FACULTEIT WETENSCHAPPEN

Asteroseismic analysis and modelling of red giant stars observed by the NASA *Kepler* space telescope

Bram BUYSSCHAERT

Promotor: Dr. E. Corsaro
KU Leuven

Promotor: Prof. Dr. J. Christensen-Dalsgaard
Aarhus Universitet

Co-promotor: Dr. P. G. Beck
SAp, IRFU/DSM/CEA Saclay

Proefschrift ingediend tot het behalen van de graad van Master of Science in de Sterrenkunde

Academiejaar 2013-2014

Acknowledgements

Many people have contributed towards this thesis throughout past year, and without them this work might have looked very differently. First of all, my promoters Enrico, professor Jørgen Christensen-Dalsgaard and Paul, who have rode along with me for one-year long journey and helped me to tackle the many difficulties along the way. Thank you for everything! For the many fruitful discussions, the many interesting science (and life) lessons, the assistance in tackling all those problems related to the asymptotic relation, and how to write a proper thesis. I have learned a tremendous amount the past year!

Pieter, thank you for solving all my *Python* related questions and to provide your repository to analyse the *fgong* files. Although I will probably never reach your level of understanding of *Python*, I have increased my scripting skills a lot thanks to you.

Victor, thank you for setting me up with GARSTEC and helping me out with general questions about stellar modelling.

Chen, thank you for helping me with all my *IDL*, ASTEC and ADIPLS questions!

Thank you professor Hans Kjeldsen and professor Torben Arentoft for converting the simulator for solar-like oscillations, so that it could make artificial data for red giants, even when this was on a very short notice.

Ditte, Vincent, Mikkel, Jens, Vichy, Rhita-Maria, Karsten, Frank, Victor and Brandon for the many astrophysical and non-astrophysical discussions during office hours and on Fridays after office hours! The Friday evenings in office 435 were very *hygge* and will not soon be forgotten.

Thanks to the International Office in Leuven and the International Center in Aarhus for helping to organise my Erasmus stay at Aarhus University, and thank you professor Jørgen Christensen-Dalsgaard and members of SAC that I was allowed to work at this institute with a very nice work-environment.

All those wonderful people I met during my Erasmus in Aarhus, thank you! Even though I was rather absent during the last few weeks, and missed some parties, you kept supporting and motivating me! Also thanks to all the Belgian people who drove hours to a far away country to see Legoland!

Ten slotte een dikke merci aan papa en Isabelle! Merci dat ik mijn dromen kon waarmaken door Sterrenkunde te studeren! Merci dat ik een ongelooflijke ervaring mocht beleven door op Erasmus te gaan naar Denemarken! Merci voor al de steun en interesse tijdens mijn studies en tijdens mijn thesis, zonder eigenlijk volledig te snappen wat ik nu al die tijd heb gedaan.

Preface

" *At first sight it would seem that the deep interior of the Sun and stars is less accessible to scientific investigation than any other region of the universe. Our telescopes may probe farther and farther into the depths of space; but how can we ever obtain certain knowledge of that what is hidden behind substantial barriers? What appliance can pierce through the outer layers of a star and test the conditions within?* "

Sir Arthur Stanley Eddington

This famous quote was presented in the opening paragraph of his book *The Internal Constitution of the Stars* (Eddington 1926). One answer to this intriguing question is by calculating theoretical models from our current understanding of physics. Such an approach always lacks comparison with observational results, since the top most layers of the star are blocking the direct view into deeper layers. However, *Asteroseismology*, the seismic analysis of oscillation modes probing the interior of stars, allows an indirect approach to characterise the conditions deep inside the star. These oscillations distort the stellar surface by producing detectable, periodic brightness variations and velocity variations.

The unprecedented photometric quality of space telescopes like CoRoT and *Kepler* lead to a revolution in asteroseismology. The NASA *Kepler* space telescope allowed for unprecedented photometric accuracy, nearly uninterrupted and very long time span observations, providing data for a vast number of stars, in various evolutionary stages. This is something difficult from ground-based observations, since the day night rhythm forces large, regular gaps in the dataset.

Red giants are large, evolved and cool stars that have ceased burning hydrogen in the core. However, not all red giants are in the same evolutionary phase and the difference lies in their core properties and internal structure. For some of them, the main energy sources are gravitational contraction and shell hydrogen burning, while others have reached the phase of stable core helium burning, surrounded by a burning hydrogen shell. Since these stars pulsate due to the near-surface convection, asteroseismology can be used to study the differences in core properties, hence characterise the evolutionary state of the red giant.

However, their oscillations have tiny amplitudes and therefore are very challenging targets for ground-based observations. Since the advent of space telescopes, photometric data of these stars, obtained with CoRoT and *Kepler* lead to major advances in our understanding of stellar physics. In the mean time, the seismic analysis of several thousand red giants revealed many details of the deep interior of those stars. Most significant is the detection of oscillations, so called *mixed modes*, that form a standing wave between the surface and the deep interior. This detection extended the sensitivity of the seismic analysis into the very deep interior of the red giant, allowing us to investigate the oscillating star as a whole.

This thesis is dedicated to the extraction of the seismic information and theoretical modelling of red giants that were observed with the NASA *Kepler* space telescope for 1152 days. A special focus is set on the extensive automated analysis of mixed modes. The results of this analysis presented in this work contribute to a improved global understanding of the seismological constraints from mixed modes.

Summary

Red giants are evolved, low-mass, cool stars that have been observed in large samples and for long time spans by *Kepler*. Since these stars oscillate due to the near-surface convection, asteroseismology can be used as a tool for studying the differences in the stars' core properties, hence characterise their evolutionary stage.

In the context of this work, a selection of red giants observed with the NASA *Kepler* space telescope was made, on which a seismic analysis is performed in order to deduce the evolutionary stage of the stars considered. The sample of stars investigated does not show effects caused by stellar rotation in the stars' oscillation spectra and provides high signal-to-noise oscillations.. Three stars are included in the sample. These are KIC 6928997, KIC 6762022 and KIC 10593078, for which *Kepler* observations with a total time span of 1152 days (Q0 - Q13), are used. An artificial star, with known stellar parameters, is also included in the sample in order to deduce all systematics in the analysis, as a hare-and-hound exercise. In order to study and analyse the seismic parameters of the red giants, a repository of *Python* packages has been built, acting as a semi-automated pipeline.

Seismic parameters, such as the frequency of maximum oscillation power ($\nu_{\max}$) and the large frequency separation ($\Delta\nu$), are computed from the power spectral density (PSD), calculated from the *Kepler* data. Significant oscillation modes are extracted from the PSD by means of a Bayesian Markov Chain Monte Carlo (MCMC) method. These oscillation modes contain dipole mixed modes, which are sensitive to the most inner parts of the star, and are used to determine its evolutionary stage. The main objective in this work is to explore the robustness of the solution for the true period spacing $\Delta\Pi_1$, which is observationally determined and deduced from detailed stellar modelling.

In a first step, $\Delta\Pi_1$ is determined from the observations according to two different methods. Values are obtained from the empirical fit to the observed period spacings ΔP and by the asymptotic relation, described by Mosser et al. (2012b). The uncertainties on both $\Delta\Pi_1$ and the coupling factor q are also computed. Therefore, gridsearches in the corresponding parameters space of the true period spacing $\Delta\Pi_1$ and the coupling factor q are performed, in order to find the best values and reproduce the mixed mode frequency pattern from the asymptotic relation. Subsequently, the most likely stellar model is computed for each red giant. From these stellar models, $\Delta\Pi_1$ is calculated using the Brunt-Väisälä frequency. Using the true period spacing, two stars in our sample and the artificial star are classified as a red giant branch (RGB) star, while it is found that KIC 6762022 is in the red clump (RC) stage.

The values deduced for $\Delta\Pi_1$ according to both the methods used in this work for analysing the observations correspond to one another within 5.4%. The values determined for $\Delta\Pi_1$ from the models and the observations agree within less than a percent. The computed values for $\Delta\Pi_1$ correspond exactly to those stated in the literature. However,

during the study it is shown that the uncertainties stated in the literature are likely to be too optimistic, being of the order of milliseconds. Therefore it is argued that a more realistic error is of the order of seconds, which has no impact at all on the clear determination of the evolutionary stage of the red giant.

The uncertainties on the coupling strength q do not allow instead to constrain the parameter. This is likely related to the lack of dipole mixed modes in the most senstivie regions, namely around the radial and quadrupole modes.

The implications of the larger uncertainties on both $\Delta\Pi_1$ and q will can only be quantified from the detailed stellar modelling of a large sample of stars, and with the inclusion of red giants showing rotational effects, since it has been shown that 80% of the observed red giants show effects of rotation.

Lastly, the inclusion of an artificial star in the analysis provided a good step forward, since it made the presence of some problems related to the current development of the simulator evident, making quantitative conclusions regarding the systematics difficult. In the near-future the description for the amplitudes and mode lifetimes will be implemented in the simulator, as well as the granulation effects will be included.

Samenvatting

Rode reuzen zijn oude, koele sterren met een lage massa. Een groot aantal van dit type sterren zijn gedurende een lange tijdsperiode geobserveerd geweest met de NASA *Kepler* ruimtetelescoop. Aangezien deze sterren trillingen vertonen, veroorzaakt door convectie zones dicht bij het steroppervlak, kan asteroseismologie gebruikt worden om verschillen in de interne eigenschappen van de rode reus te onderzoeken. Deze variaties in de kern structuur van de ster worden gegenereerd door verschillen in hun levensfase.

Enkele van deze rode reuzen, geobserveed met *Kepler*, werden gebruikt voor een seismische studie, waardoor de correcte levensfase van de ster kan bepaald worden. De selectie van sterren, die gebruikt worden in dit onderzoek, vertonen duidelijke pulsaties in hun frequentie spectrum maar geen effecten van rotatie. In totaal werden drie sterren geselecteerd, KIC 6928997, KIC 6762022 en KIC 10593078, waarvoor 1152 dagen (Q0 - Q13) van *Kepler* observaties werden gebruikt. Een extra, gesimuleerde ster, met vooraf gekende eigenschappen, werd bij de selectie toegevoegd om effecten eigen aan de analyse te kunnen bestuderen. Om de noodzakelijke seismische parameters van deze rode reuzen te bestuderen, werd een eigen pipeline geconstrueerd, bestaande uit verschillende *Python* scripts.

Seismische parameters zoals de frequency of maximum oscillation power ($\nu_{\max}$) en de large frequency separation ($\Delta\nu$) werden bepaald uit de power spectral density (PSD), berekend voor de *Kepler* observaties. Significante ster trillingen werden bepaald uit de PSD, d.m.v. Bayesiaanse Markov Chain Monte Carlo (MCMC) methodes. Eén soort van deze pulsaties zijn dipool modes, die een gemengd character hebben. Door deze specifieke eigenschappen zijn ze zeer gevoelig aan de eigenschappen en structuur van de kern en kunnen ze gebruikt worden om de levensfase van de ster bepalen. In dit werk werd hoofdzakelijk de robuustheid van de verschillende methodes om $\Delta\Pi_1$ (de true period spacing) te testen. Deze parameter werd theoretisch berekend, uit ster-evolutie modellen, en bepaald uit de gebruikte data.

Twee methodes werden gebruikt om $\Delta\Pi_1$ te bepalen uit de observaties. Eén methode maakt gebruik van een empirische fit voor de observed period spacing (ΔP), terwijl een andere de asymptotice relatie, ontwikkeld door Mosser et al. (2012b), gebruikt. De onzekerheden op de $\Delta\Pi_1$ en de coupling factor q zijn ook bestudeerd. Hiervoor werden roosters in de parameter ruimte $\Delta\Pi_1$ en q gemaakt. De mogelijke oplossingen op dit rooster werden vergeleken met de observaties om de meest waarschijnlijke beschrijving van het patroon van de dipool gemende modes te bepalen. Vervolgens werden ster-evolutie codes gebruikt om het meest waarschijnlijke ster-evolutie model voor iedere rode reus te bepalen. Voor deze modellen kon $\Delta\Pi_1$ ook bepaald worden, uit de beschrijving van de Brunt-Väisälä frequentie. M.b.v. de true period spacing kon de levensfase van de sterren in onze selectie bepaald worden. De artificiële ster, KIC 6928997 en KIC 10593078 werden geklasseerd

als red giant branch (RGB) sterren, terwijl KIC 6762022 in de red clump (RC) fase is.

De waardes berekend voor $\Delta\Pi_1$, bepaald met de veschillende methodes voor de *Kepler* observaties, verschillen minder dan 5.4% van elkaar, terwijl deze van model en volgens de MCMC methode minder dan 1% verschillen. De finale waardes zijn exact dezelfde als deze van de literatuuur maar het verschil ligt in de bepaalde foutmarges. Deze in de literatuur zijn vele malen kleiner, mogelijk te optimistisch en in de grootte orde van milliseconden. Terwijl deze bepaald in dit werk in de marge van seconden liggen en meer realistisch zijn. De bepaalde grootte orde van de onzekerheden is echter niet zo groot, dat enige misidentificatie mogelijk is tussen de verschillende levensfases.

De foutmarges bepaald voor de coupling factor q zijn echter zo groot dat deze niet exact kan bepaald worden. Dit is hoogstwaarschijnlijk te wijten aan het gebrek aan gebruike dipool modes in de meest gevoelige regio's van de PSD, namelijk rond de radiale en quadrupool modes.

De uiteindelijke effecten van deze grotere onzekerheden op zowel $\Delta\Pi_1$, als op q zullen echter pas duidelijk blijken uit gedetailleerde modellering voor een grotere selectie van rode reuzen. Deze grotere selectie dient ook sterren te bevatten die effecten vertonen van rotatie in hun frequentiespectrum, aangezien dat bijna 80% van deze steren rotatie vertonen.

Het gebruiken van artificiële data is een stap in de goede richting om effecten, eigen aan de analyse, te bestuderen. De simulatie vertoonde echter enkele problemen, die te wijten zijn aan de huidige set-up van de simulator. Daardoor is het nog niet mogelijk om quantitatieve conclusies te maken over de analyse. In de nabije toekomst zullen een andere beschrijving voor de amplitudes en mode lifetimes geïmplementeerd worden in de simulator, alsook granulatie effecten.

Vulgariserende Samenvatting

Er bestaan verschillende soorten sterren, die allemaal hun eigen kenmerken hebben. Ze kunnen variëren in massa, temperatuur, samenstelling en / of leeftijd. Eén van deze types sterren, is de rode reus. Dit is een oude, koele ster met een lage massa die niet meer de juiste eigenschappen heeft in haar kern om waterstof te verbranden (en zal één van de volgende levensfase zijn van onze eigen zon). De ster heeft echter andere energiebronnen gevonden en men kan de rode reuzen opdelen in twee types. Eén type verbrandt waterstof in een schil rond haar kern en ondergaat contractie, terwijl de andere helium verbrandt in haar kern met daar rond een schil van waterstofverbranding.

De verschillende energiebronnen zorgen voor andere kenmerken in de kern van de ster, die doorgaans niet rechtstreeks kunnen waargenomen worden. Door de trillingen aan het oppervlak van deze ster te bestuderen, gelijkaardig met de studie van aardbevingen op Aarde, kunnen we meer te weten komen over rode reuzen. Door de aard van sommige van deze trillingen, die zowel voorkomen aan het oppervlak en diep in de kern, kunnen de inwendige eigenschappen van de ster bestudeerd worden en daaruit kan het type van de rode reus worden afgeleid

Voor dit project werden drie rode reuzen gekozen: (i) die geen effecten vertonen van hun rotatie, aangezien deze de studie van de trillingen bemoeilijken; (ii) waarvoor de pulsaties aan het oppervlak duidelijk zichtbaar zijn. Deze sterren werden onafgebroken geobserveerd voor 1152 dagen met de NASA *Kepler* ruimtetelescoop. Door deze lange tijdsperiode en door de uitstekende eigenschappen van deze ruimtetelescoop, kunnen de frequenties van de oscillaties gedetailleerd bestudeerd worden. Een extra, gesimuleerde ster, met vooraf gekende eigenschappen, werd bij de selectie toegevoegd om effecten eigen aan de analyse te kunnen bestuderen.

De analyse werd als volgt uitgevoerd: eerst werden de frequenties van de trillingen in de rode reus bepaald. Daarna werden de sterren gemodelleerd m.b.v. ster-evolutie codes. Deze theoretische modellen werden ten slotte vergeleken met de observaties om het best passende model te bepalen en dus ook theoretisch het type rode reus te kenmerken.

Het was mogelijk om, gebruikmakend van de methodes om de observaties te analyseren alsook van de theoretische modellen, het type rode reus te bepalen. De waardes voor de parameter, berekend uit de stertrillingen, die het type rode reus bepaalt, lagen binnen de foutmarge van de verschillende methodes. De waardes voor deze parameter voor twee van deze sterren, die al eerder bestudeerd werden in dit opzicht, stemden overeen met die gegeven in de wetenschappelijke literatuur. Het grote verschil tussen dit werk en de literatuur zijn de gevonden foutmarges. Deze liggen tot een factor 1000 hoger t.o.v. de literatuur. In dit werk zijn ze systematisch bepaald door een rooster van mogelijke waardes te onderzoeken, terwijl deze uit de literatuur bepaald werden uit de convergentie van de oplossing, wat te optimistisch is door de verschillende lokale minima in de waarschijnlijkheid van het model.

Acronyms

ACF auto-correlation function.

ADIPLS Aarhus adiabatic oscillation package.

AIC Akaike Information Criterion.

ASTEC Aarhus STellar Evolution Code.

BIC Bayesian Information Criterion.

FOV field of view.

FWHM Full Width at Half Maximum.

***g* mode** gravity mode.

GARSTEC GARching Stellar Evolution Code.

GUI Graphical User Interface.

H-R Hertzsprung-Russell.

KASC WG8 Working Group 8.

KIC *Kepler* Input Catalog.

LS least-squares.

MCMC Markov Chain Monte Carlo.

MS main sequence.

NASA National Aeronautics and Space Administration.

***p* mode** pressure mode.

p-p chain proton-proton chain.

ppm parts per million.

PSD power spectral density.

RC red clump.

RGB red giant branch.

SNR signal-to-noise ratio.

TAMS terminal-age main sequence.

ZAMS zero age main sequence.

Contents

Chapter 1

Introduction

Oscillations seen as brightness variations at the surface of our own star, the Sun, have been studied for several centuries. The analysis of these pulsations, known as helioseismology, allows one to derive information from the different internal layers of the Sun, which are otherwise inaccessible to direct observations. A similar type of oscillations are observed in red giants, and are recently used to determine the evolutionary stage of these evolved, low-mass, cool stars.

The stellar evolution up the different phases comprising the stage of the so-called red giants are presented in Section 1.1. General theory about the stellar oscillations are presented in Section 1.2, as are the differences between pressure modes and gravity modes. The mixed character of some pulsation modes and how these can be used to determine properties of the stellar interior are discussed in Section 1.3, together with the asteroseismic scaling relations. Some information about the NASA *Kepler* space telescope is given in Section 1.4.

1.1 Introduction to red giants

A star spends most of its life burning hydrogen in its core, during a phase known as the main sequence (MS). When the central region runs out of hydrogen, the fusion reaction stops and the star is in need of a new energy source. Since the central region is not hot enough to start the fusion of helium, the only way out is gravitational contraction. The core contracts, causing the central density and the central temperature to rise. To counterbalance the increasing luminosity, the envelope of the star expands, decreasing the effective temperature $T_{\rm eff}$ of the surface, hence the star becomes a subgiant (cooling at almost constant luminosity). The red giant phase then starts when the hydrogen is ignited in a shell around the core due to the increase of the internal temperature caused by gravitational contraction. This allows the star to increase its luminosity, hence rising the red giant branch (RGB) in the Hertzsprung-Russell (H-R) diagram. During the different evolutionary phases making up the red giant stage, the outer envelope becomes convective due to the large temperature gradient, hence inducing solar-like oscillations.

Since this work concentrates on the study of red giants, a brief discussion of stellar evolution from the MS to the end of the central helium burning phase is provided. The work of Cassisi & Salaris (2013) is closely followed, since it supplies a detailed discussion about stellar evolution and its implications. The focus remains on low-mass stars with a mass between 1 $M_{\odot}$ and 2 $M_{\odot}$, because the stars analysed in this work fall in this mass range.

A star leaves the pre-MS stage when it reaches central temperatures adequate for hydrogen burning. The point in the H-R diagram where the star reaches the MS is called the zero age main sequence (ZAMS) and it is indicated in Figure 1.3. These hydrogen burning processes have a different temperature dependence, therefore distinct mechanisms are happening in stars with diverse birth mass. For stars with masses lower than $\sim 1.3\ M_{\odot}$, hydrogen is mainly burned by the proton-proton chain (p-p chain), while the dominant process in more massive stars is the CNO cycle. The star regulates the thermonuclear burning processes in order to maintain its hydrostatic equilibrium. The stars swells when the energy supplied is more than that needed, decreasing the temperature and density in the burning regions, hence reducing the efficiency of the burning process and restoring the equilibrium.

The thermonuclear hydrogen burning process through the p-p chain has different pathways but all start with the fusion of two hydrogen atoms into deuterium, which is the slowest step in the process. This deuterium atom is subsequently converted to helium-3, after which different pathways convert it into stable helium and liberate energy. The p-p chain mechanism has only a weak temperature dependence, therefore a large part of the core participates in the energy production, keeping the core radiative. The CNO mechanism is a catalytic cycle that converts four hydrogen atoms into helium using a carbon-12 atom as catalyst. Different isotopes of carbon, nitrogen and oxygen are produced by adding the protons piecewise and positron emission. In the final step the initial carbon-12 atom is retrieved and a stable helium atom is produced. The CNO cycle is much more temperature dependent and happens in the convective core of the star.

Once all the hydrogen in the core is converted into helium, the star has reached the terminal-age main sequence (TAMS) and thermonuclear burning of hydrogen can no longer withstand gravitation. For low mass stars, the hydrogen burning is smoothly shifted from the core to a shell around the helium core, while it is completely halted for more massive stars and only re-ignites after the overall contraction phase. The temperature and density of the central region are not yet sufficiently high to initiate helium fusion. Contraction of the helium core stars when the Shönberg-Chandrasekhar limit has been reached. This gives an upper limit for the mass of the isothermal helium core, approximated as an ideal gas, to remain in hydrostatic equilibrium, and it is expressed by a ratio of the mean molecular weight in the envelope and the core. When the core gets too massive, the core contracts and gravitational energy is released, heating up the core, and the Shönberg-Chandrasekhar limit no longer applies. The core contraction in the subgiant phase is accompanied by an expanding radius of the star, decreasing the temperature at almost constant luminosity (Figure 1.3). A large convective envelope appears during the subgiant phase, irrespective of any pre-existing outer convective regions during the MS phase. This convective envelope occurs as a reaction on the contraction of the core. Due to the expansion, the outer regions are now cooler and the opacity has increased, making radiative energy transport less efficient. This convective envelope steadily increases during the subgiant phase and the subsequent red giant branch (RGB) phase.

During the RGB phase (Figure 1.3) the convective envelope penetrates to a maximum depth, an event known as the first dredge up. Since elements of lower regions, where thermonuclear burning has taken place, are mixed with the envelope, changes are made in the surface composition of the star. These changes are most notable for elements

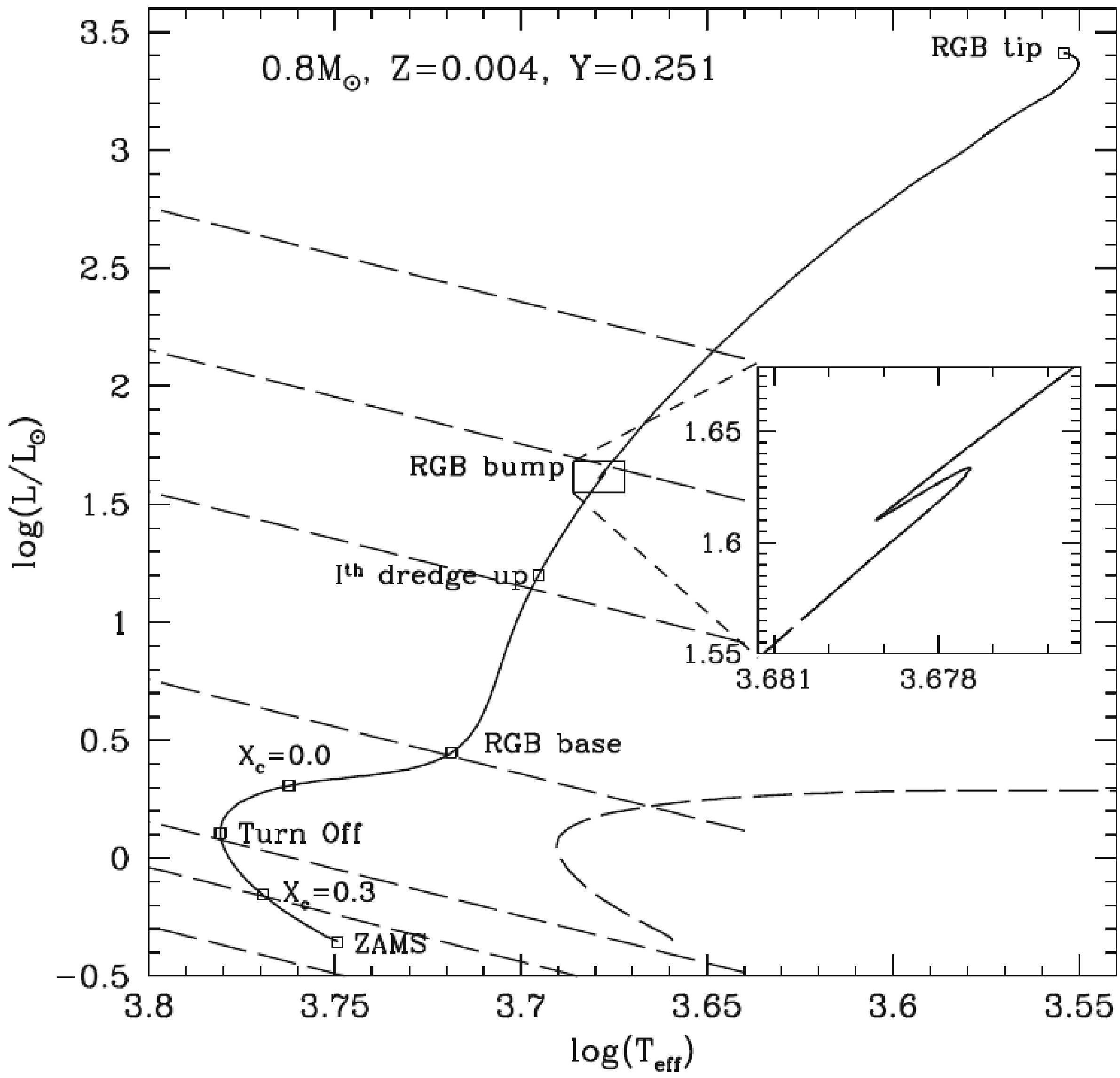

Figure 1.1: H-R diagram evolution of a low-mass star. The evolution is from the ZAMS to the RGB tip. The labels mark selected evolutionary stages. The thin-dashed lines represent the loci of constant radius for respectively $R/R_\odot = 0.6, 0.8, 1.0, 2.0, 5.0, 10$ and 20 from bottom to top. Figure 3.11 from Cassisi & Salaris (2013).

produced during the burning phases, e.g. the different helium isotopes and the CNO elements. A chemical discontinuity is left for certain radial layers, as the convective envelope starts to penetrate less deeply. When the hydrogen shell burning reaches these chemical discontinuous layers, it goes through a remarkable evolution in the H-R diagram, crossing the same luminosity in the H-R diagram three times in what is called the RGB bump.

The evolution along the RGB ends at the tip of the RGB, which is marked as the maximum luminosity that a hydrogen shell burning star can reach, corresponding to $L_{\rm tip} = 103.4\ L_\odot$. This limit is reached when sufficient conditions allow to ignite helium in the core. The ignition happens a little off center, since the internal temperature profile reaches a maximum at a shell of $M_r = 0.2\ M_\odot$ (Figure 1.3). The ignition also happens under degenerate conditions for stars with a mass below $\sim 2.3\ M_\odot$ (low-mass stars). The burning is ignited in a degenerate layer and no moderation on the burning rate happens. The burning rate increases with the increasing temperature and a thermal runaway occurs, known as the helium-flash. A tremendous amount of energy is released for a few seconds in the core, before moderation happens because of two factors. First, the increase in temperature decreases the level of electron degeneracy in the core. Second, because of the increase in energy convention sets in the core, transporting the energy outwards to other inner layers.

After the helium-flash, the star tries to re-ignite the central helium burning. This happens during several thermal pulses (Figure 1.3), until stable helium burning is obtained in the core and the star is said to have reached the horizontal branch. The metal rich, population I stars, settle on a substructure of the horizontal branch, called the red clump (RC). More massive stars ($M > 2.3\ M_\odot$), which underwent a smoother transition from hydrogen shell burning to central helium burning, settle in a different substructure of the horizontal branch, namely the secondary RC. After a quiescent central helium burning phase, the star moves on to the asymptotic giant branch when the central helium is depleted.

1.2 General Introduction to Asteroseismology

One can wonder "*Why do stars pulsate in the first place and are oscillations expected for all stars?*". Pulsations are seen in a large variety of stars, throughout many evolutionary stages. However, oscillations are not observed in all stars. Whether this is due to the detection limits of present-day instruments or whether these stars intrinsically do not pulsate, is still an unresolved question, which only will be answered by using even more sensitive instrumentation (Chaplin et al. 2011a). For the stars that do pulsate, different driving mechanisms have been identified and different classes of oscillations have been observed. These stars' oscillations are seen as harmonics of their natural oscillations modes, according to specific 3D configurations.

The pulsations are seen as a relatively stable phenomenon in light curves or radial-velocity time series, spanning over many years. During one pulsation cycle, energy is lost because the volume of the star damps the oscillation. Therefore, a driving mechanism is necessary to supply energy for the oscillations. Two main different driving mechanisms have been identified so far, briefly discussed below. An extensive review is given by Aerts et al. (2010, and references therein).

- Regions in the star that gain heat during the compression phase of the pulsation cycle drive the oscillation, while those that lose heat during compression damp the oscillation. This is called the heat-engine mechanism. When the heated region, usually a radial layer, obtains enough energy to drive the pulsation, it acts as a heat engine. It converts thermal energy in mechanical energy. This driving mechanism is often connected to properties of the opacity, hence the name κ mechanism (Dziembowski & Pamiatnykh 1993; Gautschy & Saio 1993; Charpinet et al. 1997). In certain ionisation layers, these could either be hydrogen and helium ionisation region or those for iron, an increase in the opacity blocks the radiation, heating up the gas, hence the pressure increases in this layer and the star swells. The opacity

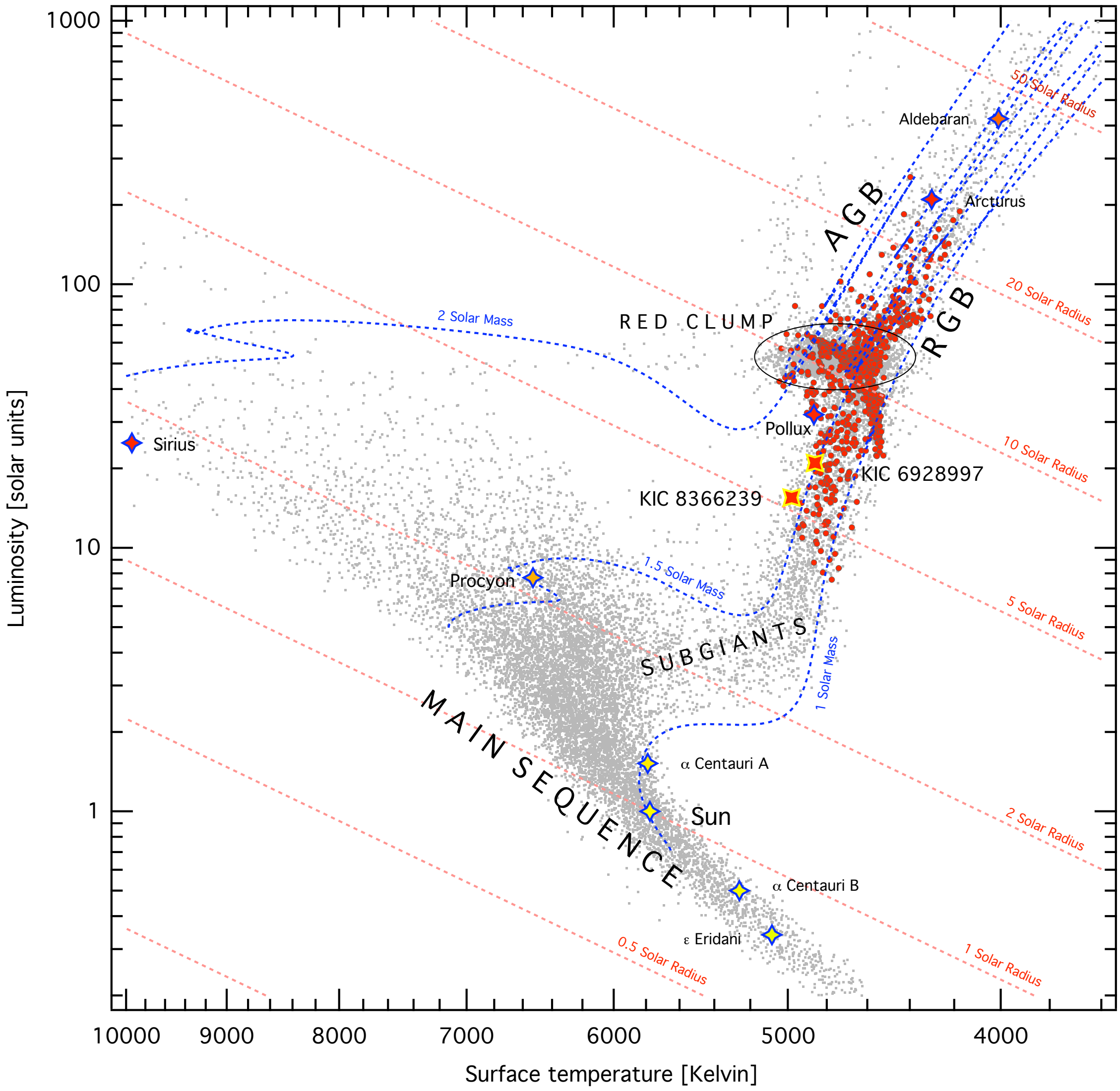

Figure 1.2: H-R diagram showing the temperature and luminosity of 1400 *Kepler* red giants, and the stars in the HIPPARCOS catalogue. Three evolutionary tracks for stars with a different birth-mass, 1, 1.5 and 2 $M_\odot$, are indicated. These evolve from the MS up to asymptotic red giant branch. Figure taken from Beck & Kallinger (2013).

drops as the gas becomes ionised, less radiation is absorbed and the gas cools down. It can no longer support the weight of the above layers, making the star contract. The gas recombines during the contraction phase. The recombination increases the opacity again, therefore more radiation is again absorbed, heating up the layers and the cycle is then repeated.

- Another driving mechanism is related to the stochastic behaviour of the near-surface convective layers. This mechanism accounts for the oscillations seen in the Sun (Goldreich & Keeley 1977; Elsworth et al. 1995; Christensen-Dalsgaard 2002), in MS stars with masses lower than 1.6 $M_\odot$ (Christensen-Dalsgaard 1982; Christensen-Dalsgaard & Frandsen 1983; Houdek et al. 1999) and in red giants (Frandsen et al.

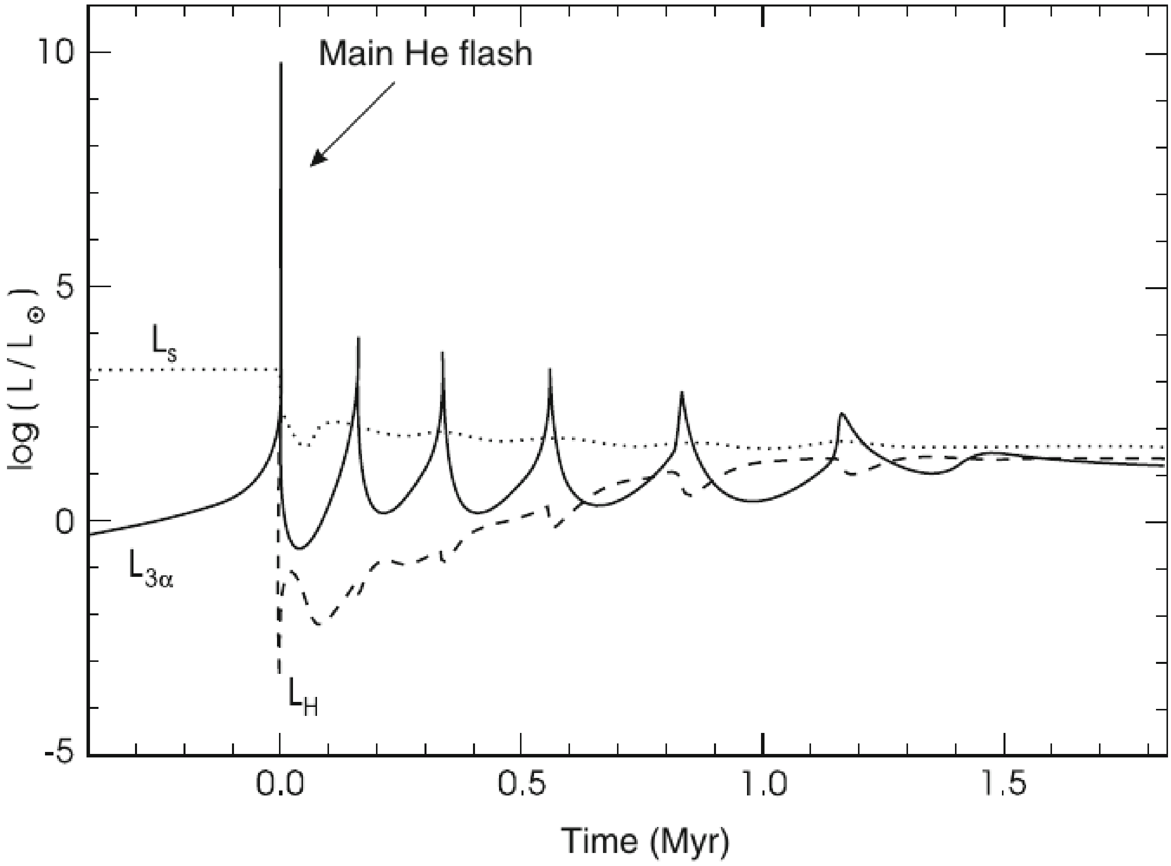

Figure 1.3: Time evolution of the surface luminosity L_s, the luminosity produced by the helium fusion $L_{3\alpha}$ and the hydrogen shell burning L_H. The start of the helium-flash, marking the end of the RGB, is indicated at time zero. Figure 3.30 from Cassisi & Salaris (2013).

2002; De Ridder et al. 2006b; Hekker et al. 2006). The stochastic and turbulent convection in these outer layers provides enough energy, which acts as engine to drive the global oscillations. These pulsations are also intrinsically damped by the same convective region that energises them.

The geometrical description of the oscillations, using spherical harmonics, is presented in Section 1.2.1. Two types of stellar oscillations are seen, namely the gravity modes (g modes) and pressure modes (p modes). These are discussed in Section 1.2.2 together with a presentation of the asteroseismic parameters and the important techniques adopted for the study of these pulsations.

1.2.1 Describing the Pulsations

For a spherical symmetric star, the displacements caused by the pulsation mode are described by spherical harmonics (Aerts et al. 2010). These displacements are in the three orthogonal directions, namely r the distance to the center, θ the co-latitude, measured from the pulsation pole, the axis of symmetry, and lastly the longitude ϕ. The pulsation symmetry axis coincides with the rotation axis for most stars. The nodes of pulsations are concentric shells in r, cones of constant θ and planes of constant ϕ. The equations of motions are solved with the displacements described as

$$\xi_r(r,\theta,\phi;t) = a(r)Y_\ell^m(\theta,\phi)\exp(-i2\pi\nu t)\ , \tag{1.1}$$

$$\xi_\theta(r,\theta,\phi;t) = b(r)\frac{\partial Y_\ell^m(\theta,\phi)}{\partial\theta}\exp(-i2\pi\nu t)\ , \tag{1.2}$$

$$\xi_\phi(r,\theta,\phi;t) = \frac{b(r)}{\sin(\theta)}\frac{\partial Y_\ell^m(\theta,\phi)}{\partial\phi}\exp(-i2\pi\nu t)\ , \tag{1.3}$$

where ξ_r, ξ_θ and ξ_ϕ are the displacements along the r, θ and ϕ direction. $a(r)$ and $b(r)$ are amplitudes, ν is the oscillation frequency and $Y_\ell^m(\theta,\phi)$ are spherical harmonics. These spherical harmonics are given by

$$Y_\ell^m(\theta,\phi) = (-1)^m\sqrt{\frac{2\ell+1}{4\pi}\frac{(\ell-m)!}{(\ell+m)!}}P_\ell^m(\cos(\theta))\exp(im\phi)\ , \tag{1.4}$$

where $P_\ell^m(\cos(\theta))$ are the Legendre polynomials.

The pulsation modes in a star are described by three quantum numbers. The first quantum number specifies the number of nodes along the radial direction and is called the *overtone of the mode* or *radial order*, indicated by n. The *spherical degree* of the mode ℓ instead describes the number of surface nodes, while the *azimuthal order* m describes the number of surface nodal lines crossing the pulsation symmetry axis. The total number of surface nodes that are lines of longitude can never be larger than $2\ell+1$, indicating the relation $|m| < \ell$. Modes with positive m are prograde modes, i.e. travelling in the direction of rotation, and those with negative sign are retrograde modes.

The simplest modes are radial modes, for which $\ell = 0$. The star swells and contracts spherically symmetric with the stellar surface as an anti-node and the core as a node. The simplest non-radial mode is the dipole mode, which has $\ell = 1, m = 0$. The equator acts as a nodal line. When the northern hemisphere swells up, the southern hemisphere contracts, and vice versa. Modes with a spherical degree $\ell = 2$ are called quadrupole modes and those with $\ell = 3$ octupole. The spherical harmonics for modes ranging from $\ell = 0, |m| = 0$ to $\ell = 4, |m| = 4$ are given in Figure 1.4.

1.2.2 Pressure and Gravity Modes

The oscillations observed in the context of asteroseismology can be split in two major classes (Aerts et al. 2010). The differences between the two types arise from a different restoring force. They come from different sets of solutions for the equations of motions. The first set of solutions has pressure as restoring force for the oscillations, hence the modes are called pressure modes (p modes). They are acoustic waves[1] and their dynamics are described by the local sound speed c. The second corresponds to gravity modes (g modes) for which buoyancy is the restoring force for the modes. Besides the differences in restoring forces, other differences arise between both types of oscillations.

[1]The stellar pulsations present in stars are standing waves when $m = 0$, since $\exp(im\phi)$ becomes unity in Equation 1.4, otherwise it is a travelling wave.

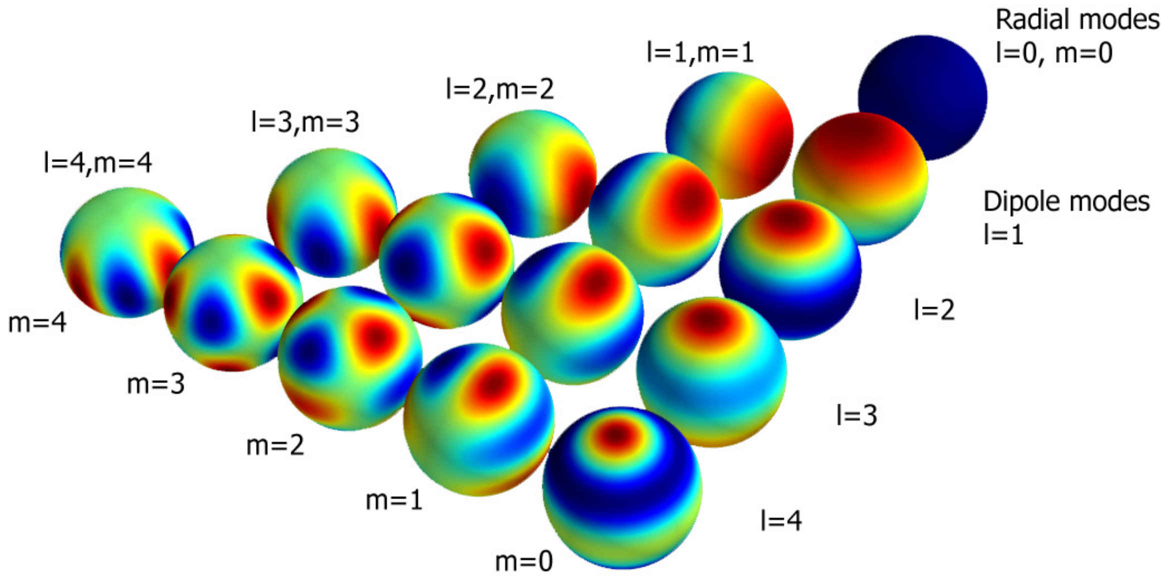

Figure 1.4: The spherical harmonics describe the displacement on the stellar surface. The spherical degree ℓ describes the total number of nodal lines on the stellar surface, while the azimuthal order m defines the number of nodal lines crossing the symmetry axis of the pulsations. Non-radial oscillations modes have a spherical degree $\ell \neq 0$, while radial modes have $\ell = 0$. Figure taken from Beck & Kallinger (2013).

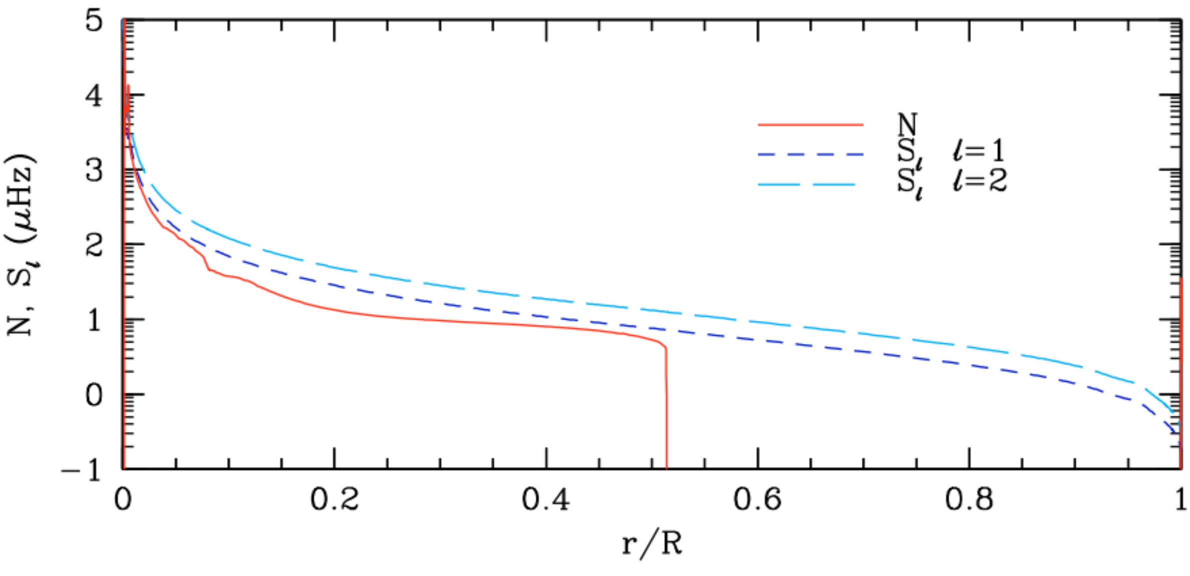

Figure 1.5: The characteristic frequencies of a 3 $M_\odot$ star in the helium burning phase. N is the Brunt-Väisälä frequency and S_ℓ is the Lamb frequency. The frequencies are expressed in logarithmic scale. Figure taken from Eggenberger et al. (2010).

The frequencies of the oscillation modes change differently as the total number of radial nodes increases. The frequency of the p modes increases with increasing n, while that of the g modes decreases. The different classes of modes also probe different parts of the stellar interior. The p modes are more sensitive to conditions in the outer regions of the star, while the g modes are more responsive to the properties of the core. This is obtained from the stability analysis for the characteristic frequencies, given graphically in Figure 1.5. When the angular frequency ω of a mode corresponds to

$$|\omega| > N \quad \text{and} \quad |\omega| > S_\ell \ , \tag{1.5}$$

the oscillation is stable and behaves as a p mode, while a g mode is stable under the condition

$$|\omega| < N \quad \text{and} \quad |\omega| < S_\ell \ . \tag{1.6}$$

When ω does not correspond to either one of these conditions, the mode is exponentially damped. Here N is the Brunt-Väisälä frequency, or buoyancy frequency, and S_ℓ the Lamb frequency. Both are defined as

$$N^2 = g\left(\frac{1}{\Gamma_1}\frac{\mathrm{d}\ \ln(p)}{\mathrm{d}r} - \frac{\mathrm{d}\ \ln(\rho)}{\mathrm{d}r}\right) \ , \tag{1.7}$$

$$S_\ell = \frac{\ell(\ell+1)c^2}{r^2} \ , \tag{1.8}$$

where

$$c^2 = \frac{\Gamma_1 p}{\rho}$$

and Γ_1 is defined as

$$\Gamma_1 = \left(\frac{\partial \ln(p)}{\partial \ln(\rho)}\right)_{ad} \ ,$$

with p the pressure, ρ the density, g the gravity, r the radial distance from the core of the star and c is the sound speed.

The asymptotic description for p modes, which is valid for $n \gg \ell$, state that modes are approximately equally spaced in frequency (Tassoul 1980, 1990). A similar asymptotic description for the g modes states that they are approximately equally spaced in period. The frequencies for p modes are approximately given by

$$\nu_{n\ell} = \Delta\nu\left(n + \frac{\ell}{2} + \epsilon\right) + \delta\nu_{0\ell} \ , \tag{1.9}$$

where n and ℓ are the radial order and spherical degree of the mode, ϵ is a constant of the order of unity and $\delta\nu_{0\ell}$ is the small frequency separation of non-radial modes to the radial mode of consecutive spherical degree. $\Delta\nu$ is known as the *large frequency separation* and denotes the main characteristic frequency separation between modes having the same spherical degree and consecutive radial order. It is related to the sound travel time across the stellar diameter and is given by

$$\Delta\nu = \left(2\int_0^R \frac{\mathrm{d}r}{c(r)}\right)^{-1} \ . \tag{1.10}$$

These frequency separations are indicated in Figure 1.6 for the red giant KIC 6928997. The large frequency separation is used to collapse the observed frequencies of the oscillation modes to a frequency échelle diagram (Grec et al. 1983). Here the frequencies are expressed in modulo $\Delta\nu$ as

$$\nu_{n\ell} = k\Delta\nu + \widetilde{\nu_{n\ell}} \ , \tag{1.11}$$

where k is an integer such that $\widetilde{\nu_{n\ell}}$ is between 0 and $\Delta\nu$. The diagram is produced by plotting $\widetilde{\nu_{n\ell}}$ on the x-axis and $\nu_{n\ell}$ on the y-axis. This p modes with the same spherical degree ℓ show up as strong vertical ridges in these diagrams.

The periods of the g modes can be described to first order as (Unno et al. 1989)

$$P_{n\ell} = (|n| + \alpha)\,\Delta\Pi_\ell \ , \tag{1.12}$$

where

$$\Delta\Pi_\ell = \frac{2\pi^2}{\sqrt{\ell(\ell+1)}} \left(\int \frac{N}{r} \mathrm{d}r \right)^{-1} \ , \tag{1.13}$$

where N is the Brunt-Väisälä frequency and α is a small constant. The integral is over the cavity in which the g modes pulsate.

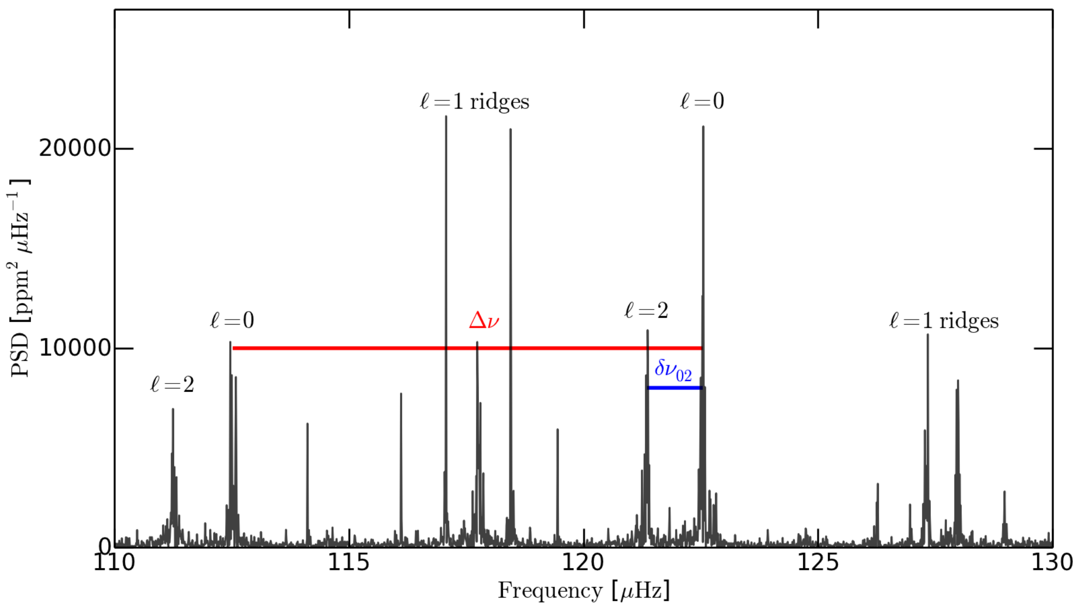

Figure 1.6: The power spectral density (PSD) of the *Kepler* red giant KIC 6928997. The radial $\ell = 0$ and quadrupole $\ell = 2$ pressure modes show a very regular pattern, while the dipole modes $\ell = 1$ show a mixed behaviour. The large frequency separation $\Delta\nu$ and the small frequency separation $\delta\nu_{02}$ are indicated.

1.3 Red Giant Asteroseismology

From helioseismology, it became clear that stars that have a convective envelope, could show solar-like oscillations, irrespective of the evolutionary stage. These pulsations were detected in some red giants from ground based observations (Frandsen et al. 2002; De Ridder et al. 2006b; Hekker et al. 2006; Aerts et al. 2010), but only a handful were known. Interesting properties, such as non-radial mixed modes, were predicted (Christensen-Dalsgaard 2004; Dupret et al. 2009), however firm detections were only possible with the use of space photometry. Using the CoRoT space telescope (2007 - 2012) and later the NASA *Kepler* space telescope (2009 - 2013), solar-like oscillations were detected in about $15,000$ red giants (De Ridder et al. 2009; Hekker et al. 2009; Bedding et al. 2010; Huber et al. 2010; Kallinger et al. 2010a; Stello et al. 2013) and the predicted non-radial mixed modes were soon detected (Beck et al. 2012; Bedding et al. 2011; Mosser et al. 2011). The unprecedented quality of the data collected by these space photometry missions allowed to rapidly set the asteroseismology of red giants as one of the most important disciplines for our understanding of stellar structure and evolution.

Some interesting properties exist for stars with solar-like oscillations. One of these are the asteroseismic scaling relations, which relate stellar fundamental properties such as the photospheric radius and mass to asteroseismic quantities. These relations are presented in the subsequent sections. The properties of the mixed modes are explained in Section 1.3.2 and how these are used to differentiate between red giants in the RGB and RC phase.

1.3.1 Asteroseismic Scaling Relations for $\nu_{\rm max}$ and $\Delta\nu$

The PSD of a time series of the brightness variations measured for a star, shows how the variance of the data is distributed over the frequency components. The units for the PSD are the square of the units of the brightness variations per unit of frequency. Asteroseismic parameters, e.g. the different frequency separations, are deduced from the PSD. An example of such a PSD is given in Figure 1.6. A detailed introduction to the seismology of red giants and the peak-bagging analysis is given in Chapter 3.

Global features can be recognised in the PSD of stars having solar-like oscillations. One of these is the frequency of maximum oscillation power $\nu_{\rm max}$, which is the central frequency of the envelope modulating the power of the oscillations. Brown et al. (1991) argued that this frequency is related to the acoustic cut-off frequency ν_c. Belkacem et al. (2011) tried to prove the underlying physics that relates $\nu_{\rm max}$ to ν_c, although the exact theoretical evidence is still under debate. Nevertheless, the developed asteroseismic scaling relation for $\nu_{\rm max}$, using the proportionality with ν_c, prove to work reasonably well for many solar-like pulsators (Bedding & Kjeldsen 2003; Chaplin et al. 2011b; Huber et al. 2011). Kjeldsen & Bedding (1995) stated the asteroseismic scaling relation for $\nu_{\rm max}$ as

$$\nu_{\rm max} = \left(\frac{M}{M_\odot}\right)\left(\frac{R}{R_\odot}\right)^{-2}\left(\frac{T_{\rm eff}}{T_{\rm eff,\odot}}\right)^{-0.5}\nu_{\rm max,\odot} \;, \tag{1.14}$$

where M and R are the photospheric mass and radius of the star and $T_{\rm eff}$ its effective temperature, and $M_\odot$, $R_\odot$, $T_{\rm eff,\odot}$ and $\nu_{\rm max,\odot}$ are the solar values.

The large frequency separation (Equation 1.10) is related to the mean stellar density (Ulrich 1986). Therefore it is also possible to obtain an asteroseismic scaling relation for

$\Delta\nu$ as

$$\Delta\nu = \left(\frac{M}{M_\odot}\right)^{0.5}\left(\frac{R}{R_\odot}\right)^{-1.5}\Delta\nu_\odot\ , \tag{1.15}$$

where $\Delta\nu_\odot$ depicts the solar value. The solar values $\nu_{\mathrm{max},\odot} = 3150\ \mu$Hz and $\Delta\nu_\odot = 134.9\ \mu$Hz are adopted in this work (Huber et al. 2011). The scaling relations can be inverted in order to obtain the photospheric radius and mass as a function of the asteroseismic parameters, giving

$$R = \left(\frac{\nu_{\mathrm{max}}}{\nu_{\mathrm{max},\odot}}\right)\left(\frac{\Delta\nu}{\Delta\nu_\odot}\right)^{-2}\left(\frac{T_{\mathrm{eff}}}{T_{\mathrm{eff},\odot}}\right)^{-0.5} R_\odot\ , \tag{1.16}$$

and

$$M = \left(\frac{\nu_{\mathrm{max}}}{\nu_{\mathrm{max},\odot}}\right)^{3}\left(\frac{\Delta\nu}{\Delta\nu_\odot}\right)^{-4}\left(\frac{T_{\mathrm{eff}}}{T_{\mathrm{eff},\odot}}\right)^{1.5} M_\odot\ . \tag{1.17}$$

1.3.2 Probing the Core

The solar-like oscillation presented above consist of p modes. For the case of red giant stars however, also g modes are present in the spectrum through their coupling to the p modes, as explained as follows. Pressure and gravity modes are propagating in different regions of the star, and are well separated by the evanescent zone, therefore no brightness variations are caused by the pure g modes. In this zone, the conditions given by Equations 1.5 and 1.6 are not fulfilled and the modes are exponentially damped. This evanescent zone becomes smaller for evolved stars, such as red giants, and coupling is possible between the g modes and p modes. These coupled modes are known as non-radial mixed modes and show a g mode behaviour in the outer regions of the star and a p mode behaviour in the internal regions.

The principle of avoided crossings (Aizenman et al. 1977; Deheuvels & Michel 2010) states that the frequencies of a g mode cannot be the same to that of a p mode of the same spherical degree ℓ. When the frequencies approach each other, they undergo an avoided crossing, as indicated in Figure 1.7. The frequencies of the p modes decrease with the age of the star, while those of the g modes increase. At the avoided crossing, also known as mode bumping, the modes have a mixed character, neither behaving as a pure p mode nor as pure g mode, hence are called mixed modes. The frequencies of these mixed modes are extremely sensitive to the evolutionary state and are therefore very interesting.

Since the dipole p modes penetrate deeper layers of the star (see Figure 1.5), the coupling with the g modes will be the strongest, therefore dipole mixed modes are expected to be the most pronounced mixed modes (Christensen-Dalsgaard 2004; Dupret et al. 2009; Montalbán et al. 2010). These were recently detected in red giants with data from the NASA *Kepler* space telescope (Bedding et al. 2011; Beck et al. 2012; Mosser et al. 2011).

It has been proven observationally that these dipole mixed modes can be used to deduce the evolutionary phase of the red giants (Beck et al. 2012; Mosser et al. 2011). The g mode character of the mixed modes is reflected in the existence of a true period spacing $\Delta\Pi_1$, which depends on the properties of the core, and differs substantially between stars along the RGB and in the RC phase. RGB stars have a $\Delta\Pi_1$ in the range of 70 - 100 s, while it varies for stars in the RC phase in the range 200 - 400 s. Using both $\Delta\Pi_1$ and

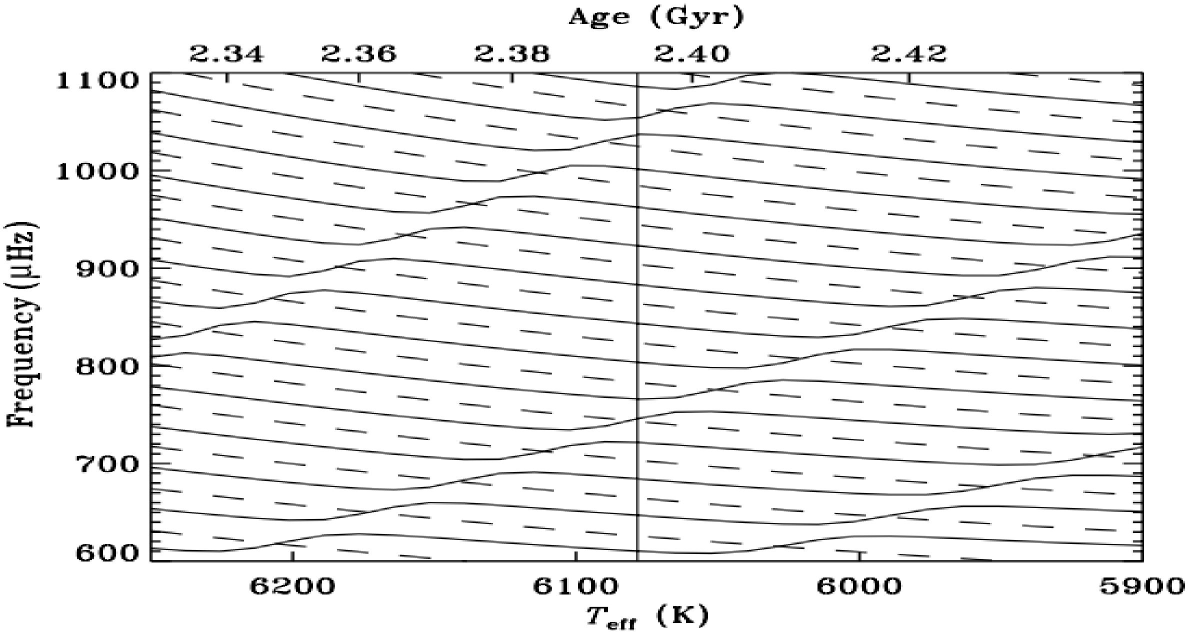

Figure 1.7: The evolution of the adiabatic frequencies with age for a model with mass 1.6 $M_\odot$, where age is measured by the effective temperature. The dashed lines correspond to radial modes ($\ell = 0$), while the solid lines are for dipole modes ($\ell = 1$). Figure taken from Christensen-Dalsgaard et al. (1995); Bedding & Kjeldsen (2003).

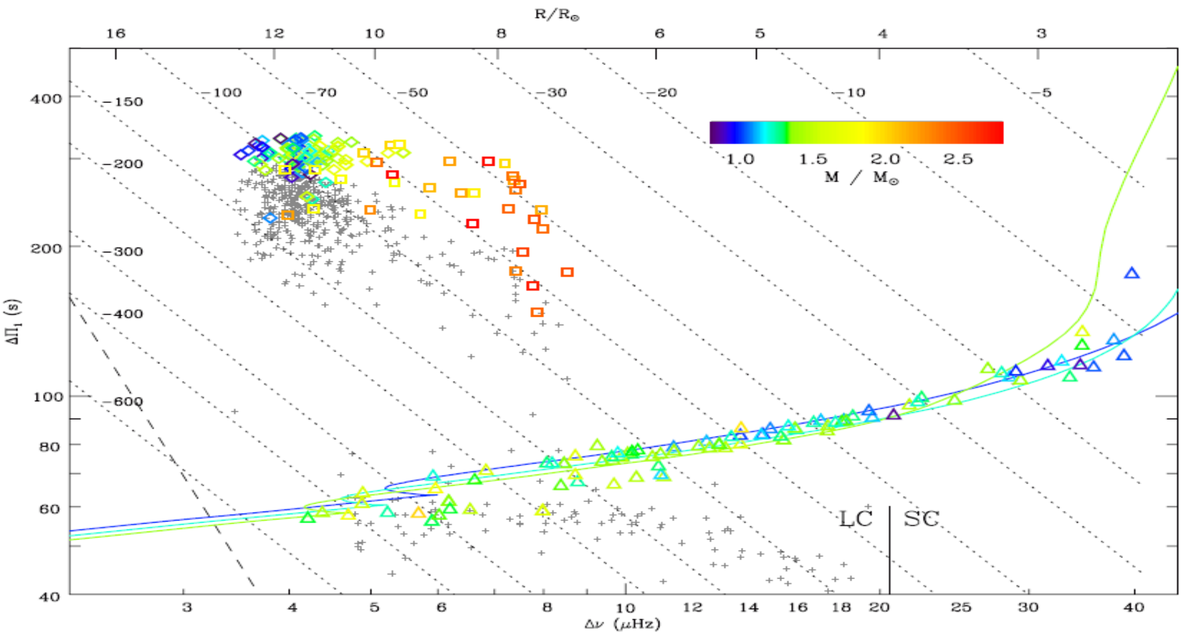

Figure 1.8: The g mode period spacing $\Delta\Pi_1$ as a function of the p mode large frequency separation $\Delta\nu$. RGB stars are indicated by triangles, clump stars by diamonds and secondary clump stars by squares. The derived mass and radius for the stars, using the asteroseismic scaling relations, are indicated by the colour scale and top y-axis, respectively. The solid colored lines correspond to a grid of stellar models with masses of 1, 1.2 and 1.4 $M_\odot$, from the ZAMS to the tip of the RGB. Figure taken from Mosser et al. (2012b).

$\Delta\nu$, it is possible to construct an asteroseismic H-R diagram (Figure 1.8), discriminating between the two types of red giants.

1.4 Kepler Space Telescope

The NASA *Kepler* space telescope was launched in March 2009 and has been operational from the 12th of May, 2009 until the 11th of May 2013. The main mission ended when the second of the four reaction wheel broke down, making accurate pointing to the field of view (FOV) no longer possible. The space telescope observed the same patch on the sky for over 1450 days.

The space telescope has a primary mirror of 1.4 m in diameter, feeding an aperture of 0.95 m. The telescope is in a Schmidt camera configuration and has a FOV extending 115 deg^2 pointing towards the northern constellations of Cygnus, Lyra and Draco. The camera consists of 42 CCD's, having 2200x1024 pixels each, giving it a total of 95 megapixels. Characteristics about the data obtained with the *Kepler* space telescope are presented in Chapter 2.

The satellite orbits around the Sun, avoiding influences by Earth occultations, stray light and any influences by the gravitational field of Earth and its orbit. The orbit is characterised as *Earth-trailing* and has an orbital period of 372.5 days, making it slowly fall further behind Earth.

Since early 2014, the *Kepler* satellite is observing again in the *K2 mission*, with a revised observing strategy in the ecliptical plain. It was shown from simulations that also in this mode *Kepler* is capable of obtaining good photometric data of red giant stars (Chaplin et al. 2013). The first 10 days of the engineering observing run is currently analysed and tested.

Chapter 2

Characteristics of Data collected by the NASA *Kepler* Space Telescope

The datasets acquired by the NASA *Kepler* space telescope are used for the analysis of the dipole mixed modes observed in red giants. More than $15,000$ red giants are observed in the *Kepler* FOV, which contains $\sim 150,000$ stars.

The characteristics of the data retrieved from this NASA space telescope are presented in Section 2.1. Since *Kepler* measured brightness variations for a vast sample of stars, a sub-sample that meets particular criteria is selected for the purpose of this work. The different criteria to choose the final set of stars and the general properties of each selected star are discussed in Section 2.2.

In order to test the characteristics of the data analysis, a blind exercise has been set up with artificial data. Section 2.3 presents information about the simulator used for generating a synthetic PSD of solar-like oscillations from a list of input frequencies with their corresponding mode inertia.

2.1 Observations

The NASA *Kepler* mission was originally designed as a planet-hunting mission (Borucki et al. 2010), where planet-candidates are seen as transit events in the continuous photometric observations. Due to its unprecedented photometric accuracy, long timespan and high duty-cycle *Kepler*, also became one of the leading instruments for the study of solar-like oscillations (Hekker et al. 2011a,b; Huber et al. 2011; Bedding et al. 2011; Chaplin et al. 2011b).

Kepler measured the brightness variations for all the $\sim 150,000$ stars in its FOV with two different sampling rates, either in short cadence, with an observation every 58.848 s corresponding to a Nyquist frequency of $\nu_{\mathrm{nyq}} \sim 8.5$ mHz, or long cadence, having a sampling rate of 29.4244 min ($\nu_{\mathrm{Nyq}} \approx 283.45$ μHz). The majority of the stars were observed in long cadence mode, while only a small sample in short cadence. Due to the operation of the satellite, the observations were regularly interrupted. One of these operations was the 90° roll around its axis to keep the solar panels illuminated, happening every 93 days. This roll also moves the CCD frame, making a star illuminate different parts of the CCD frame after each roll, hence resulting in observations subdivided into quarters (Q). The transmission of the data of the space telescope to the ground happened every 30.12 days, interrupting the observations for 0.9 days.

The different quarters are patched together and the different missing data points due to the satellite operation are taken into account according to the approach of García et al. (2011) for red giants, which has been done within the *Kepler* Asteroseismic Science Consortium Working Group 8 (KASC WG8). The light curves for almost all red giants, where solar-like oscillations have been detected, have been processed and made available for the general astrophysics community. However, this is only up to the data release of Q13, and a general release for the complete timespan Q0 - Q17 will follow in the near future.

The data used in this work span from Q0 to Q13 and account for 1152 days of observations. Starting from the light curves, the KASC WG8 members generated PSDs for every star. In particular, the PSDs were derived by calculating a Lomb-Scargle periodogram of the light curve (Aerts et al. 2010), thus representing the basic datasets adopted in this work.

2.2 Selection of the Stars

There are over 15,000 red giants monitored in the *Kepler* FOV that show solar-like oscillations, see e.g. Stello et al. (2013) . Since the entire sample of red giants is too large to be completely studied in this work, a selection has to be made. The selection criteria to find a best sub-sample of red giants to study the dipole mixed modes are given as follows:

1. The star should be known to have solar-like oscillations and to be a red giant, allowing the detection of the dipole mixed modes in the oscillation diagram.

2. Rotation complicates the PSD of the mixed modes through the presence of rotational splitting. Non-radial modes (in particular the dipole modes) are split into multiplets. The structure of the multiplets does not only depend on the rotation velocity of the star, but also on the inclination at which the star is observed (Gizon & Solanki 2003). Previous attempts to observe the (differential) rotation in red giants have proven successful (Beck et al. 2012). However the effect of rotation on the character of the mixed modes is still not fully understood. To exclude any of these effects, only red giants that do not show any evidence of rotation in their PSD are accepted, making this the strongest criterion in our selection.

3. Stars with a prominent power excess are chosen, as the mode extraction and identification will be easier. The sample of stars should also contain stars with a different $\Delta\nu$, as the evolutionary state along the RGB is also related to this parameter. The dependence on large frequency separation for the RGB stars is indicated in Figure 1.8.

During a visual analysis performed on over 1,000 PSDs, the rotational effects of the star were searched. From this inspection, only 25 red giants remained and a final selection was based on both $\Delta\nu$ and the power of the peaks in the oscillation diagram. This lead to a sample of three red giants, KIC 6928997, KIC 10593078 and KIC 6762022.

All three of them served as benchmark stars, on which comparisons between different data reduction pipelines for solar-like oscillations have been tested (Hekker et al. 2011b).

This test provides literature values for $\Delta\nu$ and $\nu_{\max}$ for all three stars. Literature values, derived according to the *CAN* method (Gruberbauer et al. 2009; Kallinger et al. 2010b), are given in Table 2.1. Effective temperatures and estimates for the surface gravity and metallicity are retrieved from the revised *Kepler* Input Catalog (KIC) (Pinsonneault et al. 2012).

The light curves of the stars presented in the sample are shown in Figure 2.1, where the brightness variation is given as parts per million (ppm) in function of the Barycentric *Kepler* Julian Date defined as BKJD = BJD − 2454833.0. The spectral window is computed for each light curve, allowing to have a measurement of the aliasing properties of the discrete timing of the observations (Aerts et al. 2010). Both KIC 6762022 and KIC 10593078 do not show strong side lobes, however KIC 6928997 has stronger side lobes corresponding to a frequency of 0.18 μHz, connected to the missing quarters Q5 and Q9 due to a broken CCD.

The true period spacing $\Delta\Pi_1$ has been previously determined by other authors for two of the proposed red giants. In particular, KIC 6928997 has been studied by Beck et al. (2011), during one of the first detections of dipole mixed modes, where it was classified as an RGB star. Both KIC 6928997 and KIC 10593078 have been investigated by Mosser et al. (2012b), where an early attempt has been done to determine the true period spacing $\Delta\Pi_1$ and the coupling factor q (see Equation 3.21). The retrieved values are $\Delta\Pi_1 = 77.21 \pm 0.02$ s, $q = 0.14 \pm 0.04$ and $\Delta\Pi_1 = 82.11 \pm 0.03$ s, $q = 0.13 \pm 0.04$ for KIC 6928997 and KIC 10593078, respectively.

2.3 Synthetic Dataset

The accuracy and precision obtained for an estimated parameter do not necessarily include all the systematics hidden in the adopted analysis. For this reason, an extra star is included to the final sample. The PSD of this star is simulated from an input frequency list, with their corresponding mode inertia, obtained from a stellar evolutionary code (ASTEC) and a stellar pulsation code (ADIPLS) — the details of these codes are presented in Chapter 4 —. The star has an effective temperature $T_{\text{eff}} = 4950$ K and has a solar metallicity [Fe/H] = 0.00 dex.

The simulator has been developed by De Ridder et al. (2006a), for the simulation of solar-like oscillations seen in MS stars and subsequently further developed by H. Kjeldsen & T. Arentoft. The simulator does not only take the stochastic nature of the solar-like oscillations into account, but also the effects of the stellar background and instrumental noise. These are matched to mimic conditions retrieved from observations made with the

Table 2.1: Literature values for $\nu_{\max}$ and $\Delta\nu$ (Hekker et al. 2011b), as derived by means of the *CAN* method (Kallinger et al. 2010b). The values for T_{eff}, log g and [Fe/H] are those derived by Pinsonneault et al. (2012).

KIC	$\nu_{\max}$ (μHz)	$\Delta\nu$ (μHz)	T_{eff} (K)	log g (dex)	[Fe/H]
6928997	122.57	10.02	4807 ± 86	2.62	0.21
6762022	41.79	4.39	4862 ± 87	2.72	0.01
10593078	204.96	15.34	4971 ± 98	2.88	0.17

Kepler space telescope. Since the simulator has been developed for MS stars and has only been recently modified for red giants, no effects of granulation were included. The instrumental white noise, however, has been taken into account.

The spherical degree ℓ and radial order n_p of the input frequencies for the simulator are already known, due to the output of ADIPLS. Appropriate amplitudes and lifetimes for the oscillations are scaled from the inertia values and the spherical degree, after which stochastic noise is added. The amplitudes of a given mode with degree ℓ at frequency ν are calculated as

$$A_{\ell,\nu} \propto \sqrt{\frac{\mathcal{M}_0}{\mathcal{M}_{\ell,\nu}}} \, , \tag{2.1}$$

where $\mathcal{M}_0$ and $\mathcal{M}_{\ell,\nu}$ are the mode masses of the radial mode and the mode with spherical degree ℓ at a frequency ν for the same radial order. The corresponding lifetime of the modes are approximated by using the relation

$$t_{\text{life}} \propto \sqrt{\mathcal{M}_{\ell,\nu}} \, . \tag{2.2}$$

Both equations are however not fully correct, but they are chosen in order to make the obtained pulsations resemble the solar-like oscillations observed in red giants. These equations are approximations of the full equation

$$H_{\ell,\nu} = \frac{P_{\ell,\nu}}{\eta^2_{\ell,\nu}\mathcal{M}_{\ell,\nu}} \, , \tag{2.3}$$

where $H_{\ell,\nu}$ is the height for a given mode of spherical degree ℓ at a frequency ν and $\eta_{\ell,\nu}$ is the corresponding damping rate for that mode (Benomar et al. 2014). The dependence on the mode mass on the lifetime (Equation 2.2) reflects the distinct behaviour of the g modes and p modes, since modes with a higher mode mass, e.g. the gravity-dominated mixed modes, have a much longer mode lifetime. The simulator has been recently improved to include simulations of solar-like oscillations in red giants and is still in an early testing phase.

The brightness variations induced by the simulated oscillations are added to the light curve of a star having an apparent magnitude $m = 11$. The simulator is built to sample the light curve equidistantly with a sampling rate corresponding to the short cadence mode of *Kepler*, and no gaps are introduced in the sampling. Given that the lifetimes of the solar-like oscillations in most red giants are rather long, the generated light curve is resampled to match the long cadence mode of *Kepler*. Finally a Lomb-Scargle periodogram is computed from the light curve in order to retrieve the corresponding PSD. The frequency resolution changes with the total observing time of the dataset. In order to have a PSD with the same frequency resolution as those of the *Kepler* stars, the simulator also uses a light curve of 1152 days. From now on, the artificial star will be referred to as *Ziva*.

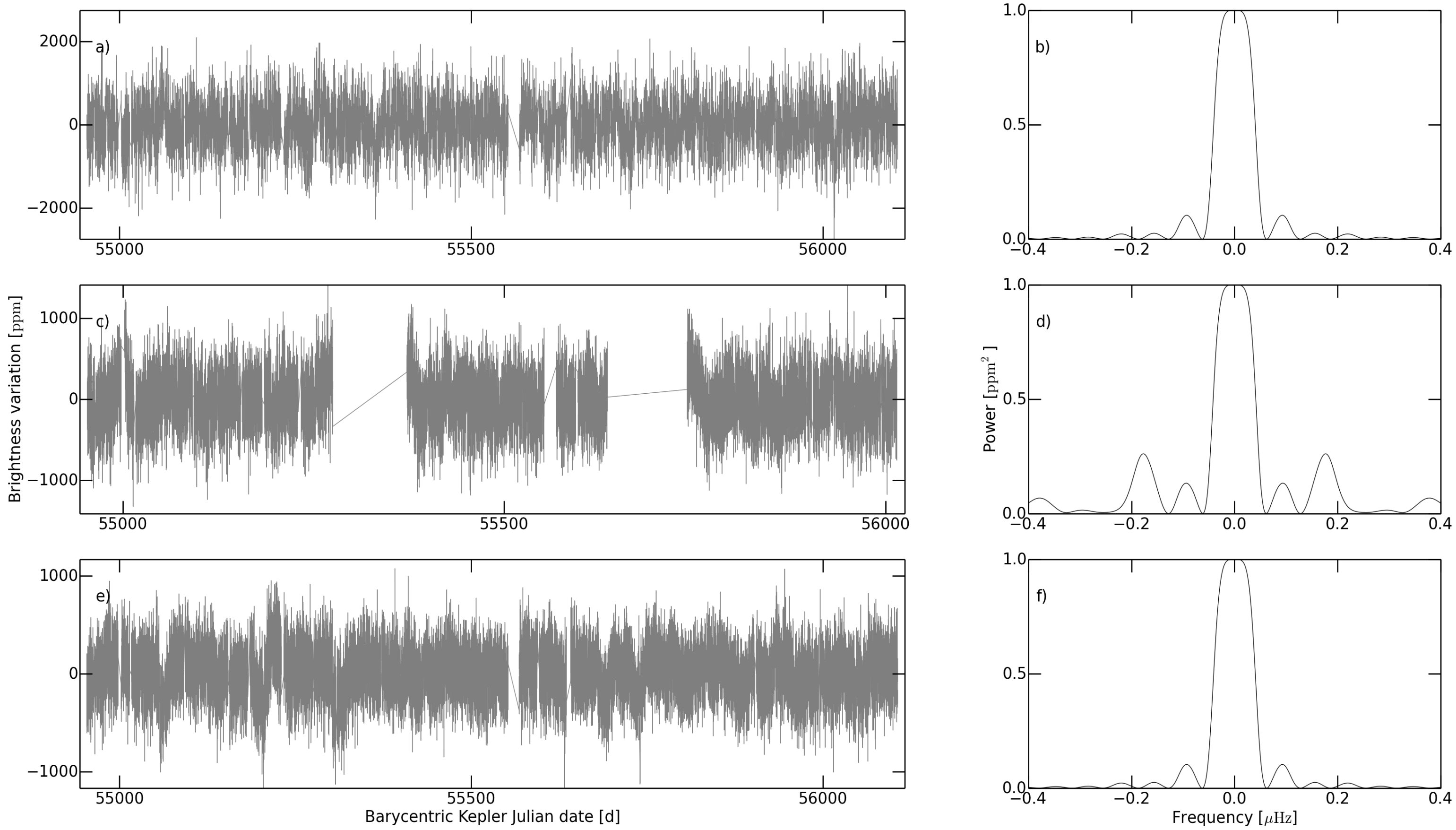

Figure 2.1: The light curves (*left*) and the corresponding spectral windows (*right*) of the three stars used in this work, observed with *Kepler* from Q0 - Q13. *a)* is the light curve for KIC 6762022, while *b)* is the spectral window corresponding to the discrete timing of the observations. *c)* and *d)* are for KIC 6928997 and *e)* and *f)* are for KIC 10593078.

Chapter 3

Seismic Analysis of Mixed Modes for Red Giants observed by *Kepler*

The dipole mixed modes observed in red giants are the main parameters analysed in this thesis, since they can be used to determine the evolutionary state of the red giant. It is however not trivial to measure the frequencies, and their uncertainties, directly from the stars' PSDs. To do so, a repository containing packages to analyse the PSD has been built, written in the scripting language *Python*.

These packages consist of modular pieces of code that can be used in a specific order to deduce different parameters that one intends to retrieve. The first package determines the background in the observed PSD, which can be modelled according to the different contributions expressed in Section 3.1. Once an appropriate description for the background is found, which also determines the frequency of maximum power $\nu_{\max}$, the large frequency separation $\Delta\nu$ is obtained. The method for measuring $\Delta\nu$ is presented in Section 3.2. The derived model for the background is then used to determine the signal-to-noise ratio (SNR) of the different frequency peaks in the PSD. Significant oscillation peaks are subsequently fitted and identified, an analysis hereafter also referred to as peak bagging. The elaborate mechanism of peak bagging is described in Section 3.3. Once the dipole mixed modes are finally identified, the true period spacing $\Delta\Pi_1$ can be determined, as explained in Section 3.4.

3.1 Determining the Background

The PSD of a star showing solar-like oscillations does not only have signal at the characteristic frequencies of the pulsations but it also has multiple background contributions (Kallinger et al. 2010a; Carrier et al. 2010; Kallinger et al. 2014). It is generally assumed that there are two main contributions to the background signal, which are described in the upcoming section. The fitting procedure is subsequently discussed in Section 3.1.2.

3.1.1 Different Contributions

The first component is frequency dependent and it is believed to be linked to different scales of granulation corresponding to different timescales in the PSD. Harvey (1985) originally described these contributions as Lorentzians, after which many variants of the description followed. In this work the description by Kallinger et al. (2010a) is used, which describes the granulation components as a sum of super-Lorentzian profiles

$$B(\nu) = \sum_{i=1}^{3} \frac{2\pi \frac{a_i^2}{b_i}}{1 + \left(\frac{\nu}{b_i}\right)^{c_i}} , \tag{3.1}$$

where a_i is the amplitude of the i-th component, b_i is the characteristic frequency which corresponds to the frequency where the power is half of that at 0 μHz and c_i is related to the decaying time of the physical process involved. In the majority of the stars it is necessary to include three different granulation components although a description with two components can be sufficient in some cases. The different criteria used to determine how many granulation laws are adequate are presented in Section 3.1.2.

The second main contribution to the background is an instrumental white noise component that is described by a constant term. It is mostly visible at frequencies close to the Nyquist frequency $\nu_{\rm Nyq}$, where the astrophysical signal decreases.

An additional term included in the overall background model is the power excess for the region of the PSD where the oscillations are visible. Although it does not correspond to a background signal in the PSD, it has to be taken into account for the proper modelling and description of the other components of the background. The power exess gives rise to the broad hump which is approximately Gaussian and can be modelled as

$$G(\nu) = P_g \exp\left[-\frac{(\nu - \nu_{\rm max})^2}{2\sigma_g^2}\right] . \tag{3.2}$$

The height and width of the Gaussian envelope are respectively P_g and σ_g. $\nu_{\rm max}$ is the central frequency of the envelope and is defined as the frequency of maximum oscillation power $\nu_{\rm max}$. It is an important global asteroseismic parameter of a star, as it is used in the scaling relations (defined in Equation 1.14) to estimate the radius and mass of the star (Chaplin et al. 2011b).

3.1.2 Fitting Procedure

Equation 3.1, which describes the contribution from granulation, and Equation 3.2, corresponding to the Gausian power excess, can be combined to

$$P_{\rm bkg}(\nu) = W + R(\nu) \cdot [B(\nu) + G(\nu)] , \tag{3.3}$$

where W is the white noise contribution, $B(\nu)$ is the sum of the different granulation components, $G(\nu)$ is the Gaussian power excess and the response function $R(\nu)$ is defined as

$$R(\nu) = \mathrm{sinc}^2\left(\frac{\pi\nu}{2\nu_{\rm Nyq}}\right) , \tag{3.4}$$

which takes into account the sampling rate of the observations. Since *Kepler* long cadence data are used, the corresponding Nyquist frequency is $\nu_{\rm Nyq} \approx 283\ \mu$Hz (García et al. 2011).

A least-squares (LS) minimisation with boundaries set for each fitting parameter is used to deduce the best description of the background, according to Equation 3.3. Estimations and/or boundaries for most parameters are deduced in different ways.

Firstly, the PSD is smoothed with a boxcar filter having a width defined by the user (typically 1 μHz). This ensures that possible spikes are not influencing the analysis. The maximum power found corresponds to the first estimation for $\nu_{\max}$. Many different scaling relations between $\nu_{\max}$ and $\Delta\nu$ are proposed, which all describe $\Delta\nu$ as a power law dependent on $\nu_{\max}$ (Hekker et al. 2009; Stello et al. 2009; Huber et al. 2010). The relation by Huber et al. (2010) is adopted, because it has been calibrated on a larger sample of stars, and it reads

$$\Delta\nu = (0.263 \pm 0.009) \cdot (\nu_{\max})^{0.772\pm0.005} \quad . \tag{3.5}$$

The estimate of $\Delta\nu$ (derived by Equation 3.5) is used as the width for the boxcar of the second smoothing, which removes almost all fine structures around the power excess. This allows to retrieve good estimates on the different parameters of the background. The same procedure is used to estimate $\nu_{\max}$ with fitting boundaries set by $\pm\Delta\nu_{\mathrm{estimate}}$. The corresponding power in this region is used as an estimate for the height of the power excess P_g, while the power excess width σ_g is estimated as $\sqrt{2} \cdot \Delta\nu$. The white noise contribution is measured from the average power in the smoothed PSD in the frequency regime 269-283 μHz far from the power excess of stellar oscillations[1].

For the different granulation components, only the lower boundary on a_i is read from the data. The minimum value for a_i is set as

$$\left[(W_{\mathrm{guess}} \cdot 0.95\nu_{\mathrm{Nyq}})/(2\pi)\right]^{1/2} \quad , \tag{3.6}$$

where W_{guess} is the estimated white noise term in the background. This corresponds by definition to the amplitude the granulation law would have given a characteristic frequency of almost the Nyquist frequency. The amplitudes for the initial fit are started from a value of 50 ppm. The lower and upper boundaries for the slope c_i are respectively 2 and 4. It is however common to fix the slope to a value of 4 (Kallinger et al. 2010a; Carrier et al. 2010), although it can be left as a free parameter since it can also vary from star to star. Mosser et al. (2012a) state that a slope of $c_i = 2$ might be better for granulation laws at low frequencies, while $c_i = 4$ does a better job in describing the frequency dependence at higher frequencies. Recently, Kallinger et al. (2014) found that a slope of 4 might be the most suitable value. In order to ensure higher freedom during the fitting process and at the same time avoid using too many assumptions on the background model, the slope of the individual Harvey-like components is let to vary in the range $2 - 4$.

For discriminating between the models of the background with either two or three granulation components, the Akaike Information Criterion (AIC) and the Bayesian Information Criterion (BIC) are adopted (Akaike 1974; Schwarz 1978). Both criteria are used in model fitting, because they provide a balance between the goodness-of-fit and the number of free parameters involved in the model. The AIC and BIC are defined as

$$\mathrm{AIC} = 2k - \ln\left(\chi^2\right) \;\text{ and} \tag{3.7}$$

$$\mathrm{BIC} = 2\ln\left(\chi^2\right) + k \cdot \ln\left(N\right) \quad , \tag{3.8}$$

where k is the number of degrees of freedom, N is the number of data points and χ^2 is the reduced chi-squared determined for the model. If both the AIC and the BIC for

[1] Extra care has to be taken for stars which have $\nu_{\max}$ close to this region, as the power excess will influence the estimation of the white noise component.

the three-components background model are smaller than for the two-component model, the former is accepted over the latter, meaning that despite of the larger number of free parameters, the more complex model provides a considerable better fit to the data (Liddle 2004). The difference in AIC and BIC between the models is expressed as a fraction, accepting the three components fit if $AIC_3/AIC_2 < 1$ and $BIC_3/BIC_2 < 1$, where the index 2 relates to the background with two granulation components and 3 to the three components background.

An example for a background fitting is given in Figure 3.1, where the background for KIC 8366239 is represented by the red line. The dashed red line includes the additional term representing the Gaussian power excess. The individual contributions used in the fit are indicated by the black dashed lines, while the second smoothing of the PSD by means of a boxcar having a width of approximately $\Delta\nu$ is given by the blue solid line and is used for giving an indication of the background level present in the data.

When a reasonable description of the background is found using the LS minimisation, it is then used by a Bayesian Markov Chain Monte Carlo (MCMC) algorithm (Berg 2004). The Bayesian inference for the parameters describing the model of the background (Equation 3.3) is calculated (Duvall & Harvey 1986; Anderson et al. 1990; Handberg & Campante 2011; Corsaro et al. 2013). A probability $p(\Theta|D, I)$ is assigned to each set of parameters Θ of the background, for the data D of the PSD and available prior information I, retrieved from previous observations or restricted by theoretical considerations. This

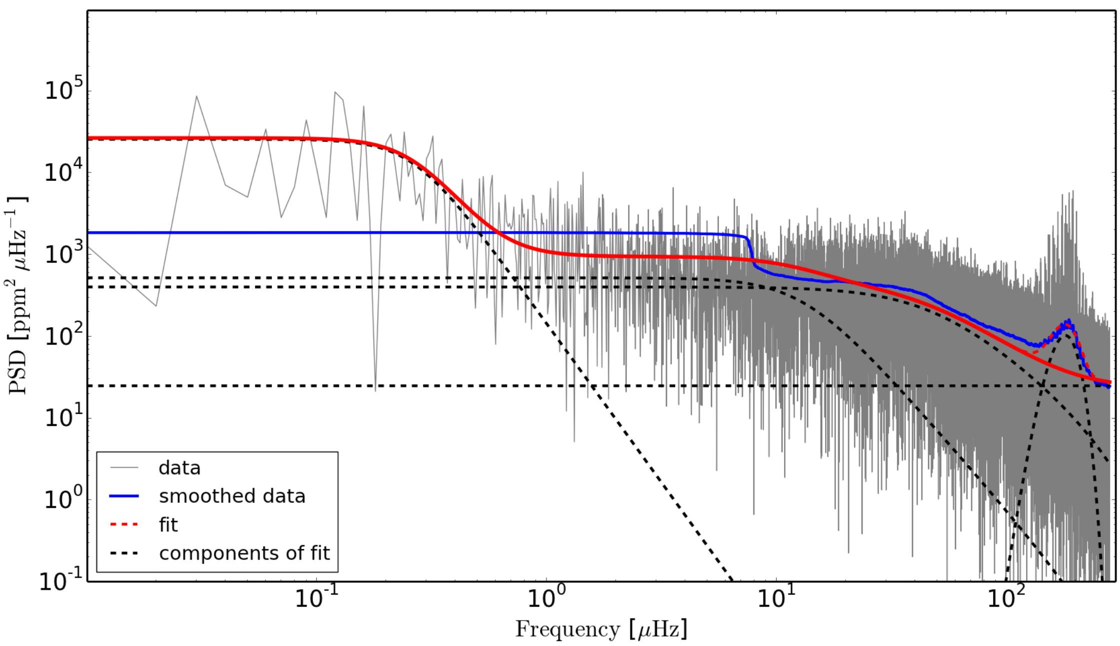

Figure 3.1: Resulting background fit (red line) to the PSD (gray) of KIC 8366239. The red dashed line is when the Gaussian envelope is included. The individual contributions are given by the black dashed lines. The smoothed PSD with a filter width of roughly $\Delta\nu$ is given in solid blue. The jump in the smoothed curve is an artifact induced by the logarithmic scale of the figure.

is done through the Bayes' theorem,

$$p(\Theta|D, I) = \frac{p(\Theta|I)p(D|\Theta, I)}{p(D|I)} \ . \tag{3.9}$$

$p(\Theta|I)$ is defined as the *prior probability*, which describes the probability of the model with the parameter set Θ in the absence of D, and $p(\Theta|D, I)$ is the *posterior probability* when the information about the data D is included. The *likelihood of the parameter* set Θ for the model is defined as $p(D|\Theta, I) = \mathcal{L}(\Theta)$ and the *marginal likelihood* for all the hypotheses is defined as $p(D|I)$.

A uniform prior is used for all the parameters and the likelihood $\mathcal{L}(\Theta)$ is described as (Duvall & Harvey 1986; Anderson et al. 1990)

$$\mathcal{L}(\Theta) = \sum_{\nu} \ln(\mathrm{model}(\Theta; \nu)) + \frac{\mathrm{PSD}(\nu)}{\mathrm{model}(\Theta; \nu)} \ . \tag{3.10}$$

The model depends on the parameters Θ and describes the background in the PSD. ln is the natural logarithm and the summation is made to obtain a unique value for a given parameter set Θ.

The Bayesian MCMC is set up for 30 walkers, which are the independent chains in the MCMC. The initial position for these walkers is set as a Gaussian ball around the values derived from the LS minimisation fit. The Gaussian ball is constructed as a random position around the derived input values obtained by the LS fit. The standard deviation of this random position is typically in order of 10^{-3} times the input value. The walkers are left to burn-in, i.e. feel the possible parameter space until a certain level of convergence is reached. Once convergence is reached, the *marginal posterior probability distribution* is obtained using a given set of steps for the walkers. The marginal probability distribution is a one-dimensional distribution that contains all the information required for the free parameter Θ_k it corresponds to (e.g. mode, mean, median and Bayesian credible intervals).

The final description of the background is then done using the median value of the marginal distribution, because it is preserved by any change of variable. The difference between the result deduced with the LS minimisation and with the Bayesian MCMC is provided in Figure 3.2.

3.2 Determination of $\Delta\nu$

Once the background has been described, the global large frequency separation $\Delta\nu$ can be measured. According to Hekker et al. (2011b) there are several methods to determine the global $\Delta\nu$. It is possible to take a power spectrum of the PSD of the star, which will show the different characteristic frequency separations present in the oscillation diagram. A similar result is retrieved when the auto-correlation function (ACF) of the PSD is calculated. When calculating the cross-correlation of the PSD with itself, the main frequency separation and their harmonics are retrieved. The method of the ACF has been chosen because it has an easier implementation.

The ACF is calculated in the PSD of the star for the region $\nu_{\mathrm{max}} \pm 2\Delta\nu_{\mathrm{estimate}}$, where $\Delta\nu_{\mathrm{estimate}}$ is deduced from the scaling relation defined in Equation 3.5. The choice of adopting this frequency interval is motivated as follows: (i), $\Delta\nu$ is often referred to as a

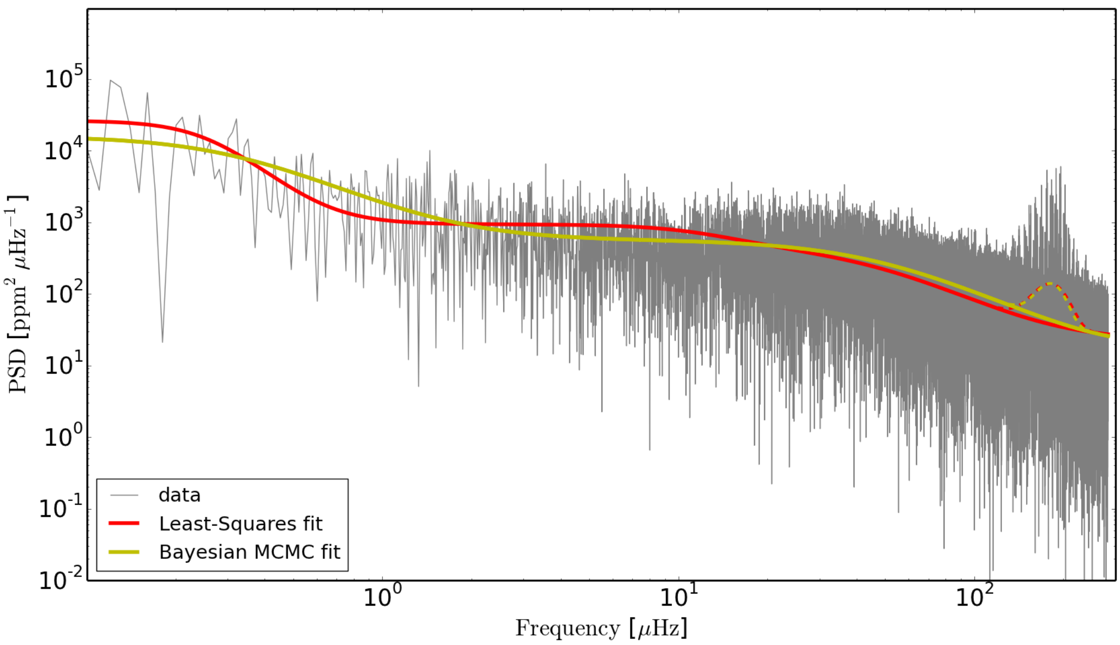

Figure 3.2: The resulting background fit using the Bayesian approach (solid yellow line) to the PSD (gray) of KIC 8366239. The initial estimation using the LS minimisation is given by the red solid line. The yellow (red) dashed line represent the model of the background together with the Gaussian power excess.

global parameter of the star, but it is known by previous works (Kallinger et al. 2010a; Mosser et al. 2010), that this parameter can vary between different radial orders, with a mean value depending on how many radial orders have been taken into account. This can add an extra uncertainty in the determination of $\Delta\nu$ using all radial orders in the power excess; (ii), when radial orders further away from $\nu_{\rm max}$ are investigated, the oscillation modes therein have a lower height in the PSD as compared to that of the modes close to $\nu_{\rm max}$. This is reflected in the average number of significant radial orders, discussed in Section 3.3. Typically three to five significant radial orders are found in the PSD of a red giant. The non-significant radial orders are therefore discarded in order to avoid extra uncertainty on $\Delta\nu$.

The large frequency separation $\Delta\nu_{\rm estimate}$ is used as a first estimation for $\Delta\nu_{\rm global}$. The maximum in the ACF in the interval $0.75 - 1.25 \cdot \Delta\nu_{\rm estimate}$ is searched, instead of the global maximum in the ACF[2]. In a second step, this maximum is fitted with a Lorentzian function to be less sensitive to the frequency resolution of the ACF. The function is given as

$$P_{\Delta\nu}(\nu) = B + \frac{P_{\rm ACF}}{1 + 4\left(\frac{\nu-\nu_0}{\Gamma}\right)^2} \ , \tag{3.11}$$

where $P_{\rm ACF}$, Γ and ν_0 are the amplitude, Full Width at Half Maximum (FWHM) and

[2]The global maximum in the ACF of the PSD is always at 0 μHz, corresponding to no shift between the signal and itself. A maximum here is referred to as a peak in the ACF with a non-zero frequency shift.

the central frequency respectively of the Lorentzian, while B is a uniform background. The deduced ν_0 of the Lorentzian profile is then the large frequency separation $\Delta\nu$ for the radial orders considered in the PSD. An example of the determination of $\Delta\nu$ for KIC 8366239 is given in Figure 3.3.

Once a reliable estimate has been obtained for $\Delta\nu$, a Bayesian MCMC is used to determine the most likely value and the uncertainty on the large frequency separation. The fitting of the Lorentzian profile to the ACF is repeated, using the Bayesian method. Uniform priors are set on the fitting procedure and the likelihood function presented in Equation 3.10 is used. The median value of the marginal distribution is used as the most likely value for $\Delta\nu$.

3.3 Peak Bagging

Once the global asteroseismic parameters for the star are deduced, the individual oscillations modes have to be extracted and identified. This is done under the term peak bagging, an analysis performed in the context of asteroseismology of solar-like oscillations, which is illustrated here as the combination of three different processes. The first process decides whether a given peak in the PSD is significant. When a peak is deemed significant, it has to be described with an appropriate profile. Finally mode identification has to be done for assigning the spherical degree ℓ, radial order n_p, and in case of rotation present in the star the azimuthal order m.

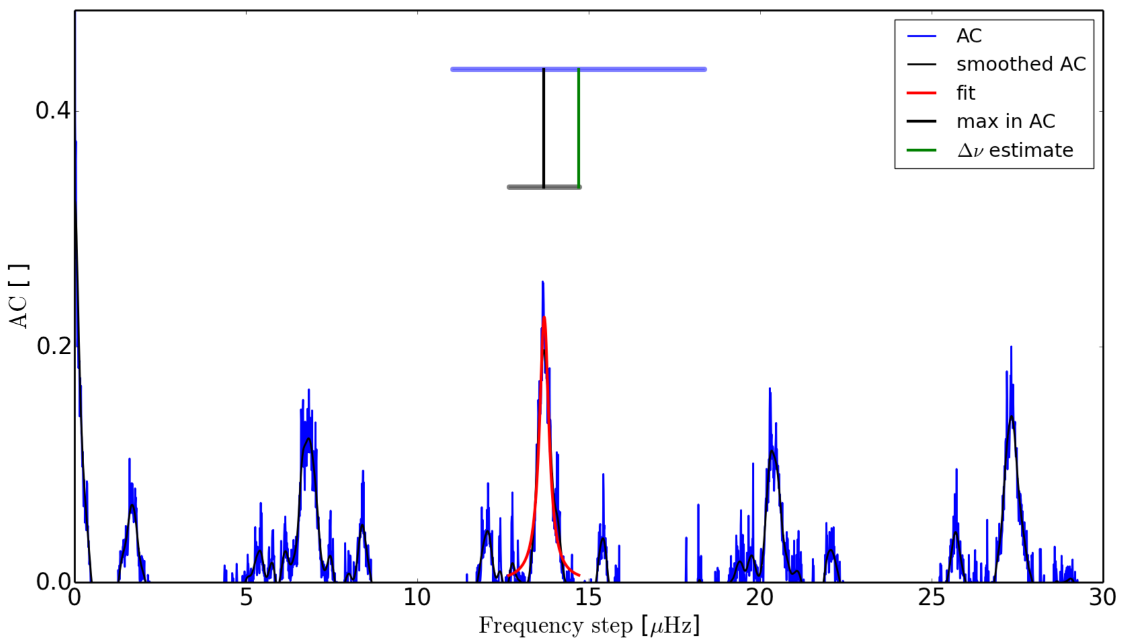

Figure 3.3: The determination of $\Delta\nu$ for KIC 8366239, where the ACF is given in blue. The green line represents the estimate for $\Delta\nu$, obtained from Equation 3.5. The maximum in the ACF shaded blue region (i.e. the search interval) is fitted by a Lorentzian profile (red line) to determine $\Delta\nu$. The deduced large frequency separation is given by the black line.

A more detailed discussion is given in this section since there are many possible methods to both measure and extract the mode peak parameters, which can produce differences in the final results. The different assumptions made are discussed in the following sections together with the adopted techniques. First, peak bagging is done by an automated algorithm. The selected peaks with their asteroseismic parameters estimated from the fit are passed to a second interactive step, where the user is presented with a Graphical User Interface (GUI) in which peaks can be added, deleted and modified. When the user decides that all peaks are reasonably well described by the LS fitting, a Bayesian MCMC is used to compute the marginal distribution of each parameter. The step for the automated peak bagging is discussed in Section 3.3.1, the interactive method using the GUI in Section 3.3.2, and the final approach using a Bayesian MCMC in Section 3.3.3.

3.3.1 Automated Pipeline

The first step in the automated peak bagging consists of testing the significance of a given peak in the PSD. A possible solution is to define a SNR and use a certain threshold to deem a peak meaningful. The method to evaluate the SNR implemented in the pipeline consists of dividing the PSD by the fitted background. The contribution of the power excess to the fitted background is disregarded, since this would influence the peaks in the PSD. The SNR is defined as

$$\mathrm{SNR} = \frac{\mathrm{PSD}}{W + R(\nu) \cdot B(\nu)} \,, \tag{3.12}$$

where the denominator corresponds to the definition of the background given in Section 3.1. The significance threshold is defined as an integer times the average SNR in the radial order. When a peak surpasses 6 to 8 times the average SNR, it is very likely to be connected to an oscillation mode and not an artifact of noise (Aerts et al. 2010). It is noted that this method relies on the height of the mode, which not always resembles the total power stored in the mode, making it possible to miss some modes having lower height. The rotations effect of the star will split the total power of the mode over all peaks of the multiplet, while effects of a bad spectral window might give rise to strong side lobes in the PSD. However, both effects are expected to have minor influence during the mode extraction for the sample of stars presented in Section 2.2. This is because the stars do not show evidence of rotation in the observed oscillations and the duty cycle of *Kepler* observations is adequate for avoiding prominent side lobes in the PSD.

As it follows from the theory of solar-like oscillations, the peaks retrieved from the oscillation diagram are represented by a Lorentzian profile (Gizon & Solanki 2003; Aerts et al. 2010; Carrier et al. 2010; Bedding et al. 2010; Beck et al. 2012). However this only holds when a peak is fully resolved, i.e. when the FWHM of the mode peak is substantially larger than the frequency resolution of the PSD (Chaplin et al. 2005; Aerts et al. 2010). The implementation of a Lorentzian profile for a single peak, and with the previously previously fitted background included, is given as

$$P_{\mathrm{mode}}(\nu) = W^{*} + R(\nu) \cdot \left[B^{*}(\nu) + \frac{H}{1 + 4\left(\frac{\nu - \nu_0}{\Gamma}\right)^2} \right] \,, \tag{3.13}$$

where $R(\nu)$ is the response function defined in Section 3.1, and W^{*} and $B^{*}(\nu)$ is the description for the white noise component and the granulation components derived by means of the Bayesian MCMC fit to the background of the PSD. The height, the FWHM and the central frequency of the Lorentzian profile are given by H, Γ and ν_0, respectively. It is however known that a strong correlation exists between the height and the FWHM of the Lorentzian profile. This causes the fitting process, done by means of the LS minimisation method, to be unstable. The conversion from height to amplitude (e.g. see Barban et al. 2007) leads to a profile defined as

$$P_{\mathrm{mode}}(\nu) = W^* + R(\nu) \cdot \left[B^*(\nu) + \frac{A^2}{\pi \Gamma} \frac{1}{1 + 4\left(\frac{\nu - \nu_0}{\Gamma}\right)^2} \right] \,, \tag{3.14}$$

where A is now the amplitude of the Lorentzian profile, allowing for a more stable fitting process.

The automated fitting of the significant peaks is done in two steps. At first, an individual fit for each peak that passed the significance criterion is performed, by using the Lorentzian profile with the background of the PSD as defined in Equation 3.14. The deduced parameters from each individual fit are stored and passed to the second step. Before the second step starts, a quick mode identification is performed, in order to identify the spherical degree ℓ for each mode. All the dipole ($\ell = 1$) and octupole ($\ell = 3$) modes are passed, while only one radial ($\ell = 0$) and one quadrupole ($\ell = 2$) mode are forced in their appropriate regions. This ensures that false-positive radial modes, which can happens if the resolution of the fitting is too low, are discarded. It also makes mode identification safer as dipole mixed modes can be seen in this region. However, care is needed in any case because the identification process is not straightforward. The dipole and octupole modes, together with the radial and quadrupole modes are passed to the second step which fits all the modes together for the full radial order n_p. This allows to take possible couplings in the fitting process between the different modes into account.

The method itself is presented in pseudo-code format in Algorithm 3.1. The mode extraction is performed for each radial order independently of the others. Except for the frequency, PSD, SNR, $\Delta\nu$ and ν_{max}, an initial guess for the frequency position of the central radial mode closest to ν_{max} is required. The frequency position of this mode, $\nu_{\ell=0,\mathrm{central}}$, serves as a scaling parameter to move to different radial orders, and is refined by a preliminary fit.

From $\nu_{\ell=0,\mathrm{central}}$, the different radial orders are cut in frequency from

$$\nu_{\ell=0,\mathrm{central}} - (\Delta n_p + 0.2) \cdot \Delta\nu \text{ to } \nu_{\ell=0,\mathrm{central}} + (\Delta n_p + 0.8) \cdot \Delta\nu \,,$$

where Δn_p states the difference between the chosen and the central radial order. The corresponding PSD is cut for this frequency region and the SNR is calculated. Subsequently all the chunks of PSD and frequency are sorted according to descending SNR.

In the sorted SNR, the first element is tested to pass the given criterion and if the condition is satisfied, the corresponding frequency and PSD are extracted for this position. A frequency region in the PSD is selected from this frequency position having a width $2.5Res$, where the desired resolution, Res, is set by the user as a minimum frequency interval to discriminate between consecutive frequency peaks. It has been found that the parameter depends little on the frequency of maximum power ν_{max}, hence a value of 0.2 μHz is often reasonable for red giants not showing rotational splitting. The selected frequency region is fitted with a Lorentzian profile, as defined in Equation 3.14, and the parameters characterising the profile are stored for subsequent calculations. From the extracted frequency position a different frequency region is chosen with a width of Res, together with the corresponding SNR. The SNR values corresponding to the selected regions of the PSD are removed from the total array of SNR values in order to provide the peak witha certain width — hence the term Res — in the SNR array. This process corresponds to recalculating the SNR every time the most significant oscillation peak is fitted and removed from the PSD and it continues until the first element of the sorted SNR no longer satisfies the given threshold.

A mode identification is performed for the retrieved peaks, which needs the description of the surface term ϵ and the radial order n_p (Mosser et al. 2011). This leads to a phase shift

$$\theta = (\nu/\Delta\nu) - (n_p + \epsilon) \ , \tag{3.15}$$

where the phase shift has a value in the interval $[-0.2,\ 0.8[$. For this phase shift it has been shown that the radial modes have $\theta \approx 0.00$ and quadrupole modes have $\theta \approx -0.12$, the interval $]0.1,\ 0.2[$ has been chosen for the $\ell = 3$ modes, while the $\ell = 1$ modes correspond to the region $[0.2,\ 0.8[$. The surface term ϵ can be deduced for each radial order, by using the assumption that $\theta = 0$ for these modes and that the radial order n_p can be obtained by $\lfloor \nu_{\ell=0}/\Delta\nu \rfloor - 1$. The dipole and octupole frequencies are then passed to the global fitting for the complete radial order.

3.3.2 Interactive Pipeline

The fitting parameters deduced during the automated peak bagging are now passed to the interactive pipeline, where both the frequency échelle and the PSD act as a GUI. Here the user can add or delete the identified peaks, run the fitting procedure again or start the Bayesian MCMC algorithm required for the determination of the marginal distributions for all the fitting parameters.

The output from the automated peak bagging is represented in a graphical manner. The fit is overlaid on the PSD for each radial order, the peaks are indicated in a different colour coding and symbol depending on the spherical degree ℓ. A frequency échelle is also produced in which the frequencies have been corrected for the surface term ϵ by using the phase shift θ (Equation 3.15). The SNR threshold criterion is translated to PSD units and indicated on the GUI to help the user. An example of this screen is given in Figure 3.4 for KIC 8366239.

Table 3.1 presents the different possibilities given during the usage of the GUI. The command for adding or deleting the identified peaks is independent of the refitting of the radial orders, as the user may want to change more frequencies before running the fitting procedure. The fitting procedure is exactly the same as the second step from the automated peak bagging. It uses the previous run as an initial guess and uses the same fitting boundaries provided by the frequency region in the individual peak bagging.

3.3.3 Distribution of the Parameters

When the option '*b*' has been chosen in the GUI of the interactive peak bagging (Table 3.1), the Bayesian MCMC is addressed to calculate the distributions of all the different parameters of the fitting. This is again separately done for each radial order.

Algorithm 3.1 Pseudo code for the automated peak bagging which runs per radial order. The peak bagging consists out of two steps, as explained in the text.

```
In: frequency, PSD, SNR, number of radial orders, $\Delta\nu$,
    background model, desired resolution, threshold,$\nu_{\ell=0,\mathrm{central}}$
for radial order in chosen radial orders do
    Cut PSD, SNR and frequency out for order
    Sort cut according to decreasing SNR

    procedure PEAK RETRIEVAL AND INDIVIDUAL FITTING
        while SNR[0] > threshold do
            Build fit region:
            freq_sort[0] $\pm$ 2.5 $\cdot$ desired resolution
            corresponding PSD

            fit using Lorentzian profile
            save parameters

            delete region:
            freq_sort[0] $\pm$ desired resolution
            corresponding PSD and SNR
        end while
        Mode identification for found peaks
        Pass all $\ell = 1$ and $\ell = 3$ peaks
    procedure FITTING FOR THE FULL RADIAL ORDER
        Force one $\ell = 0$ peak at $\nu/\Delta\nu - (n_p + \epsilon) = 0.00$
        Force one $\ell = 2$ peak at $\nu/\Delta\nu - (n_p + \epsilon) = -0.12$
        Use all $\ell = 1$ and $\ell = 3$ peaks
        Set appropriate fitting intervals for each peak

        Fit for complete radial order using Lorentzian profiles

        Mode identification

    Plotting
end for
Out: For all frequencies:  frequency, amplitude, FWHM, $\ell$, $n_\mathrm{p}$
```

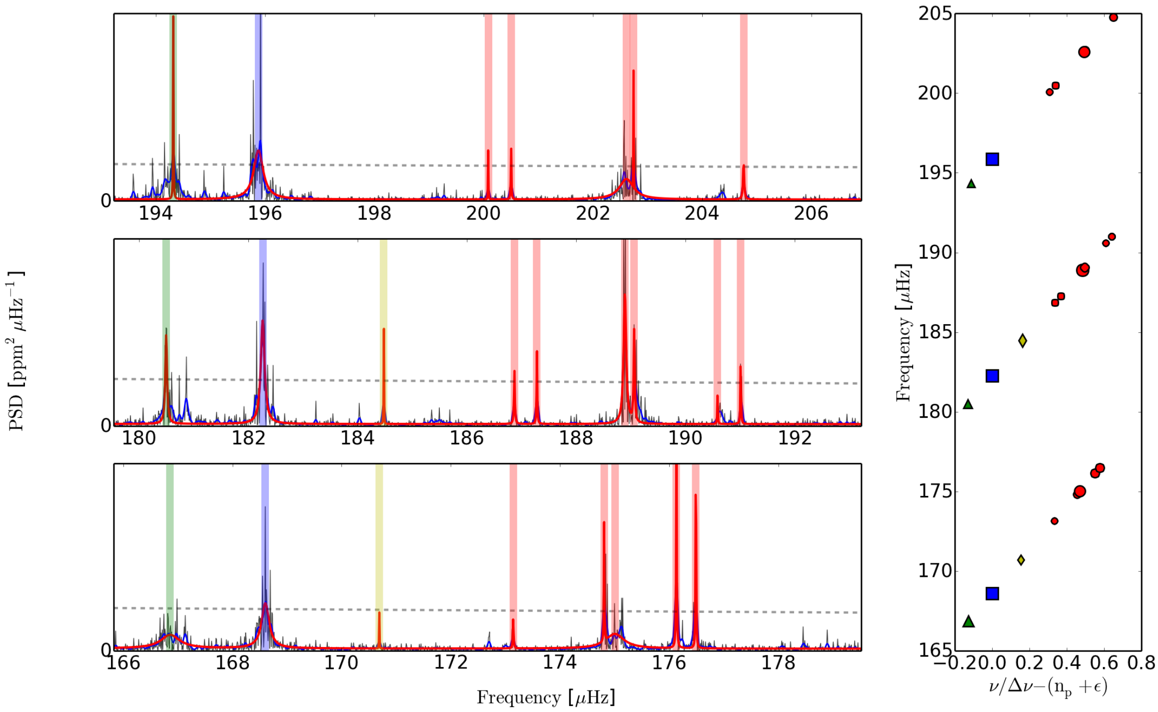

Figure 3.4: Example of the GUI presented during the interactive peak bagging for KIC 8366239. *Left:* The radial, dipole, quadrupole and octupole modes are respectively indicated by the blue, red, green and yellow shaded region in the PSD. The PSD itself is given in black, smoothed with a moving boxcar of 0.1 μHz in blue and the initial fit in red. The dashed line represents the SNR threshold. *Right:* The frequency échelle diagram on which the $\ell = 0$, 1, 2 and 3 modes are indicated by blue squares, red dots, green triangles and yellow diamonds respectively. The marker size for each radial order is related to the amplitude of the peak.

Table 3.1: The different options that can be used during the interaction with the GUI for interactive peak bagging.

Command	Usage
a	add a new peak close to the frequency of the cursor
e	add a new peak exactly at the frequency of the cursor
d	delete the peak closest to the frequency of the cursor
r	rerun the fitting with added/deleted frequencies
b	run the Bayesian MCMC to get distributions
p	print the deduced fitting parameters in the terminal
s	save the output and exit the GUI
x	exit the GUI without saving
h	help, prints the commands in the terminal

The likelihood $\mathcal{L}$ defined in Equation 3.10 is used for fitting the significant frequencies in each radial order. An uniform prior is used for the central frequency and the amplitude of the Lorentzian profile, while a modified Jeffreys' prior is used for the FWHM. This type of prior allows to maintain a finite width for the unresolved peaks, since they most likely have a FWHM smaller than the frequency resolution. Handberg & Campante (2011) defined the modified Jeffreys' prior as

$$p(\Theta, I) = \prod_k f_k(\Theta_k) = \prod_k \left(\Theta_k + \Theta_k^{\mathrm{uni}} \ln \left[\Theta_k^{\mathrm{uni}} + \frac{\Theta_k^{\mathrm{max}}}{\Theta_k^{\mathrm{uni}}} \right] \right)^{-1} , \tag{3.16}$$

where $p(\Theta, I)$ is the prior probability for the parameter set Θ and Θ_k^{max} gives the upper boundary in the parmeter space for Θ_k. For $\Theta_k \gg \Theta_k^{\mathrm{uni}}$, Equation 3.16 behaves like a Jeffreys' prior, while for $0 \leq \Theta_k \ll \Theta_k^{\mathrm{uni}}$ it behaves like an uniform prior. Θ_k^{uni} marks the transition between the two regimes. The median value of the distribution is seen as the true value for the parameter, while the differences between the median value and the 16%-percentile and 84%-percentile correspond respectively to the lower and upper uncertainty on the fitting parameter.

3.4 Determination of $\Delta\Pi_1$

Once all the significant frequencies are retrieved and the mode identification is complete, one can determine the true period spacing of the dipole mixed modes $\Delta\Pi_1$. The determination of $\Delta\Pi_1$ is done in two steps. (i) the period spacing between consecutive dipole mixed modes is measured. When these are set as function of their phase shift θ, they can be fitted with a continuum subtracted by a Lorentzian profile. The deduced continuum estimates the true period spacing $\Delta\Pi_1$; (ii) the asymptotic relation defined by Mosser et al. (2012b) is subsequently used to deduce both the true period spacing $\Delta\Pi_1$ and the coupling factor q.

3.4.1 Estimating $\Delta\Pi_1$ from Period Spacings

The first step to describe the true period spacing $\Delta\Pi_1$ is by measuring the observed period spacing ΔP between consecutive dipole mixed modes, formally defined as

$$\Delta P = \frac{10^6}{\nu_{1,n_p,\ell=1}} - \frac{10^6}{\nu_{2,np,\ell=1}} . \tag{3.17}$$

The frequencies of the two consecutive dipole mixed modes are $\nu_{1,n_p,\ell=1}$ and $\nu_{2,n_p,\ell=1}$, of which $\nu_{1,n_p,\ell=1}$ is the lowest frequency. An average phase shift $\theta = (\theta_{1,\ell=1} + \theta_{2,\ell=1})/2$, as defined by Equation 3.15, is assigned for each measured period spacing ΔP. These can then be fitted by a flat continuum, which is the estimation for $\Delta\Pi_1$, and a Lorentzian profile with negative amplitude. This is the empirical approach, proposed by Mosser et al. (2012b). A LS minimisation method is used to fit the Lorenzian profile to the observed period spacings.

An example for this fit is provided in Figure 3.5, where the full black line represents the best fit of a Lorentzian subtracted from a continuum and the measured period spacings are given by black dots. The flat continuum of the model estimates $\Delta\Pi_1$ and it is later refined by the gridsearch method for the asymptotic relation.

This method has however one major drawback, which is when a dipole mixed mode is missed due to the significance criterion, leaving a gap in the range of consecutive mixed modes. Therefore, the observed ΔP will be larger because one frequency has been skipped. This will make the estimation of $\Delta\Pi_1$ harder if the user does not take precautions. Nevertheless, even in case this event occurs, it is not of the extent to produce a misidentification of the evolutionary stage of the star.

The uncertainty on the deduced $\Delta\Pi_1$ is determined by using a MCMC, where ΔP and θ are randomly varied within the propagated uncertainties for a large number of steps. The propagated uncertainties on ΔP and θ are

$$\sigma(\Delta P)^2 = \left(\frac{10^6\sigma(\nu_{1,n_p,\ell=1})}{\nu^2_{1,n_p,\ell=1}}\right)^2 + \left(\frac{10^6\sigma(\nu_{2,n_p,\ell=1})}{\nu^2_{2,n_p,\ell=1}}\right)^2 , \tag{3.18}$$

$$\sigma(\theta_{i,n_p,\ell=1})^2 = \left[\left(\frac{\sigma(\nu_{i,n_p,\ell=1})}{\nu_{i,n_p,\ell=1}}\right)^2 + \left(\frac{\sigma(\nu_{\max})}{\nu_{\max}}\right)^2\right]\theta^2_{i,n_p,\ell=1} \quad \text{and} \tag{3.19}$$

$$\sigma(\theta)^2 = \left(\frac{1}{2}\right)^2\sigma(\theta_{1,n_p,\ell=1})^2 + \left(\frac{1}{2}\right)^2\sigma(\theta_{2,n_p,\ell=1})^2 . \tag{3.20}$$

The set of randomly varied ΔP and θ is fitted with the Lorentzian profile and the flat continuum to estimate $\Delta\Pi_1$. Subsequently, the standard deviation on the set of $\Delta\Pi_1$is chosen as the uncertainty on the deduced $\Delta\Pi_1$ of the initial LS fit.

3.4.2 Gridsearch Method for Multi-Parameter Fit of Asymptotic Relation

Once the true period spacing $\Delta\Pi_1$has been deduced from the previous fit, a gridsearch analysis is performed in order to determine the final $\Delta\Pi_1$ with higher accuracy and precision. The true period spacing for a star can be obtained by using the asymptotic relation proposed by Mosser et al. (2012b)

$$\nu = \nu_{\mathrm{n_p},\ell=1} + \frac{\Delta\nu}{\pi}\arctan\left[q\,\tan\left(\frac{1}{\Delta\Pi_1\nu} - \epsilon_g\right)\right] . \tag{3.21}$$

The frequencies of the dipole mixed modes ν are coupled to the frequency of the pure p mode $\nu_{\mathrm{n_p},\ell=1}$. The coupling factor q describes the strength of the coupling between the gravity mode cavity and the pressure mode region and has typically a value between 0.1 and 0.3, where 0 states that there is no coupling present. The constant ϵ_g is a normalisation phase, which ensures that the g mode periods are close to $(n_g + 1/2 + \epsilon_g)\Delta\Pi_1$ in case of weak coupling. However, for simplicity the term $1/2 + \epsilon_g$ is assumed to be constant and set to zero, which is also done in Mosser et al. (2012b).

According to this, a bi-dimensional grid along the coordinates $\Delta\Pi_1$ and q is constructed. The frequencies of the dipole mixed modes are calculated using the asymptotic relation for each $(\Delta\Pi_1, q)$ pair in the grid from a *Python* library written by Beck (2013). These frequencies are then compared to the observed frequencies, deduced from the PSD

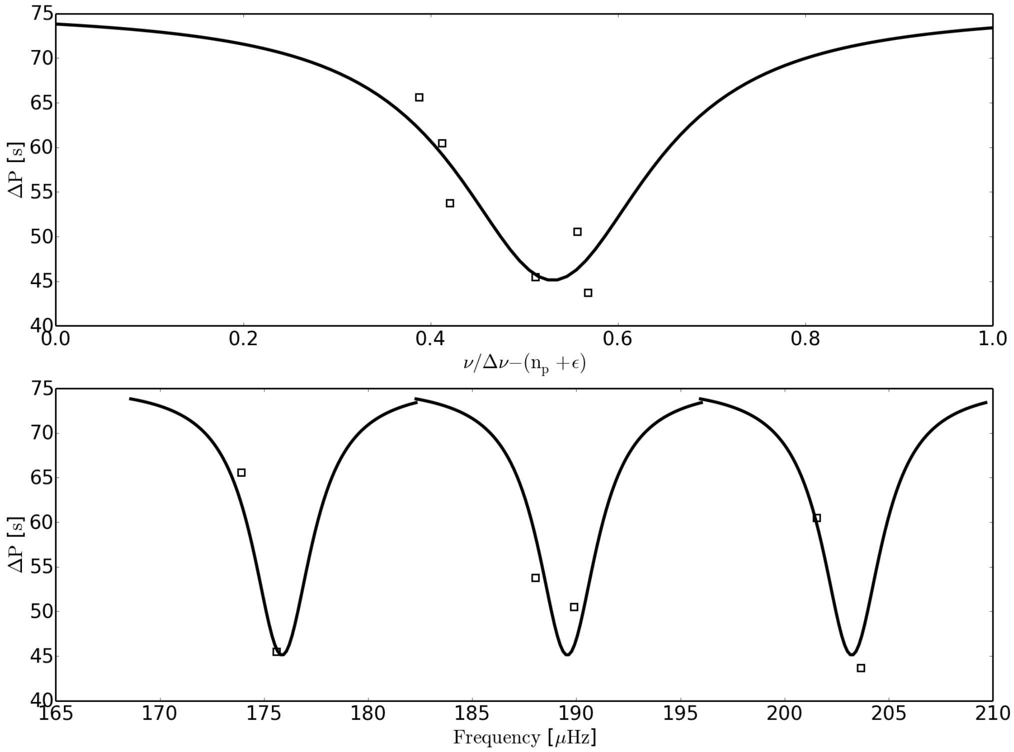

Figure 3.5: *Top:* The fit through the observed period spacings ΔP for the dipole mixed modes using a model with a flat continuum and a Lorentzian with negative amplitude for KIC 8366239. This flat background is the initial guess for the true period spacing $\Delta\Pi_1$. ΔP is presented as a function of the phase shift θ (Equation 3.15). *Bottom:* The same Lorentzian fit, but extrapolated from θ to ν.

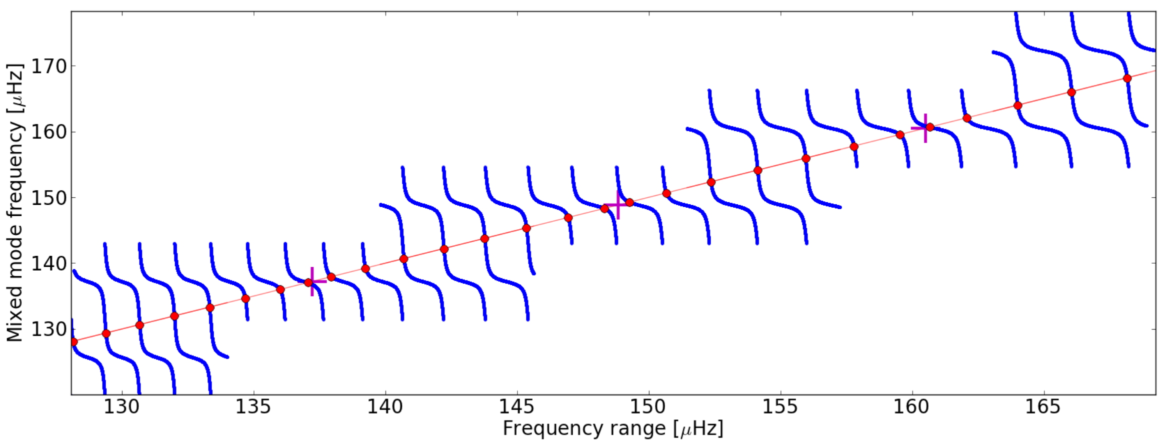

Figure 3.6: Determination of the frequencies of the dipole mixed modes according to the asymptotic relation, Equation 3.21, for a red giant with $\Delta\nu = 11.6$ μHz and $\Delta\Pi = 77.2$ s. The tangent function showing all possible solutions of the right hand side of Equation 3.21 is given in blue. The red line indicates the position where the frequency of the vertical axis equals the horizontal axis. The deduced frequencies for the mixed modes are indicated by red dots, derived by the intersection between the tangent curve and the straight line. The magenta crosses indicate the position of the pure pressure dipole modes. Figure taken from Beck (2013).

of the star, and a normalised χ^2 is calculated. The best pair of values is accepted as the final result. The chi-squared is defined as

$$\chi^2_{\text{grid}} = \frac{1}{N-2-1}\sum_{i}^{N}\left(\frac{\nu_{\ell=1,i,\text{obs}} - \nu_{\ell=1,i,\text{asympt}}}{\sigma(\nu_{\ell=1,i,\text{obs}})}\right)^2 , \tag{3.22}$$

where $\nu_{\ell=1,i,\text{obs}}$ is the frequency of the i-th observed mixed mode, $\nu_{\ell=1,i,\text{asympt}}$ is the corresponding frequency, from the asymptotic relation (closest to the i-th observed mixed mode), and $\sigma(\nu_{\ell=1,i,\text{obs}})$ is the uncertainty estimated by means of the Bayesian MCMC fit. The χ^2_{grid} (Equation 3.22) is normalised to the degrees of freedom $N-2-1$, where N is the number of observed dipole mixed modes, the term -2 is inserted as there are two fitting parameters, q and $\Delta\Pi_1$, while the term -1 is introduced since an observed data sample is used.

As the asymptotic relation is an implicit relation for ν, no analytical solution is possible and an approximation has to be made. Equation 3.21 is solved geometrically (Beck 2013). The derived frequencies are estimated according to the following reasoning: The second term on the right-hand side of Equation 3.21 is numerically calculated for a frequency range covering the selected radial orders and n_p at a certain $\Delta\Pi_1$, q and $\Delta\nu$. These frequencies follow a tangent function, when compared to the input frequency. From the geometrical perspective the input and output frequency should be equal, hence giving the frequencies of the mixed modes. This concept is visualised in Figure 3.6, where the tangent functions are given in blue and the frequencies of the mixed modes by red circles.

The grid contains 201 points in the $\Delta\Pi_1$ direction, with a step size of 0.1 s for the RGB stars and 0.2 s for those in the RC, and 101 points along the coupling factor q, with a step size of 0.005, spanning the range 0.01 - 0.51.

Chapter 4

Stellar Modelling of Red Giants

The asymptotic relation for dipole mixed modes is based on empirical observations. In order to test the validity of this description for the mixed modes, stellar evolution models are computed. For these stellar models, the true period spacing $\Delta\Pi_1$ can be deduced from the local properties of the star, allowing to solve the exact definition of $\Delta\Pi_1$, i.e. integrating the Brunt-Väisälä frequency N over the g mode cavity (Equation 1.13).

These stellar models are a theoretical tool for studying stellar structure and evolution. Two different stellar evolution codes were used in this work, namely Aarhus STellar Evolution Code (ASTEC) and GARching Stellar Evolution Code (GARSTEC). GARSTEC was complementarily used to provide reliable stellar evolution models for stars that have passed the He-flash. A direct comparison of the peak bagged frequencies with the theoretical frequencies from the pulsation model allows one to search for the best stellar model. The oscillation package ADIPLS (Section 4.2) was used to compute the oscillation frequencies of the stellar pulsations for RGB stars. Section 4.3 describes the different techniques used to determine the best stellar models, since RC stars were modelled with GARSTEC and no frequencies were computed.

4.1 Stellar Evolution Codes

Stellar evolution codes solve the equations of stellar structure at discrete timesteps for a given set of mesh points in the star, under the conditions governed by the laws of physics describing the hydrostatic equilibrium in the star. In the ideal case, these would be solved in an almost continuous timebase for a full 3D grid with the exact descriptions of the physics. However this is beyond the scope of most theoretical models today. Most stellar evolution codes solve the equations of stellar structure for a one dimensional mesh grid along the radial direction in the interior of the star, using discrete timesteps.

The equations of stellar structure (Equations A.1 - A.5, see Appendix A.1 for more information about the equations of stellar structure and evolution) are solved numerically. This is done for a mesh going from the center of the star to the stellar surface $x_1 < \ldots < x_N$, where the distribution of the mesh points is set up as such that transition regions in the internal structure, e.g. the boundaries of the convection zones, have a denser grid. The solution at timestep t^{s+1} however depends on the solution of the previous timestep t^s. The timestep difference Δt depends on the timescale of variation for most physical parameters. Some parameters, like the time derivatives in the energy equation, always vary with timescales smaller than the this difference, making adequate subsampling necessary.

Convection is always included in the characterisation of the stellar structure, for which the mixing length formalism is the opted description (Vitense 1953; Böhm-Vitense 1958). The mixing length parameter $\alpha_{\rm ML}$ describes the average distance a portion of matter travels before it loses its initial properties, e.g. temperature and composition. It represents a scaling factor of the pressure scale height $\alpha_{\rm ML} H_p$. In order to reduce computational complexity, it is assumed that the mixing, induced by the convective motion, is instantaneous, leading to chemically uniform convective regions. It is often possible to include some levels of overshooting or semiconvection, although this has to be specified by the user.

Different microphysics, and the different descriptions of it, are included in all stellar evolution codes. These comprise the description of the equation of state, the opacity, the nuclear reaction network and their efficiencies, the approximations used for diffusion and settling, the neutrino losses, etc. An overview of the possible treatments of the microphysics can be found in Christensen-Dalsgaard (2008b) for ASTEC and in Weiss & Schlattl (2008) for GARSTEC.

4.1.1 ASTEC

ASTEC is a stellar evolution code mainly developed by Prof. J. Christensen-Dalsgaard at the University of Aarhus (Christensen-Dalsgaard 2008b). Like all stellar evolution codes, it stays under active development to include new treatments of the involved physics. It has been proven to be very successful for the description of the Sun (Christensen-Dalsgaard et al. 1996).

The stars from the sample that were classified as RGB stars from the true period spacing, were modelled by using ASTEC. During the modelling, the NACRE compilation of nuclear reactions (Angulo et al. 1999), the OPAL equations of state and opacities (Iglesias & Rogers 1996) and the solar abundances derived by Grevesse & Noels (1993) were used. No effects of overshooting, microscopic diffusion and mass-loss were considered. Convection was treated according to the mixing length theory, for which α_{ML} was deduced by solar calibration. A simple Eddington relation was used to describe the atmospheric stratification. The stellar evolution was started from the ZAMS and a fixed number of gridpoints (9600) was used to describe the interior of the star.

The stellar models that were developed in this work depend on two input parameters, the photospheric mass of the star M, obtained by the asteroseismic scaling relation (Equation 1.17), and the overall metallicity Z. A stellar model was computed for each (M, Z) considered appropriate for the analysis. Chaplin et al. (2011b) state that the uncertainty on the derived mass from the scaling relation is roughly 10%, which gives an estimate on how large the grid has to be along the mass range. The literature iron abundance [Fe/H] for the red giants (Pinsonneault et al. 2012) defines the average metallicity Z through the approximated relation

$$[\mathrm{Fe/H}] = A \cdot \log_{10}\left[\frac{Z/X}{Z_\odot/X_\odot}\right] , \tag{4.1}$$

where A is a constant in the range 0.9 - 1.0, X the average hydrogen abundance and $Z_\odot$ and $X_\odot$ depict the solar values. Since the values stated in Table 2.1 are either solar or slightly more metal-rich compared to the Sun, every stellar evolution model was built for $Z = 0.02$ and $Z = 0.03$. The models evolve from the ZAMS up to a region where they should almost reach the tip of the RGB phase, which corresponds to roughly 2000 timesteps. An example of the evolution of a stellar model of $M = 1.45\ M_\odot$ and $Z = 0.02$ through the H-R diagram from the ZAMS up to the RGB is given in the left panel of Figure 4.1.

4.1.2 GARSTEC

The RC stars are modelled with GARSTEC. It has been developed through many decades at the Max-Planck-Institute of Garching and offers a large variety of input physics for stellar modelling (Weiss & Schlattl 2008).

For the stellar modelling of the RC stars the 2005 revised OPAL opacities (Iglesias & Rogers 1996; Ferguson et al. 2005) and the equations of state (Rogers & Nayfonov 2002; Hummer & Mihalas 1988) were used for the revised solar abundances (Serenelli et al. 2009). Diffusive mixing takes place in the convective regions instead of instantaneous mixing, where the effective diffusion constant is deduced from the convective velocity.

The stellar evolution models start from the pre-main sequence and are left to evolve up to the tip of the RGB, then through the helium flash until the end of the central helium burning phase. The modelling was terminated at the end of the RC phase, when all the central helium has been fused into carbon and oxygen. Once again, the mass determined from the asteroseismic scaling relation acts as a starting point to build models. The overall metallicity Z and the mass of the star are used as the input parameters to build the models. An example of the evolution through the H-R diagram is given in Figure 4.1 (right panel) for a stellar model with $M = 1.45\ M_\odot$ and $Z = 0.02$ starting in the pre-MS phase until the star leaves the RC phase.

4.2 Stellar Pulsation Code: ADIPLS

In addition, it is possible to use a stellar pulsation code for deriving information about the pulsations occurring in a star described by a given stellar model. ADIPLS is such a pulsation code and it computes the frequencies and eigenfunctions of adiabatic oscillations for general stellar models (Christensen-Dalsgaard 2008a). The properties of the pulsation can be deduced under the adiabatic approximation, where the heating term in the energy equation (Equation A.4) is neglected. This makes the computations much easier while a high degree of precision is still achieved (Aerts et al. 2010).

Stellar oscillations can be theoretically described as a perturbation of the equilibrium structure, defined by the equations of stellar structure and evolution. This perturbation is accompanied by a displacement $\delta\mathbf{r}$ described in spherical coordinates (r, θ, ϕ).

The equations describing the perturbation are given in Appendix A.2, likewise the solving mechanism adopted. The stellar pulsation code calculates, for modes with a given spherical degree ℓ, the frequencies ν, the radial order n and the normalized mode inertia $\hat{E}$.

Since the radius is not a direct input parameter for the stellar evolution modelling of an RGB star with ASTEC, the radii were obtained for each timestep. The timestep t_{scaling} was obtained by matching the photospheric radius of the model to the value derived from the asteroseismic scaling relation (Equation 1.16). This timestep was then used to build

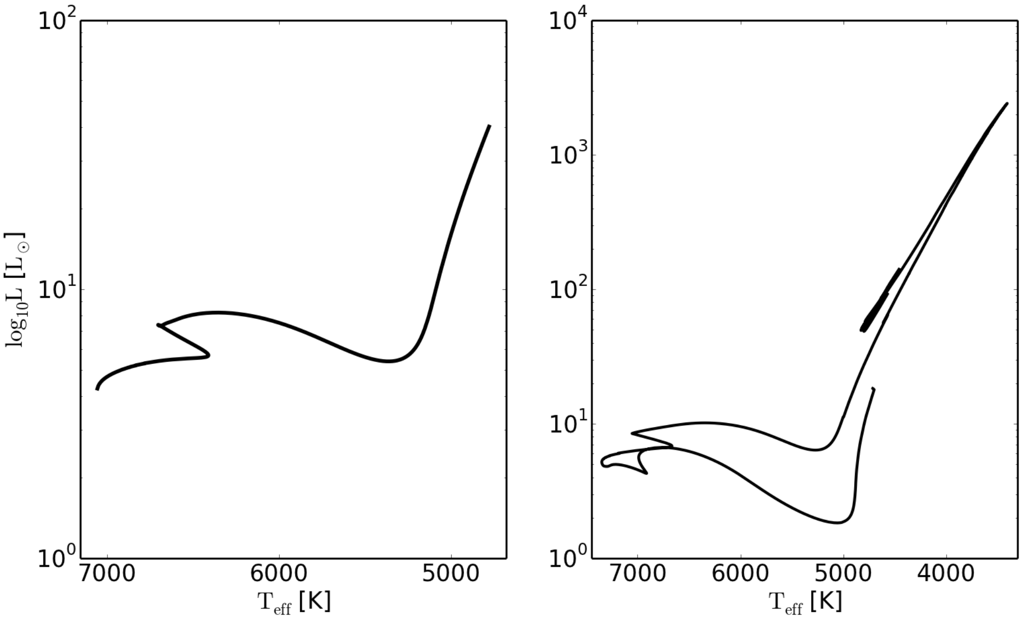

Figure 4.1: *Left:* The evolution of a stellar model computed with ASTEC with $M = 1.45\ M_\odot$ and $Z = 0.02$ through the H-R diagram from the ZAMS up to high in the RGB phase. *Right:* The evolution of a stellar model computed with GARSTEC having $M = 1.45\ M_\odot$ and $Z = 0.02$ through the H-R diagram from the pre-MS phase until the end of the helium-core burning phase.

the radius axis and expand the 2D grid of stellar models to a 3D grid (M, Z, R), for which stellar pulsations were calculated. ADIPLS was used to model frequencies for the range $t_{\rm scaling} - 100$ steps to $t_{\rm scaling} + 100$ steps. The deduced frequencies of the models were then subsequently compared to the frequencies measured from the PSD. The comparisons adopted, to obtain the best stellar model, is presented in the following section.

4.3 Model Comparison to Measurements

The modelling of both RC and RGB stars was not performed in the same way, therefore different techniques had to be employed in order to find the most adequate stellar model. For the RGB stars, the resulting frequencies from ADIPLS are compared with the frequencies measured by means of the peak bagging analysis. Since no frequencies are produced for the models of the RC stars, the comparison with the deduced values from the pipeline is made by using $\nu_{\rm max}$, $\Delta\nu$ and the true period spacing derived from the Brunt-Väisälä frequency.

4.3.1 RGB: ASTEC & ADIPLS

The modelled frequencies derived for each stellar model in the (R, M, Z) grid were compared to the frequencies extracted from the PSD of the corresponding RGB star. The model produces many more frequencies than those measured during the mode extraction from the PSD. Therefore only the region around the deduced ν_{max} was considered, using the same amount of radial orders as used for the mode extraction. For each model, the chi-squared χ^2_{ASTEC} was calculated as

$$\chi^2_{\mathrm{ASTEC}} = \frac{1}{N_0 + N_1 + N_2 - 2} \sum_{\ell=0,1,2} \left[\sum_{j}^{N_\ell} \left(\frac{\theta_{\ell,j,\mathrm{obs}} - \theta_{\ell,j,\mathrm{theo}}}{\sigma(\theta_{\ell,j,\mathrm{obs}})} \right)^2 \right] , \tag{4.2}$$

where ℓ is the spherical degree of the mode and N_ℓ is the number of frequencies measured for that degree. $\theta_{\ell,j,\mathrm{obs}}$ is the phase shift of the j-th extracted mode of spherical degree ℓ (as defined by Equation 3.15), $\sigma(\theta_{\ell,j,\mathrm{obs}})$ is the corresponding uncertainty on the measured frequency (as propagated by Equation 3.19) and $\theta_{\ell,j,\mathrm{theo}}$ is the phase shift of the modelled mode closest to the observed mode. The -2 term in the normalisation of the χ^2_{ASTEC} is introduced for two reasons. First, it includes the fact that it is an observed data sample and, second, because there is one fitting parameter, namely the frequency.

The theoretical frequencies, used in the calculation of the chi-squared χ^2_{ASTEC}, have to be corrected for the near-surface term ϵ. Therefore the phase shifts θ (Equation 3.15) are used, since these are independent of ϵ. Other possibilities like the description of Kjeldsen et al. (2008), where a power law was used to correct for the effects of the surface term on the frequency ν, were implemented to verify the most likely pulsation model simultaneously with the description of θ. This allowed to retrieve possible systematics in the model comparison.

Once a best model is obtained according to the evaluation of Equation 4.2, the true period spacing $\Delta\Pi_1$ estimated from the data is compared to the value of the model. $\Delta\Pi_1$ of the stellar models can be derived by means of different methods. First, it can be deduced from the exact definition for the true period spacing, e.g. the integral over the Brunt-Väisälä frequency N of the g mode cavity (Equation 1.13). This is straight forward since the Brunt-Väisälä frequency is calculated for every pulsation model. Similarly to the analysis done for the data, $\Delta\Pi_1$ can be inferred from the fit to the observed period spacing ΔP for all consecutive dipole mixed modes. Since the model provides all possible frequencies for the $\ell = 1$ modes and because there are no missing frequencies, the fitting is much more stable. An example of ΔP for the dipole mixed modes, obtained for a model with $M = 1.45$ $\mathrm{M}_\odot$, $Z = 0.02$ and $R = 6.50$ $\mathrm{R}_\odot$, is given in Figure 4.2.

Although both methods provide a value for $\Delta\Pi_1$, only the value obtained by the first method, the integral of N, is used in the comparison with the deduced values for the sample of red giants. The second method is instead adopted as a consistency check.

4.3.2 RC: GARSTEC

Pulsation codes do not always provide realistic sets of frequencies for stellar models in the RC phase, therefore a different approach was used for these stars. Instead of comparing modelled frequencies with observed frequencies, a comparison between three asteroseismic parameters was made, namely frequency of maximum oscillation power ν_{max}, the large frequency separation $\Delta\nu$ and the true period spacing $\Delta\Pi_1$. Both ν_{max} and $\Delta\nu$ were obtained through the asteroseismic scaling relations (Equations 1.14 and 1.15), while $\Delta\Pi_1$ was inferred from Equation 1.13. The comparison between the stellar model and the

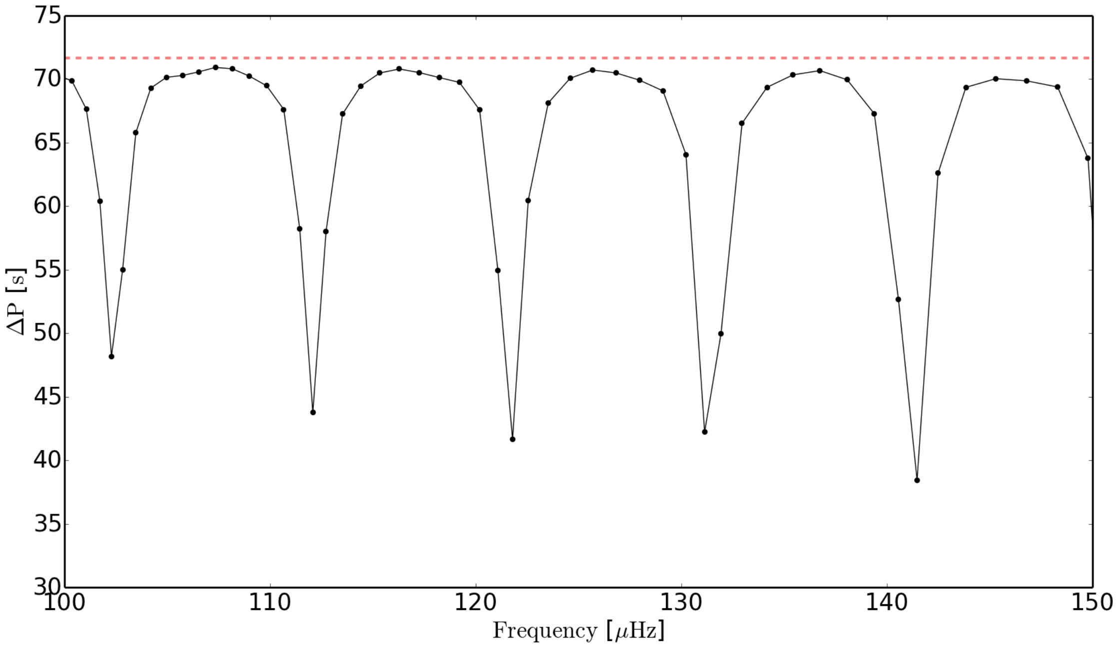

Figure 4.2: The observed period spacing ΔP from the frequencies derived for a stellar model with $M = 1.45$ $\mathrm{M}_\odot$, $Z = 0.02$ and $R = 6.50$ $\mathrm{R}_\odot$. By fitting ΔP with the method described in Section 3.4, a consistency-check was performed with the derived $\Delta\Pi_1$(red dashed line) using the integral of the Brunt-Väisälä frequency (Equation 1.13).

observation was done by using a chi-squared test, where equal weights were given to each parameter, and defined as

$$\chi^2_{\mathrm{GARSTEC}} = \left(\frac{\nu_{\mathrm{max,obs}} - \nu_{\mathrm{max,model}}}{\sigma(\nu_{\mathrm{max,obs}})}\right)^2 + \left(\frac{\Delta\nu_{\mathrm{obs}} - \Delta\nu_{\mathrm{model}}}{\sigma(\Delta\nu_{\mathrm{obs}})}\right)^2 + \left(\frac{\Delta\Pi_{1,\mathrm{obs}} - \Delta\Pi_{1,\mathrm{model}}}{\sigma(\Delta\Pi_{1,\mathrm{obs}})}\right)^2 . \tag{4.3}$$

The subscript *obs* indicates the result from the mode extraction or determination of the PSD, while the subscript *model* corresponds to the values obtained from the stellar model. $\sigma(\nu_{\mathrm{max,obs}})$, $\sigma(\Delta\nu_{\mathrm{obs}})$ and $\sigma(\Delta\Pi_{1,\mathrm{obs}})$ are the uncertainties on the observed ν_{max}, $\Delta\nu$ and $\Delta\Pi_1$, respectively.

Chapter 5

Results for the Sample of Red Giants and Discussion

The three red giants selected in this work, together with the synthetic star Ziva, were analysed according to the seismic data analysis pipeline presented in Chapter 3. Once a reliable set of pulsation modes has been identified through mode extraction, a comparison by means of stellar evolution and pulsation models is made. In this chapter all the results obtained are presented and discussed.

The asteroseismic parameters $\nu_{\rm max}$ and $\Delta\nu$ estimated in this work through different methods are described in Section 5.1. The pipeline settings adopted for the mode extraction for each star are presented in Section 5.2. The true period spacings, both obtained by fitting ΔP and by using the asymptotic relation, are presented in Section 5.3, for the extracted frequencies of the dipole modes. Stellar models were built for each star by using the information of the mode extraction and the stellar evolution code is chosen according the value for the true period spacing $\Delta\Pi_1$. The specifics regarding the modelling are presented in Section 5.4.

The figures for the analysis of KIC 6928997 are presented the following sections, while those related to the other stars can be found in the Appendices.

5.1 Determination of the Asteroseismic Parameters $\Delta\nu$ and $\nu_{\rm max}$

The first step in the analysis of the red giants is the determination of global asteroseismic parameters for each star. These include the frequency of maximum oscillation power $\nu_{\rm max}$ and the large frequency separation $\Delta\nu$.

The values for the frequency of maximum oscillation power $\nu_{\rm max}$ determined according to the two methods described in Section 3.1, are listed in Table 5.1 for all the stars of the sample. One example for the model of the background of the PSD is presented in Figure 5.1 for KIC 6928997 and in Appendix B.1 for the other three stars. The initial fit from the LS method is given in red, while the best description of the MCMC is indicated by the solid yellow line.

The uncertainties for $\nu_{\rm max}$, determined with the MCMC, correspond to a 1σ uncertainty, deduced from the marginal distribution. Since the distribution is not perfectly Gaussian, both upper and lower uncertainty are stated instead of the standard deviation.

Table 5.1: The frequencies of maximum oscillation power $\nu_{\rm max}$ for all stars in the sample, as derived according to the different methods adopted. The values for $\nu_{\rm max}$ are compared to the value obtained by applying the asteroseismic scaling relation (Equation 1.14) for the radius, mass and $T_{\rm eff}$ of the best fitting model (see Table 5.6).

	$\nu_{\rm max}$ LS (μHz)	$\nu_{\rm max}$ MCMC (μHz)	$\nu_{\rm max}$ Model (μHz)
KIC 6928997	120.11	$121.24^{+0.28}_{-0.32}$	126.63
KIC 6762022	39.63	$40.97^{+0.22}_{-0.27}$	40.99
KIC 10593078	206.44	$207.19^{+0.49}_{-0.47}$	216.04
Ziva	114.52	116.83 ± 0.13	103.40

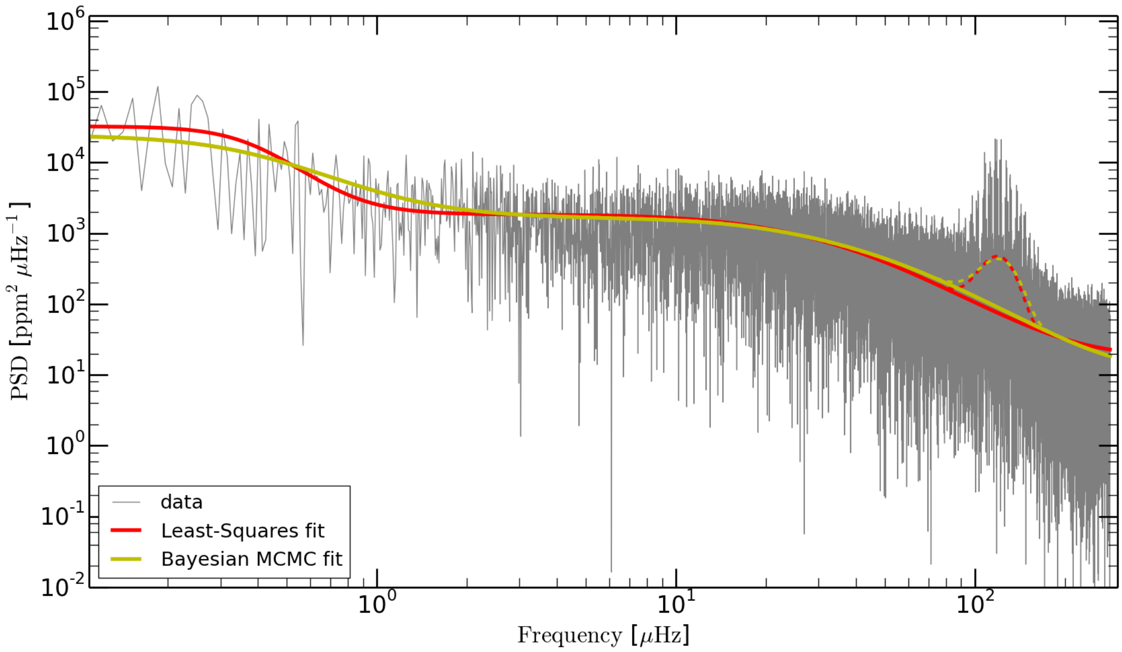

Figure 5.1: The resulting background fit using the Bayesian approach (solid yellow line) to the PSD (gray) of KIC 6928997. The initial estimation using the LS minimisation is given by the red solid line. The yellow (red) dashed line represent the model of the background together with the Gaussian power excess.

The upper (lower) uncertainty are deduced from the difference between the 84% (16%) percentile and the median value in the marginal distribution.

The second global asteroseismic parameter deduced, before any mode extraction, is the large frequency separation $\Delta\nu$, computed from the fitting process of the ACF (Section 3.2). The values derived for $\Delta\nu$, for both methods, are listed in Table 5.2 for all the stars selected.

The determination of $\Delta\nu$ from the ACF in the case of KIC 6928997 is presented in Figure 5.2. The green line indicates the estimated $\Delta\nu$ from the scaling relation with $\nu_{\max}$ (Equation 3.5). The obtained $\Delta\nu$ from the LS fit (indicated in red) is given by the black vertical line. The figures for the other three stars in the sample are given in Appendix B.2.

5.2 Mode Extraction

Once the global asteroseismic parameters of each star are characterised, the significant modes are extracted. The pipeline presented in Section 3.3, is used to detect the significant mode peaks in the PSD and to fit the modes with a Lorentzian profile.

The peak bagging method depends on several parameters which can be fine-tuned. The first parameter is the frequency of the central radial mode $\nu_{\ell=0,\mathrm{central}}$. This is perhaps the most important parameter, together with $\Delta\nu$, because it is used to scale down to different radial orders. This value is estimated from a frequency échelle, constructed with all values of the PSD passing the SNR criterion and for five radial orders centered on $\nu_{\max}$. The distinct pattern of the small frequency separation $\delta\nu_{02}$ is searched in the frequency échelle and the frequency of the radial mode closest to $\nu_{\max}$ is taken as $\nu_{\ell=0,\mathrm{central}}$. There is a tolerance on the input $\nu_{\ell=0,\mathrm{central}}$ up to 5% of $\Delta\nu$, since the pipeline improves this frequency before it starts the mode extraction. Another parameter defines the SNR threshold as a multiple of the average SNR for each radial order. For consistency during the analysis, process, the threshold has been set to a value of 7 since it allows to take the most likely peaks without being too strict in the selection. The threshold parameter also influences the number of radial orders that are included during the mode extraction. Five significant radial orders are considered as a starting point, centered around $\nu_{\ell=0,\mathrm{central}}$. When no significant modes are identified in the outer most radial orders, these are excluded from the analysis, reducing the number of considered radial orders to 3. The final parameter needed to describe the peak bagging is the desired resolution Res, a minimum frequency interval aimed at discriminating between consecutive frequency peaks. Res has been chosen as a function of the deduced $\nu_{\max}$, where a value of 0.2 μHz is adopted for stars with $\nu_{\max} > 100$ μHz, otherwise $Res = 0.1$ μHz is used.

Once all significant modes have been extracted and fitted with a Lorentzian profile, the Bayesian MCMC is used to deduce the final parameters for each oscillation mode. The MCMC runs independently for each radial order.

The values used for the input parameters of the mode extraction pipeline are presented in Table 5.3. For every star, except KIC 6762022, five significant radial orders are considered during the peak bagging. It is possible to use more significant radial orders, up to a total of seven for the artificial PSD of Ziva. However to follow the same analysis as the other targets, only five radial orders have been considered. The increased number of significant radial orders for Ziva is related to the absence of the granulation terms in

Table 5.2: The values of $\Delta\nu$ derived for the sample of stars. The probe is deduced from the scaling relation with $\nu_{\max}$ (Equation 3.5). The deduced values for $\Delta\nu$ are compared to the value determined for the best stellar model by applying the asteroseismic scaling relation (Equation 1.15).

	$\Delta\nu$ Probe (μHz)	$\Delta\nu$ ACF (μHz)	$\Delta\nu$ MCMC (μHz)	$\Delta\nu$ Model (μHz)
KIC 6928997	10.60	10.025	10.038 ± 0.009	10.295
KIC 6762022	4.50	4.464	4.455 ± 0.011	4.401
KIC 10593078	16.11	15.304	$15.459^{+0.022}_{-0.019}$	15.701
Ziva	10.22	8.967	$8.947^{+0.034}_{-0.039}$	8.927

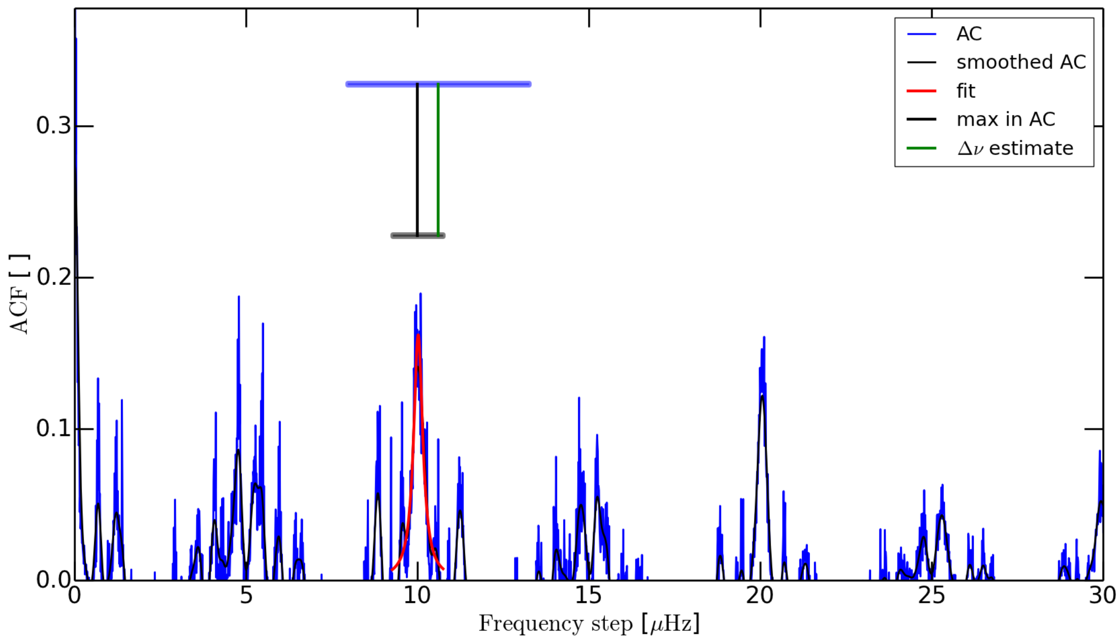

Figure 5.2: The determination of $\Delta\nu$ for KIC 6928997, where the ACF is given in solid blue. The green line represents the estimate for $\Delta\nu$, obtained from Equation 3.5. The maximum in the ACF shaded blue region (i.e. the search interval) is fitted by a Lorentzian profile (red line) to determine $\Delta\nu$. The deduced large frequency spacing is given by the black line.

Table 5.3: The input parameter for the pipeline and the number of frequencies obtained in the asteroseismic analysis. The frequency of the central radial mode $\nu_{\ell=0,\mathrm{central}}$, the number of radial orders # orders and the SNR threshold of an integer (MoN) times the average SNR are indicated. The total number of significant peaks $\#\nu_\ell$ and the number of dipole modes $\#\nu_{\ell=1}$ are also given.

	$\nu_{\ell=0,\mathrm{central}}$ (μHz)	# orders	MoN	Res	$\#\nu_\ell$	$\#\nu_{\ell=1}$
KIC 6928997	122.5	5	7	0.2	29	18
KIC 6762022	39.5	3	7	0.1	21	15
KIC 10593078	204.5	5	7	0.2	26	16
Ziva	114.5	5	7	0.2	39	28

the simulated PSD, used to determine the SNR. The number of significant modes for each star and the number of dipole mixed modes obtained are also indicated in Table 5.3. These dipole mixed modes, using the frequency, amplitude and FWHM deduced by the Bayesian MCMC, are used in the description of the true period spacing $\Delta\Pi_1$.

The result for the mode extraction for KIC 6928997 is presented in Figure 5.3. The magenta line represents the fit with the different Lorentzian components for each radial order. The different colour coding represents the various spherical degrees of the modes. The fits for the other three stars in the sample are presented in Appendix E.

5.3 Determination of the True Period Spacing $\Delta\Pi_1$

From the set of dipole mixed modes, obtained during the mode extraction for each red giant, the true period spacing $\Delta\Pi_1$ is determined, according to the two adopted methods described in Section 3.4. The resulting values for $\Delta\Pi_1$, and the coupling factor q for the asymptotic relation, are presented in Table 5.4.

The fit to ΔP for KIC 6928997 to determine $\Delta\Pi_1$ is presented in Figure 5.4. The fit is indicated by the solid black line, whereas the measured period spacings for the dipole mixed modes are indicated by the black squares. Figures presenting the same approach for the other red giants are presented in Appendix C.

The gridsearch method (Section 3.4.2) is applied to derive the best values for $\Delta\Pi_1$ and q for the asymptotic relation (Equation 3.21). A large range of values around the value for $\Delta\Pi_1$obtained by the fit to the observed ΔP, and q, is searched for possible solutions. The χ^2_{grid} is calculated for each $(\Delta\Pi_1, q)$ pair in the grid. The result is depicted as the correlation map in Figure 5.5. The color reflects the χ^2_{grid} derived from the fit and the best pair of values for $\Delta\Pi_1$ and q is indicated with a dot. The correlation map reveals the presence of many local minima in the form of ridges. In order to study the structure of the local minima in more detail, cross-cuts in each direction through the coordinates of the minimum chi-square, marked by the circle, are produced. The cross-cuts for KIC 6928997 are shown in Figure 5.6 (Figure D.4, D.5 and D.6 for the other stars in our sample). The cut along q indicates that q is not well constrained, leading to the elongated ridges along the x-axis in Figure 5.5. Cutting through $\Delta\Pi_1$ shows that numerous local minima close

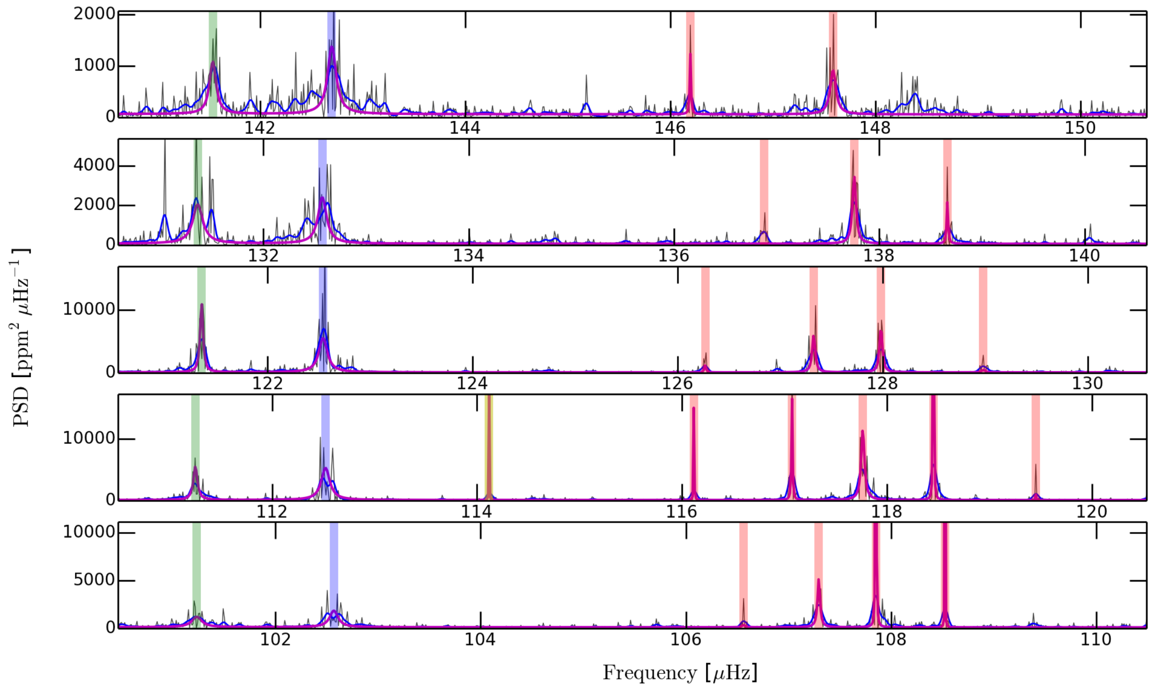

Figure 5.3: The radial, dipole, quadrupole and octupole modes retrieved by peak bagging for KIC 6928997 are respectively indicated by the blue, red, green and yellow shaded region in the PSD. The PSD itself is given in black, the smoothed PSD with a moving boxcar of 0.1 μHz in blue and the fit in magenta.

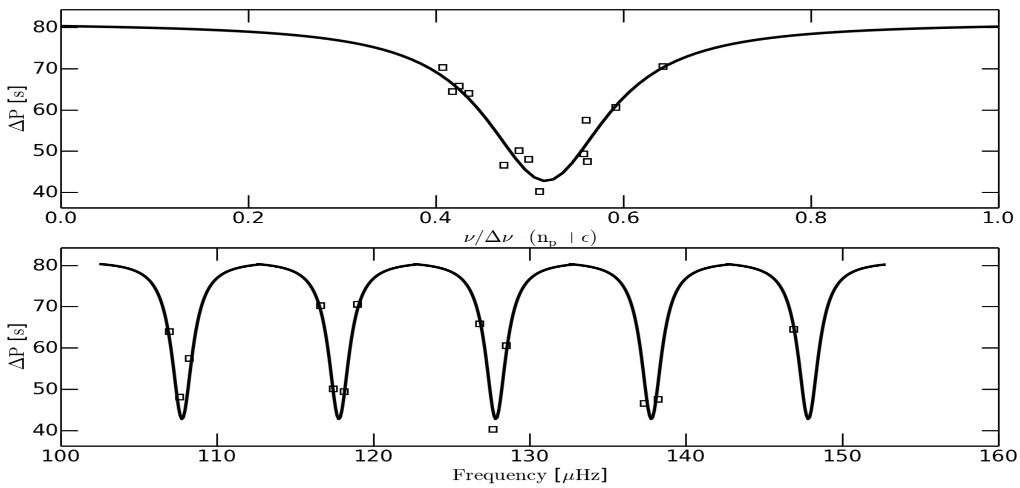

Figure 5.4: Deducing $\Delta\Pi_1$ for KIC 6928997 using the empirical approach of fitting ΔP yielded $\Delta\Pi_1 = 81.14$ s. The fit is done for the phase shift θ (*top*) and subsequently expanded to ν (*bottom*), using the inverse relation of Equation 3.15

.

Table 5.4: The values for the true period spacing $\Delta\Pi_1$. These are obtained from the fit to the observed ΔP and the use of the asymptotic relation (Equation 3.21). The $\chi^2_{\rm grid}$ level of the optimal asymptotic solution and the 1σ uncertainty are indicated. The value of $\Delta\Pi_1$ stated for the models is deduced by calculating the integral of the Brunt-Väisälä frequency (Equation 1.13).

	$\Delta\Pi_1$ ΔP fit (s)	$\Delta\Pi_1$ Asymptotic (s)	q Asymptotic	$\Delta\Pi_1$ model (s)	$\chi^2_{\rm grid}$ min	$\chi^2_{\rm grid}$ 1σ
KIC 6928997	81.14 ± 2.55	77.2 ± 0.7	$0.105^{+0.180}_{-0.090}$	72.94	29.76	298
KIC 6762022	249.00 ± 19.65	258.6 ± 2.8	$0.240^{+0.220}_{-0.121}$	258.2	0.867	5.286
KIC 10593078	88.11 ± 1.41	82.1 ± 1.4	$0.155^{+0.185}_{-0.117}$	81.83	606	2645
Ziva	70.89 ± 0.74	69.8 ± 0.6	$0.090^{+0.250}_{-0.070}$	70.35	101.37	420

to the best solution are nearly as deep as the prime minimum for the best solution. This best solution obtained by the gridsearch method is indicated by the blue dashed line.

The determination of the uncertainties on both $\Delta\Pi_1$ and q, appears to be challenging. This is caused by the presence of several local minima in the grid with varying $\Delta\Pi_1$. The difference in $\Delta\Pi_1$ from the optimal solution to the closest minima in the chi-squared distribution for the $\Delta\Pi_1$ ridges is used as an indication for the 1σ uncertainty. The uncertainty derived in this way sets the order of magnitude on the precision level made possible with the method. The $\chi^2_{\rm grid}$ level corresponding to uncertainty interval identified for $\Delta\Pi_1$ is then used for determining the uncertainty on the coupling factor q. The figures visualising this method are given in Appendix D (Figure 5.6 for KIC 6928997) and the $\chi^2_{\rm grid}$ corresponding to the 1σ uncertainty is given in Table 5.4.

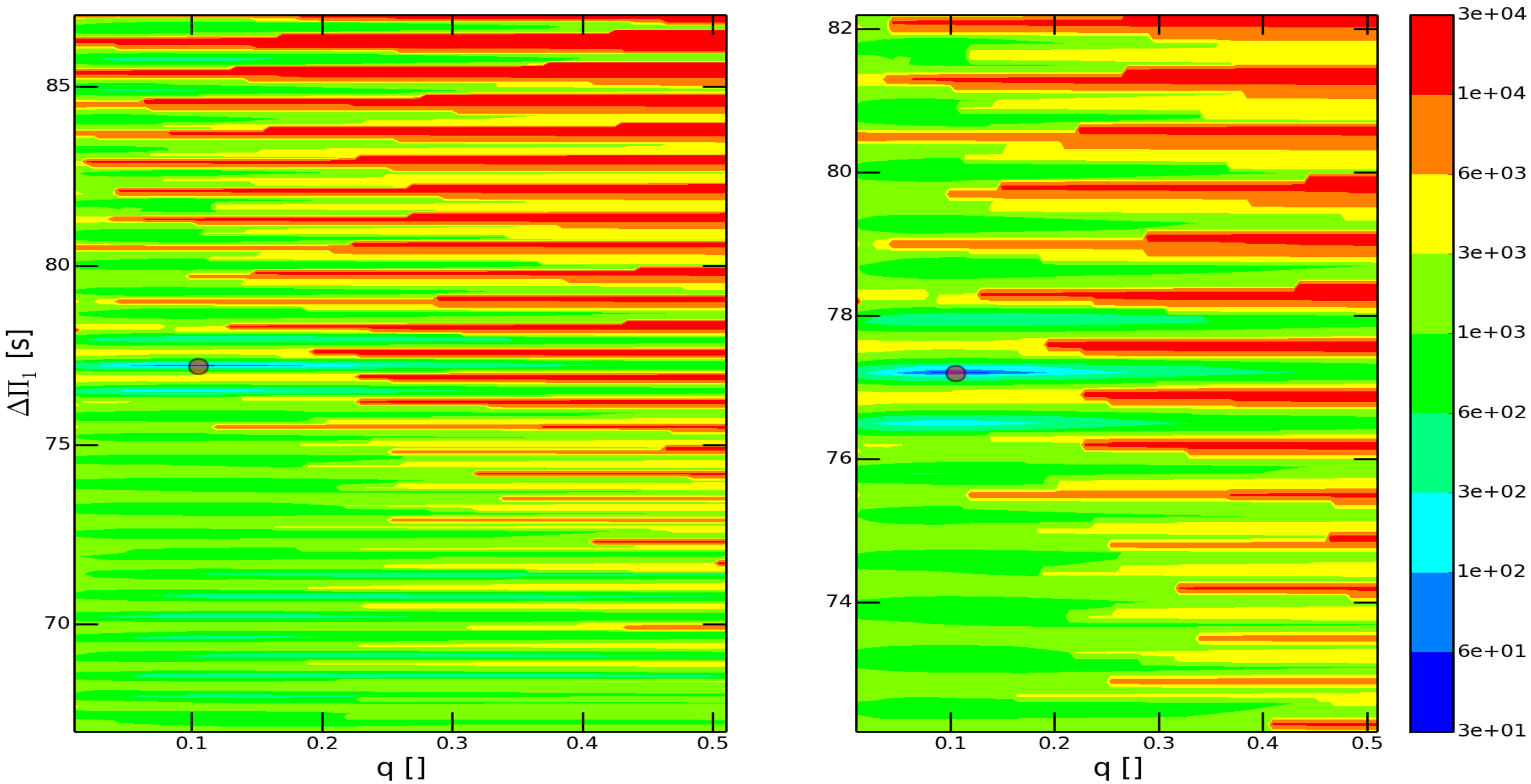

Figure 5.5: *Left:* The results from the gridsearch to determine $(\Delta\Pi_1, q)$ using the asymptotic relation for KIC 6928997. The grid is composed of 201 meshpoints along the $\Delta\Pi_1$ axis and 101 along the q axis. The color scale indicates the χ^2_{grid} derived from the grid search. The best solution for the pair of $(\Delta\Pi_1, q)$ is indicated by a dot. *Right:* A zoom of the region with the optimal solution.

The most likely pair of values for $\Delta\Pi_1$ and q deduced with the gridsearch for the asymptotic relation for each star are visually inspected in both frequency and period échelle diagrams (Figure 5.7 for KIC 6928997, Appendix D otherwise). The frequency échelle visualises the correspondence between the extracted dipole frequencies and the frequencies from the asymptotic relation, while the period échelle visualises the correspondence between $\Delta\Pi_1$ and q. The slope of the rises in the period échelle depends on q, where a smaller value for q gives a steeper slope.

5.4 Determination of the Best Stellar Model

Stellar evolution models are built for each star, either with ASTEC if the star is along the RGB or with GARSTEC if it is a RC star. The information from the mode extraction and the literature lead to a grid of stellar evolution models, as presented in Table 5.5.

For stars classified as an RGB star, the appropriate timestep in the stellar evolution model needs to be obtained to deduce the pulsation models. This is done by matching the radius of the star in the model with the observed value inferred from the scaling relations. When the star is observed to be in the RC phase, the stellar evolution models are built in such a way that they stop the evolution just before the RC phase, using a central helium abundance $Y_c = 0.9$ as stopping criterion. The evolution is then continued until the core runs out of helium, i.e. $Y_c = 0.0$. During this last part of the stellar evolution, a *fgong* file is produced for each timestep, saving important local and global stellar properties.

The built stellar models and the modelled stellar pulations spectra, are compared to the observations as described in Section 4.3, obtaining the most likely stellar models. The characteristics of these stellar models are given in Table 5.6 in comparison with the values deduced from the observations and the literature (Table 2.1). The effective temperature and metallicity of the artificial star Ziva are provided together with the PSD, allowing to solve the scaling relations. The deduced $\nu_{\max}$, $\Delta\nu$ and $\Delta\Pi_1$ for the most likely model are presented in Table 5.1, 5.2 and 5.2, respectively.

5.4.1 Ziva

The artificial PSD of Ziva caused additional difficulties during the determination of the most likely model. In fact, when the original set of ADIPLS models built for Ziva are

Table 5.5: Specifics about the grid of stellar models. The mass and metallicity range are given, and the method adopted to fix the radius range. Indexes corresponding to the scaled radius of observations are used for ASTEC models, while all timesteps in the RC phase are taken for GARSTEC models.

	Mass range ($M_\odot$)	Z range	Radius range	# models
KIC 6928997	1.40 – 1.48	0.02 – 0.03	indexes	3466
KIC 6762022	1.40 – 1.50	fixed	RC	10505
KIC 10593078	1.35 – 1.44	0.02 – 0.03	indexes	4030
Ziva	1.85 – 2.05	fixed	indexes	1071

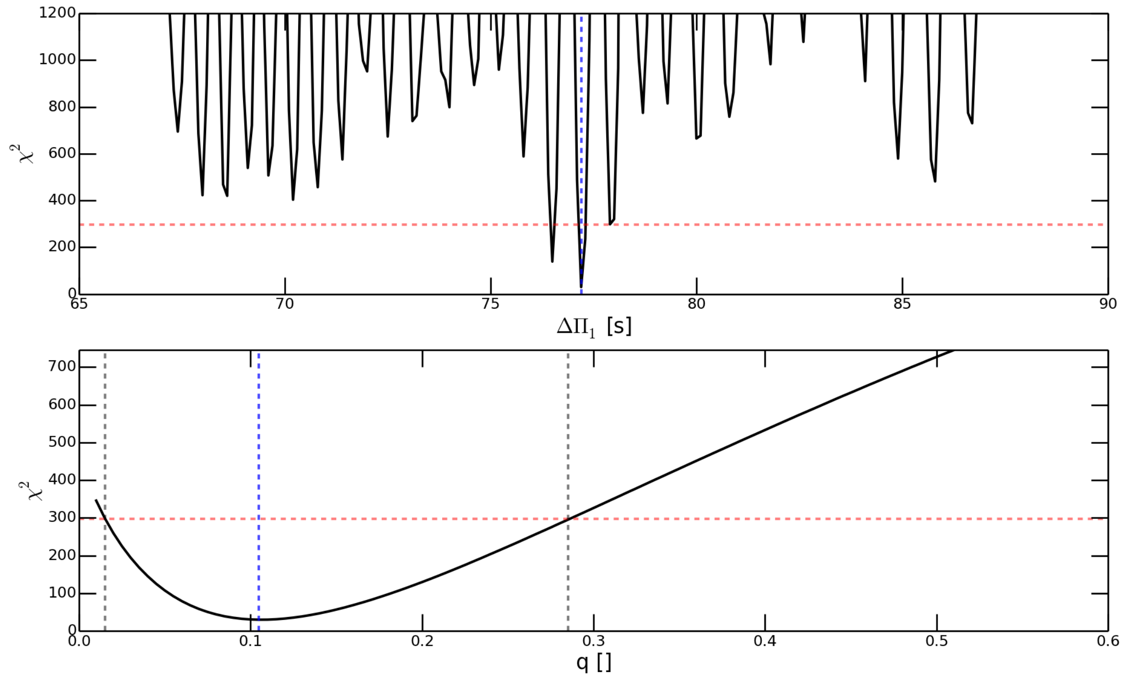

Figure 5.6: The cross-cut in the grid along fixed q ($\Delta\Pi_1$) of the optimal solution (blue dashed line) for varying $\Delta\Pi_1$ (q) in the grid is indicated by the black line in the *top* (*bottom*) panel for KIC 6928997. The χ^2_{grid} level, corresponding to a 1σ uncertainty is given by the red dashed line. The upper (lower) boundaries for the uncertainty on q are given by the gray dashed lines.

Table 5.6: The deduced radius and mass from the scaling relations (Equations 1.16 and 1.17) for the parameters estimated from the analysis of the PSD are compared to the most likely models. The parameters from the best stellar evolution model are also indicated.

	M scaling ($M_\odot$)	R scaling ($R_\odot$)	M model ($M_\odot$)	R model ($R_\odot$)	Z model dex	T_{eff} model (K)	χ^2_{model} model
KIC 6928997	1.45 ± 0.09	6.40 ± 0.64	1.46	6.31	0.03	4822	452
KIC 6762022	1.45 ± 0.09	11.00 ± 1.0	1.47	11.13	0.02	4789	$2.85 \cdot 10^{-3}$
KIC 10593078	1.40 ± 0.08	4.78 ± 0.48	1.37	4.66	0.03	4893	517
Ziva	1.95 ± 0.12	7.62 ± 0.76	1.44	6.90	0.02	4899	582

compared with the observed frequencies, the most likely model had $M = 1.86\ M_\odot$, $R = 7.55\ R_\odot$ and $Z = 0.02$. However, when this comparison is visualised in a frequency échelle, the result is not satisfying. The frequency list of Ziva has been compared with all existing ADIPLS models. This provides a new, most likely stellar model with $M = 1.44\ M_\odot$, $R = 6.90\ R_\odot$ and $Z = 0.02$. The differences in the frequency échelle diagram are shown in Figure 5.8, where the improvement for the dipole mixed modes is clear. This is reflected by a decrease in normalised chi-squared from $\chi^2_{\text{ASTEC}} = 5540$ for the model with $M = 1.86\ M_\odot$ to $\chi^2_{\text{ASTEC}} = 582$ for the model with $M = 1.44\ M_\odot$.

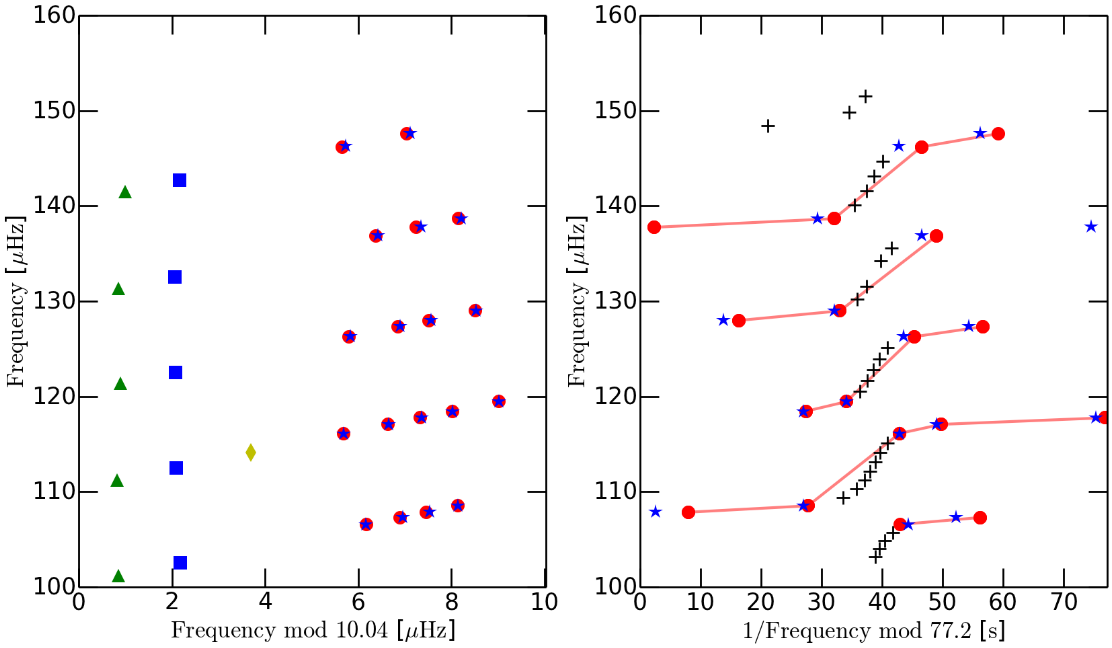

Figure 5.7: *Left:* A frequency échelle, comparing the obtained frequencies of the dipole mixed modes for the most likely description using the asymptotic relation with $\Delta\Pi_1 = 77.2$ s and $q = 0.105$ to the extracted modes from the PSD for KIC 6928997. The extracted radial, dipole, quadrupole and octupole modes are indicated by blue squares, red dots, green triangles and yellow diamonds, respectively. The frequencies of the dipole mixed modes, obtained from the asymptotic relation, and which are used in the comparison are indicated by blue stars. *Right:* A period échelle, showing the same comparison as in the left panel with the same colour coding. The black '+' indicate the frequencies for the mixed modes, obtained from the asymptotic relation, which are not used in the comparison.

5.5 Discussion of the Results

A comparison of the results derived in this work with those existing in the literature is presented in this section. In addition, general remarks and a discussion about the different analysis methods exposed in the previous chapters are also provided.

The asteroseismic parameters $\nu_{\max}$ and $\Delta\nu$ are discussed in Section 5.5.1, and the results for the true period spacing $\Delta\Pi_1$ are reviewed in Section 5.5.2. The description of the asymptotic relation for each star is compared with the extracted modes of the PSD and the most likely stellar model in Section 5.5.3.

5.5.1 The Asteroseismic Parameters $\nu_{\max}$ and $\Delta\nu$

The background models are matched to the PSD according to the two adopted fitting techniques, i.e. a LS minimisation and a Bayesian MCMC. Both techniques provide a reliable set of parameters for the description of the background (Equation 3.3), which is clear from the visual inspection of Figure 5.1 and the figures presented in Appendix B.1. However, the model using the median values of the marginal distribution deduced

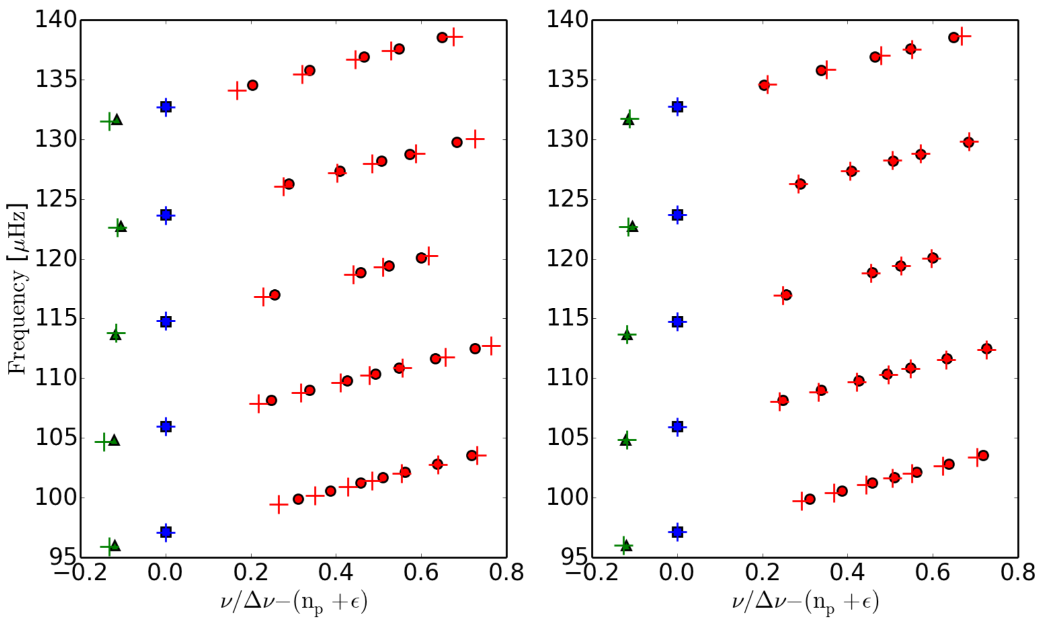

Figure 5.8: Frequency échelle diagrams for Ziva to have a visual comparison between the observation and most likely model. *Left:* The comparison with the stellar model with $M = 1.86$ M$_\odot$, $R = 7.55$ R$_\odot$ and $Z = 0.02$. The observed radial, dipole and quadrupole modes are indicated by blue squares, red dots and green triangles respectively. The deduced frequencies for the model are given by crosses, using the same color coding as the observed frequencies. *Right:* For the stellar model with $M = 1.44$ M$_\odot$, $R = 6.90$ R$_\odot$ and $Z = 0.02$.

by means of the Bayesian MCMC provide a better match to the background in the region of the power excess. Therefore, the values obtained with the MCMC approach are chosen over the values determined with the LS fitting method. It is also noted that the fit using the MCMC method provides a slightly worse description in the low frequency regime ($\nu < 2$ μHz). This is caused by a change in the slope for the granulation component describing this region. The slope decreases from an average value of 4 for the LS fit to a value in the interval 2 - 3 for the Bayesian approach. Recently, Kallinger et al. (2014) found that a slope of 4 is the most suitable value for red giants, therefore the fitting procedure will be repeated in the future with a fixed slope of 4.

The deduced values for ν_{max} with the LS minimisation agree rather well with the value determined according to the Bayesian approach (Table 5.1). However, the former still remain outside the 1σ uncertainty obtained from the marginal distribution for ν_{max} with the MCMC. The uncertainty derived with the Bayesian method is on average 0.4%, while the average difference between the values derived by the two methods is 1.9%. Similar to the background model, the value obtained with the Bayesian MCMC is adopted as the final value for the frequency of maximum oscillation power.

The measured ν_{max} and those inferred from the scaling relations for the stellar model for the red giants (Table 5.1) are in rather good agreement[1], with an average difference of

[1]The discussion regarding the match between the stellar model and the modes extracted for each RGB

3%. The differences are likely to be related to the empirical nature of the scaling relation, which represents only an approximation and it is still not fully understood. Also Huber et al. (2011) states that the asteroseismic scaling relations for $\nu_{\max}$ and $\Delta\nu$ are not fully appropriate for red giants. Smaller differences are obtained between the measured $\nu_{\max}$ and the inferred value for the stellar model for stars in the RC phase, since $\nu_{\max}$ was one of the three parameters used to determine the best stellar model (Section 4.3.2).

The values deduced for $\nu_{\max}$ are compatible with the literature values stated in Table 2.1, differing on average by only 1.4%. However, they do not agree within the uncertainty. This is possibly caused by the larger timebase for the *Kepler* data used in this work. In fact, only the first four months observations from *Kepler* were used by Hekker et al. (2011b), as opposed to the 1152 days-long observations used in this work.

The estimated values for $\Delta\nu$, determined by the scaling relation with $\nu_{\max}$ (Equation 3.5), do not always agree very well to the values obtained through the Bayesian MCMC method. However, they provide valuable initial guesses to set the region of interest in the ACF. The deduced values of the Bayesian MCMC method correspond very well with values determined from the LS method, less than 0.4%. However, there is a significant discrepancy for KIC 10593078. In order to be consistent throughout this work, the values derived by means of the MCMC approach are accepted as the deduced large frequency separations for the stars in the sample.

A further inspection of the ACF for the PSD of KIC 10593078 indicated that no significant peaks are found at 15.459 μHz (Figure 5.9). The strong maximum is at roughly 15.31 μHz. However, the marginal distribution for $\Delta\nu$ (Figure 5.10) indicates a clear identification of $\Delta\nu$. The difference between the two values for $\Delta\nu$ remains unclear.

Small differences between the values for $\Delta\nu$ deduced in this work (Table 5.2) and the values from the literature (Table 2.1) are observed. The differences are on average 0.8% (while the 1σ uncertainty is 0.2%) and could be due to a combination of several effects. First, the literature values for $\Delta\nu$ derived by Kallinger et al. (2010b) were determined by a different method in their case. A direct fit to the PSD allowed to determine $\Delta\nu$, while this work uses the method of the ACF. Second, the obtained maximum in the ACF was fitted by a Lorentzian profile in this work instead of accepting the $\Delta\nu$ with the highest ACF. Lastly, the longer timespan of the data used in this work has improved the SNR of the maximum in the ACF of the PSD. Therefore, it is not fully clear yet, if a fit to the ACF is needed, or the $\Delta\nu$ corresponding to the maximum in the ACF should be accepted.

5.5.2 The True Period Spacing $\Delta\Pi_1$

Matching the values derived from the fit to the period spacing ΔP and those deduced from the gridsearch in multi-parameter space shows notable differences. These differences correspond to 5.4% and are therefore not to the extent that a misidentification of the evolutionary stage is possible. No clear trend is visible in this comparison, though it would be expected that the fit to ΔP would underestimate the value of $\Delta\Pi_1$. The underestimation would be supported by the lack of measured ΔP in the region where the continuum background is present. However, for most stars a slight to medium overestimation is seen compared to the values derived from the asymptotic relation. This is likely related to the

star is held in Section 5.5.3.

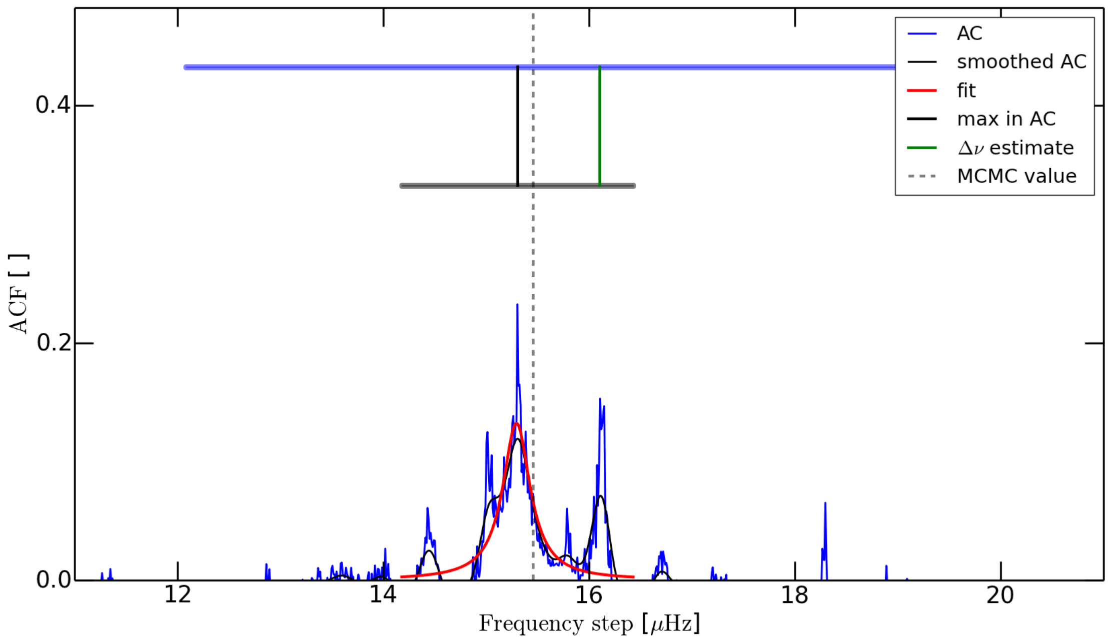

Figure 5.9: The determination of $\Delta\nu$ for KIC 10593078, where the ACF is given in blue. The green line represents the estimate for $\Delta\nu$, obtained from Equation 3.5. The maximum in the ACF shaded blue region (i.e. the search interval) is fitted by a Lorentzian profile (red line) to determine $\Delta\nu$. The deduced large frequency separation is given by the black line. The value for $\Delta\nu$ obtained by the MCMC is indicated by the gray dashed line.

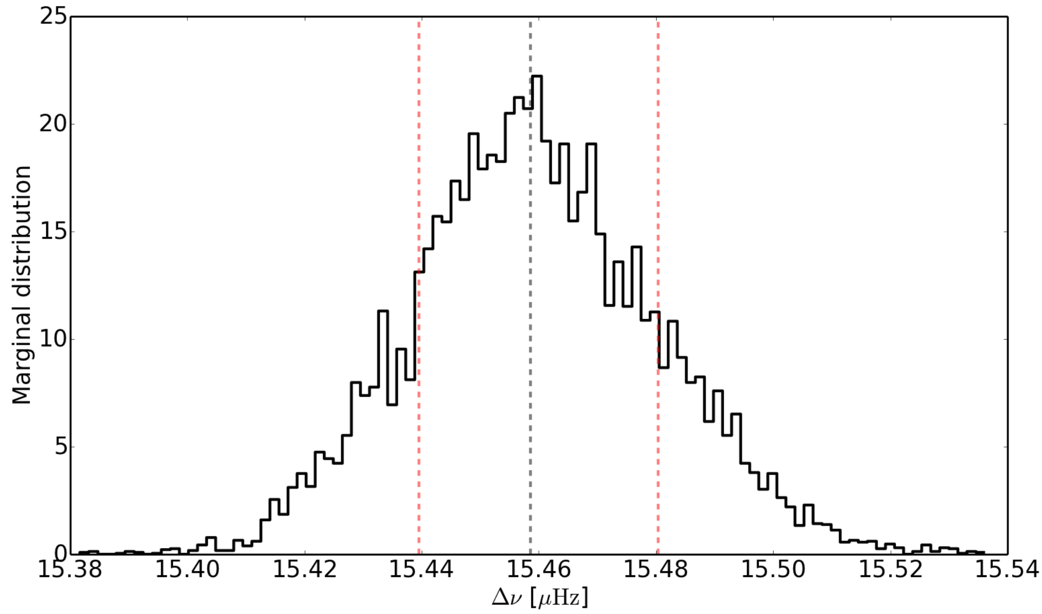

Figure 5.10: The marginal distribution for the large frequency separation $\Delta\nu$ for KIC 10593078, determined with the Bayesian MCMC fit to the ACF. The median value is indicated by gray dashed line and the 16% and 84% percentile are indicated by the red dashed lines.

boundaries used for defining the LS fitting interval of the continuum, which ranges within 85% to 115% of the maximum observed ΔP.

The extracted dipole mixed modes from the PSD were compared with the frequencies inferred from the asymptotic relation in a frequency and period échelle (Figure 5.7 and Appendix D). These observed frequencies resemble very well the pattern of the dipole mixed modes computed from the asymptotic relation, therefore the deduced coupling strength q and true period spacing $\Delta\Pi_1$ from the asymptotic relation are accepted as the final values for each star.

There is a notable difference between the $\ell = 1$ frequencies extracted from the artificial PSD of Ziva and the deduced dipole mixed mode frequencies from the asymptotic description (Figure D.9). This difference is most pronounced in the period échelle, where the observed frequencies converted into periods are indicated. This difference is not fully understood and further inspection of the simulated PSD has to be done in order to understand where the discrepancies arise.

The uncertainties on $\Delta\Pi_1$ obtained with the MCMC fit to ΔP provide an indication about the quality of the data. Even though the frequencies of the dipole mixed modes are in general well defined, with an average uncertainty of roughly 0.02 μHz, the uncertainty on $\Delta\Pi_1$corresponds to approximately 1.9% [2].

For the gridsearch method, the determination of the 1σ uncertainty on $\Delta\Pi_1$ was challenging. When the optimal solution (corresponding to the narrow dip of the global minimum of the chi-squared distribution) would be considered, the uncertainty would be very small, of the order of 10^{-2} s. However, from the fit to ΔP it is clear that the uncertainty inherent to the data is about 10^2 times larger, and this cannot be reduced significantly by changing the method to determine $\Delta\Pi_1$. Therefore, it was chosen to take the difference to the closest secondary minima as the uncertainty on the true period spacing $\Delta\Pi_1$, also given that the neighbour local minima are very close in chi-squared level.

Using this definition for the uncertainty on $\Delta\Pi_1$ deduced by the asymptotic relation, a $\chi^2_{1\sigma}$ is obtained, which is used to determine the uncertainties on q (Table 5.4). The uncertainties on q are, however, rather large, up to 160%. The detection of dipole mixed modes in the region of the $\ell = 0$ and $\ell = 2$ modes would increase the accuracy and precision on q, since these correspond to the steep rises in the period échelles (see e.g. Figure 5.7). It is therefore reasonable to assume that the derived 1σ uncertainties on q are large due to the non-detection of dipole mixed modes close to the regions of the $\ell = 0$ and $\ell = 2$ modes, causing q to remain undetermined.

Comparing the deduced values for $\Delta\Pi_1$ and q with the literature values for KIC 6928997 and KIC 10593078 (Mosser et al. 2012b) (Section 2.2) a very good agreement is found since the measurements are exactly the same. The largest difference is seen for the uncertainties on the deduced parameters. In fact, these uncertainties are about 10^2 times larger than those provided by Mosser et al. (2012b).

The determined $\Delta\Pi_1$ for the stellar models, by integrating the Brunt-Väisälä frequency N over the g mode cavity (Equation 1.13), corresponds very well with the determined value using the asymptotic approximation, since all the values are within the proposed

[2]This is when the uncertainty of KIC 6762022 is not taken into account for the calculation of the average uncertainty. KIC 676022 has a much larger uncertainty compared to the other stars, and it remains unclear if this is related to the evolutionary stage of the star, since it is the only RC star. When the uncertainty is, however, taken into account, an average uncertainty of 3.4% is obtained.

uncertainty, except for KIC 6928997 which differs of about 6%. Since both the literature and this work provide the same value for $\Delta\Pi_1$ measured from the dipole mixed modes in the *Kepler* PSD, it is more likely that the difference is introduced by the stellar model.

The values for $\Delta\Pi_1$ determined by the integral of N agree very well with the fit of the deduced ΔP from the stellar model (Table 5.7 and Appendix C), on average less than 0.8%. This is expected since more values of ΔP are provided in comparison with the extracted modes for the observations.

5.5.3 Comparison between Mode Extraction, Application of the Asymptotic Relation and Stellar Modelling

The results for the extracted frequencies from the PSD, the dipole mixed modes calculated with the asymptotic relations and the modelled frequencies with ADIPLS for the RGB stars are compared in Appendix E on one single figure for each star. Presenting all the results on one figure makes a qualitative comparison possible.

The frequencies of the dipole mixed modes, deduced with the asympotic relation, are well suited at describing the extracted modes of the PSD. This was already seen from the comparison in the frequency and period échelle diagrams (Section 5.5.2), but the comparison with the peak bagged PSD shows some extra features. The asymptotic description shows that some of the peaks that fall below the SNR threshold adopted are possible dipole mixed modes. These modes are seen all across the PSD and not only in the region where $\ell = 1$ modes are expected. These modes are however not considered in the analysis, since noise could possibly be picked up. Furthermore, it was not sure that these modes could unambiguously be identified as dipole modes. For KIC 6928997 and Ziva it was noted that significant modes identified as an $\ell = 3$ mode are extracted at a position where the asymptotic relation indicate that dipole mixed modes are present. Taking up these $\ell = 3$ modes could have added extra information to the gridsearch. Again, these modes could not unambiguously be identified as dipole modes. Since the $\ell = 3$ modes were only observed in one radial order only of the PSD, one should ponder about their intrinsic nature.

Except for the artificial PSD Ziva, there are rather large differences between the frequencies coming from the best stellar pulsation model found and the extracted modes. These differences are most notable in the region of the dipole mixed modes. The pulsation model obtained for KIC 6928997 (Figure E.1) describes the dipole mixed modes very well in two radial orders, albeit, it fails reproducing these in the other three stars. A similar behaviour is seen for the model determined for KIC 10593078, where differences remain in all radial orders. These differences are, however, on average smaller than those observed for KIC 6928997. The variations between pulsation model and extracted modes are most likely caused by the stellar evolution model. A fairly simplistic manner of stellar modelling was used, which only depends on the photospheric mass and radius, and the average metallicity Z, which is presumed to scale with the solar composition when the star has a different metallicity compared to the Sun. Many more parameters should be included in a further attempt to model the RGB stars in order to retrieve more realistic stellar models.

Table 5.7: The derived $\Delta\Pi_1$ of the stellar models for the RGB stars in the sample, according to both methods. These values are deduced from the integral of the Brunt-Väisälä frequency N over the g mode cavity (Equation 1.13) and the fit to ΔP.

	$\Delta\Pi_1$ (s) model	$\Delta\Pi_1$ (s) model ΔP fit
KIC 6928997	72.94	72.79
KIC 10593078	81.83	83.72
Ziva	70.35	70.39

5.5.4 Ziva: The hare-and-hound Exercise

Once all asteroseismic parameters for the artificial PSD Ziva is extracted and the most likely stellar model has been identified, the obtained values were compared with the input values. A model with $R = 6.90$ $R_\odot$, $M = 1.44$ $M_\odot$ and $T_{\mathrm{eff}} = 4899$ K is obtained from the stellar modelling, while the input parameters for the simulator were $R = 6.99$ $R_\odot$, $M = 1.50$ $M_\odot$ and $T_{\mathrm{eff}} = 4914$ K. These agree reasonably well and the differences are likely caused by systematics in the analyis and by the simulator itself.

The stellar modelling of Ziva had some difficulties (Section 5.4.1), since the scaling relations initially indicated a different modelling grid. These differences are likely related to the implemented method to determine the frequency of maximum oscillation power ν_{max} in the simulator. The equations used to obtain the amplitude and mode lifetime of the oscillations (Equations 2.1 and 2.2) are only approximately valid, and used to obtain oscillation modes with the same observational behaviour as those seen in the PSD of *Kepler* observations. These equations will be subsequently improved during the further development of the simulator and the effects of granulation will be added to the PSD.

Conclusions

In this thesis a detailed observational and theoretical seismic analysis of three red giants, which were observed with the NASA *Kepler* space telescope for 1152 (Q0 - Q13) days, was presented. For all except one star, KIC 6928997, quasi-uninterrupted data were available. The study of each star was partitioned into an observational and theoretical analysis, in order to determine the evolutionary phase of the star. A repository of *Python* scripts has been developed in order to serve as a semi-automated pipeline.

In the first step, the seismic parameters were extracted from the PSD, calculated from 1152 days of *Kepler* observations. The PSD of a synthetic star with known parameters was also analysed in an hare-and-hound exercise. Significant oscillation modes were extracted from the PSD by means of a Bayesian MCMC method. The main objective was to explore the robustness of the solution for the true period spacing $\Delta\Pi_1$. Values are obtained from the empirical fit to the observed period spacings ΔP and by means of the asymptotic relation, described by Mosser et al. (2012b). The uncertainties on both $\Delta\Pi_1$ and the coupling factor q are also computed. Therefore, gridsearches of a large range in the corresponding parameters space of the true period spacing $\Delta\Pi_1$ and the coupling factor q are performed, in order to find the best values and reproduce the mixed mode frequency pattern from the asymptotic relation. The values deduced for $\Delta\Pi_1$ according to both methods discussed in this work correspond within 5.4% from each other.

In the second step the most likely stellar model was deduced for each star and the true period spacing was computed for each model by using the Brunt-Väisälä frequency. Differences between the frequency of maximum oscillation power, $\nu_{\max}$, and the large frequency separation, $\Delta\nu$, deduced from the models and those determined from the *Kepler* observations are 3% and 1.8%, where the 1σ uncertainties correspond to 0.4% and 0.2%, respectively. However, the values determined for $\Delta\Pi_1$ for the models and the observations agree within 0.4% for KIC 6762022, KIC 10593078 and Ziva, while the difference for KIC 6928997 is 5%, which is likely related to the stellar model since only the photospheric radius and mass, and the overall metallicity, are varied.

This study has shown that the small uncertainties stated by other works found in the literature are likely to be too optimistic. While Mosser et al. (2012b) report millisecond precision, errors on the order of a second are obtained. Therefore it is argued that a more realistic error would be of the order of $0.8 - 1.7\%$ of the computed $\Delta\Pi_1$. However, it is noted that this larger uncertainty still remains small compared to the difference in $\Delta\Pi_1$ needed to discriminate between different evolutionary stages (e.g. Bedding et al. 2011; Mosser et al. 2012b; Stello et al. 2013). Although the result does not change the interpretation of $\Delta\Pi_1$, it is important for a better understanding of the observables and the study of their accuracy.

The uncertainties on the coupling strength q are however on an average 160%, meaning that q stays undetermined within the range investigated (ranging from 0.01 up to 0.51). This is likely related to the lack of dipole mixed modes in the most sensitive regions of the PSD, namely around the $\ell = 0$ and $\ell = 2$ modes.

The inclusion of an artificial star in the analysis provided a good step forward for detecting possible systematics inherent to the analysis. In particular, it is noticeable that the synthetic PSD shows some problems related to the current development of the simulator, making quantitative conclusions regarding the systematics difficult. This suggests that in the near-future the description for the amplitudes and mode lifetimes shall be improved and granulation effects have to be included.

In this thesis, it was shown that the usage of gridsearch techniques is a necessary tool for the understanding of the properties and uncertainties of both the true period spacing $\Delta\Pi_1$ and the coupling factor q. Currently, the methodology presented in this work is dedicated to stars that do not show the effects of rotation in the PSD, and represents a limited sample. It is known from large sample surveys of red giants observed with the NASA *Kepler* space telescope that about 80% of all stars rotate (Mosser et al. 2012a; Beck 2013). The induced rotational splitting of non-radial, mainly dipole modes, complicates the power spectrum enormously. Mosser et al. (2012b) presented an extension of the asymptotic relation that also takes the modulation of the rotational splitting into account. Implementing these additional parameters describing rotation into the tools developed within this work, will hopefully help to solve the characterisation of all the oscillations observed in stars' power spectra, in which the effects of rotational splitting cannot be disentangled from the spacing of mixed modes through $\Delta\Pi_1$.

The implications of the larger uncertainties will only become evident from a detailed stellar modelling of a large sample of star. This is however beyond the scope of this work, since it would involve the computation of large grids of models for every star.

Bibliography

Aerts, C., Christensen-Dalsgaard, J., & Kurtz, D. W. 2010, Asteroseismology

Aizenman, M., Smeyers, P., & Weigert, A. 1977, A&A, 58, 41

Akaike, H. 1974, IEEE Transactions on Automatic Control, 19, 716

Anderson, E. R., Duvall, Jr., T. L., & Jefferies, S. M. 1990, ApJ, 364, 699

Angulo, C., Arnould, M., Rayet, M., et al. 1999, Nuclear Physics A, 656, 3

Barban, C., Matthews, J. M., De Ridder, J., et al. 2007, A&A, 468, 1033

Beck, P. G. 2013, Ph.D. dissertation, KU Leuven

Beck, P. G., Bedding, T. R., Mosser, B., et al. 2011, Science, 332, 205

Beck, P. G. & Kallinger, T. 2013, Sterne und Weltraum, 4, 50

Beck, P. G., Montalban, J., Kallinger, T., et al. 2012, Nature, 481, 55

Bedding, T. R., Huber, D., Stello, D., et al. 2010, ApJL, 713, L176

Bedding, T. R. & Kjeldsen, H. 2003, PASA, 20, 203

Bedding, T. R., Mosser, B., Huber, D., et al. 2011, Nature, 471, 608

Belkacem, K., Goupil, M. J., Dupret, M. A., et al. 2011, A&A, 530, A142

Benomar, O., Belkacem, K., Bedding, T. R., et al. 2014, ApJL, 781, L29

Berg, B. 2004, Markov Chain Monte Carlo Simulations and Their Statistical Analysis

Böhm-Vitense, E. 1958, ZAp, 46, 108

Borucki, W. J., Koch, D., Basri, G., et al. 2010, Science, 327, 977

Brown, T. M., Gilliland, R. L., Noyes, R. W., & Ramsey, L. W. 1991, ApJ, 368, 599

Carrier, F., De Ridder, J., Baudin, F., et al. 2010, A&A, 509, A73

Cassisi, S. & Salaris, M. 2013, Old Stellar Populations: How to Study the Fossil Record of Galaxy Formation

Chaplin, W. J., Bedding, T. R., Bonanno, A., et al. 2011a, ApJL, 732, L5

Chaplin, W. J., Houdek, G., Elsworth, Y., et al. 2005, MNRAS, 360, 859

Chaplin, W. J., Kjeldsen, H., Christensen-Dalsgaard, J., et al. 2011b, Science, 332, 213

Chaplin, W. J., Kjeldsen, H., Christensen-Dalsgaard, J., et al. 2013, ArXiv e-prints

Charpinet, S., Fontaine, G., Brassard, P., et al. 1997, ApJL, 483, L123

Christensen-Dalsgaard, J. 1982, Advances in Space Research, 2, 11

Christensen-Dalsgaard, J. 2002, Reviews of Modern Physics, 74, 1073

Christensen-Dalsgaard, J. 2004, Solar Physics, 220, 137

Christensen-Dalsgaard, J. 2008a, Ap&SS, 316, 113

Christensen-Dalsgaard, J. 2008b, Ap&SS, 316, 13

Christensen-Dalsgaard, J., Bedding, T. R., & Kjeldsen, H. 1995, ApJL, 443, L29

Christensen-Dalsgaard, J., Dappen, W., Ajukov, S. V., et al. 1996, Science, 272, 1286

Christensen-Dalsgaard, J. & Frandsen, S. 1983, Solar Physics, 82, 469

Corsaro, E., Fröhlich, H.-E., Bonanno, A., et al. 2013, MNRAS, 430, 2313

De Ridder, J., Arentoft, T., & Kjeldsen, H. 2006a, MNRAS, 365, 595

De Ridder, J., Barban, C., Baudin, F., et al. 2009, Nature, 459, 398

De Ridder, J., Barban, C., Carrier, F., et al. 2006b, A&A, 448, 689

Deheuvels, S. & Michel, E. 2010, AP&SS, 328, 259

Dupret, M.-A., Belkacem, K., Samadi, R., et al. 2009, A&A, 506, 57

Duvall, Jr., T. L. & Harvey, J. W. 1986, in NATO ASIC Proc. 169: Seismology of the Sun and the Distant Stars, ed. D. O. Gough, 105–116

Dziembowski, W. A. & Pamiatnykh, A. A. 1993, MNRAS, 262, 204

Eddington, A. S. 1926, The Internal Constitution of the Stars

Eggenberger, P., Miglio, A., Montalban, J., et al. 2010, A&A, 509, A72

Elsworth, Y., Howe, R., Isaak, G. R., et al. 1995, Nature, 376, 669

Ferguson, J. W., Alexander, D. R., Allard, F., et al. 2005, ApJ, 623, 585

Frandsen, S., Carrier, F., Aerts, C., et al. 2002, A&A, 394, L5

García, R. A., Hekker, S., Stello, D., et al. 2011, MNRAS, 414, L6

Gautschy, A. & Saio, H. 1993, MNRAS, 262, 213

Gizon, L. & Solanki, S. K. 2003, ApJ, 589, 1009

Goldreich, P. & Keeley, D. A. 1977, ApJ, 212, 243

Grec, G., Fossat, E., & Pomerantz, M. A. 1983, Solar Physics, 82, 55

Grevesse, N. & Noels, A. 1993, in Origin and Evolution of the Elements, ed. N. Prantzos, E. Vangioni-Flam, & M. Casse, 15–25

Gruberbauer, M., Kallinger, T., Weiss, W. W., & Guenther, D. B. 2009, A&A, 506, 1043

Handberg, R. & Campante, T. L. 2011, A&A, 527, A56

Harvey, J. 1985, in ESA Special Publication, Vol. 235, Future Missions in Solar, Heliospheric & Space Plasma Physics, ed. E. Rolfe & B. Battrick, 199–208

Hekker, S., Aerts, C., De Ridder, J., & Carrier, F. 2006, A&A, 458, 931

Hekker, S., Basu, S., Stello, D., et al. 2011a, A&A, 530, A100

Hekker, S., Elsworth, Y., De Ridder, J., et al. 2011b, A&A, 525, A131

Hekker, S., Kallinger, T., Baudin, F., et al. 2009, A&A, 506, 465

Henyey, L. G., Forbes, J. E., & Gould, N. L. 1964, ApJ, 139, 306

Henyey, L. G., Wilets, L., Böhm, K. H., Lelevier, R., & Levee, R. D. 1959, ApJ, 129, 628

Houdek, G., Balmforth, N. J., Christensen-Dalsgaard, J., & Gough, D. O. 1999, A&A, 351, 582

Huber, D., Bedding, T. R., Stello, D., et al. 2011, ApJ, 743, 143

Huber, D., Bedding, T. R., Stello, D., et al. 2010, ApJ, 723, 1607

Hummer, D. G. & Mihalas, D. 1988, ApJ, 331, 794

Iglesias, C. A. & Rogers, F. J. 1996, ApJ, 464, 943

Kallinger, T., De Ridder, J., Hekker, S., et al. 2014, In. prep.

Kallinger, T., Mosser, B., Hekker, S., et al. 2010a, A&A, 522, A1

Kallinger, T., Weiss, W. W., Barban, C., et al. 2010b, A&A, 509, A77

Kjeldsen, H. & Bedding, T. R. 1995, A&A, 293, 87

Kjeldsen, H., Bedding, T. R., & Christensen-Dalsgaard, J. 2008, ApJL, 683, L175

Liddle, A. R. 2004, MNRAS, 351, L49

Montalbán, J., Miglio, A., Noels, A., Scuflaire, R., & Ventura, P. 2010, ApJL, 721, L182

Mosser, B., Barban, C., Montalbán, J., et al. 2011, A&A, 532, A86

Mosser, B., Belkacem, K., Goupil, M.-J., et al. 2010, A&A, 517, A22

Mosser, B., Elsworth, Y., Hekker, S., et al. 2012a, A&A, 537, A30

Mosser, B., Goupil, M. J., Belkacem, K., et al. 2012b, A&A, 540, A143

Pinsonneault, M. H., An, D., Molenda-Żakowicz, J., et al. 2012, ApJS, 199, 30

Rogers, F. J. & Nayfonov, A. 2002, ApJ, 576, 1064

Schwarz, G. 1978, The Annals of Statistics, 6, 461

Serenelli, A. M., Basu, S., Ferguson, J. W., & Asplund, M. 2009, ApJL, 705, L123

Stello, D., Chaplin, W. J., Basu, S., Elsworth, Y., & Bedding, T. R. 2009, MNRAS, 400, L80

Stello, D., Huber, D., Bedding, T. R., et al. 2013, ApJL, 765, L41

Tassoul, M. 1980, ApJS, 43, 469

Tassoul, M. 1990, ApJ, 358, 313

Ulrich, R. K. 1986, ApJL, 306, L37

Unno, W., Osaki, Y., Ando, H., Saio, H., & Shibahashi, H. 1989, Nonradial oscillations of stars

Vitense, E. 1953, ZAp, 32, 135

Weiss, A. & Schlattl, H. 2008, Ap&SS, 316, 99

Appendix A

Equations of Stellar Structure and Stellar Oscillations

Stellar evolution models solve the equations of stellar structure at discrete timesteps to describe the evolution of the star. These equations are presented in Section A.1. The equations of stellar pulsations are given in Section A.2, which are used to describe the characteristics of the stellar pulsations.

A.1 Equations of Stellar Structure

The equations of stellar structure and evolution describe the physical behaviour of a star given certain physical properties. These are the equation of hydrodynamics, the description of the temperature gradient, the energy equation and the equation of the chemical evolution for all chemical elements. The equations of stellar structure can be written as a function of the independent variable $x = \log_{10}(q) = \log_{10}(m_r/M)$, where q is the mass fraction, describing the fraction of the mass m_r inside a radius r for a star with a total photospheric mass M (Christensen-Dalsgaard 2008b). Using x, the equations are expressed as

$$\frac{\partial \log_{10}(r)}{\partial x} = \frac{M}{4\pi\rho}\frac{q}{r^3} \, , \tag{A.1}$$

$$\frac{\partial \log_{10}(p)}{\partial x} = -\frac{GM^2}{4\pi}\frac{q^2}{r^4 p} \, , \tag{A.2}$$

$$\frac{\partial \log_{10}(T)}{\partial x} = \nabla \frac{\partial \log_{10}(r)}{\partial x} \, , \tag{A.3}$$

$$\frac{\partial \log_{10}(L)}{\partial x} = M\left(\epsilon - \frac{\partial H}{\partial t} + \frac{1}{\rho}\frac{\partial p}{\partial t}\right)\frac{q}{L} \, , \tag{A.4}$$

$$\frac{\partial X_k}{\partial t} = \mathcal{R}_k + \frac{\partial}{\partial m}\left(\mathcal{D}_k \frac{\partial X_k}{\partial m}\right) + \frac{\partial}{\partial m}(\mathcal{V} X_k) \text{ where} \tag{A.5}$$
$$k = 1, \ldots, K \, .$$

Here r is the distance to the center, ρ is the density, p is the pressure, G is the universal gravitational constant, T is the temperature, L is the luminosity at r, ϵ is the energy generation rate per unit mass, H is the enthalpy per unit mass, X_k is the mass fraction of element k, $\mathcal{R}_k$ is the rate of change of X_k due to nuclear reactions, $\mathcal{D}_k$ and $\mathcal{V}_k$ are the respectively the diffusion and settling coefficients for chemical element k. The temperature gradient $\nabla = \mathrm{d}\ \ln(T)/\mathrm{d}\ \ln(p)$ depends on the type of dominant energy transport, either convective or radiative transport. Both $\mathcal{D}_k$ and $\mathcal{V}_k$ are neglected in the calculations with ASTEC in this work.

Appropriate boundary conditions are set up to solve the equations of stellar structure and evolution. The most obvious boundary conditions are set up at the center of the star, $r = 0$, and at the stellar surface. Extra care has to be taken for the center of the star which acts as a singular point. The equations of stellar structure and evolution are numerically solved according to the Newton-Raphson scheme, known as the Henyey scheme in the context of stellar evolution (Henyey et al. 1959, 1964).

A.2 Equations of Stellar Oscillations

Stellar oscillations can be theoretically described as a perturbation of the equilibrium structure, defined by the equations of stellar structure and evolution. This perturbation is accompanied by a displacement $\delta\mathbf{r}$, which can be described in spherical coordinates (r, θ, ϕ) for a non-radial mode as

$$\delta\mathbf{r} = \mathrm{Re}\left\{\left[\xi_r(r)Y_\ell^m(\theta,\phi)\mathbf{a}_r + \xi_h(r)\left(\frac{\partial Y_\ell^m}{\partial\theta}\mathbf{a}_\theta + \frac{1}{\sin\theta}\frac{\partial Y_\ell^m}{\partial\phi}\mathbf{a}_\phi\right)\right]\exp(-i\omega t)\right\} \ . \tag{A.6}$$

$Y_\ell^m(\theta,\phi) = c_{\ell m}P_\ell^m(\cos\theta)\exp(im\phi)$ is a spherical harmonic of degree ℓ and azimuthal order m, θ being the co-latitude and ϕ the longitude, $P_\ell^m(x)$ is an associated Legendre function and $c_{\ell m}$ is a suitable normalisation constant. $\mathbf{a}_r$, $\mathbf{a}_\theta$ and $\mathbf{a}_\phi$ are the unit vectors respectively in the r, θ and ϕ direction. The properties of the pulsation can be deduced under the adiabatic approximation, where the heating term in the energy equation is neglected (Equation A.4). Under the adiabatic approximation, the angular frequency ω of the mode is real and the amplitude functions $\xi_r(r)$, $\xi_h(r)$ and the Eulerian perturbation to pressure p' are also real.

The equations of adiabatic stellar oscillations are expressed according to the following variables

$$y_1 = \frac{\xi_r}{R} \ , \tag{A.7}$$

$$y_2 = x\left(\frac{p'}{\rho} + \Phi'\right)\frac{\ell(\ell+1)}{\omega^2 r^2} = \frac{\ell(\ell+1)}{R}\xi_h \ , \tag{A.8}$$

$$y_3 = -x\frac{\Phi'}{gr} \ , \tag{A.9}$$

$$y_4 = x^2\frac{\mathrm{d}}{\mathrm{d}x}\left(\frac{y_3}{x}\right) \ . \tag{A.10}$$

R is the photospheric radius of the stellar model and g is the deduced surface gravity. p' is the pressure perturbation and Φ' the perturbation to the gravitational potential. Using these variables, the equations describing the displacement vector $\delta\mathbf{r}$ are expressed as

$$x\frac{\mathrm{d}y_1}{\mathrm{d}x} = (A_2 - 2)y_1 + \left(1 - \frac{A_2}{\eta}\right) y_2 + A_2 y_3 \ , \tag{A.11}$$

$$x\frac{\mathrm{d}y_2}{\mathrm{d}x} = \left[\ell(\ell+1) - \eta A_4\right] y_1 + (A_4 - 1)y_2 + \eta A_4 y_3 \ , \tag{A.12}$$

$$x\frac{\mathrm{d}y_3}{\mathrm{d}x} = y_3 + y_4 \ , \tag{A.13}$$

$$x\frac{\mathrm{d}y_4}{\mathrm{d}x} = -A_4 A_5 y_1 - A_5\frac{A_2}{\eta} y_2 + \left[\ell(\ell+1) + A_5(A_4 - 2) + A_5 A_2\right] y_3 + 2(1 - A_5)y_4 \ . \tag{A.14}$$

$\eta = \ell(\ell+1)g/(\omega^2 r)$ and the terms A_i, which are the dimensionless variables describing the equilibrium model, are

$$x = r/R \ , \tag{A.15}$$

$$A_1 = q/x^3 \ , \text{ where } q = m/M \ , \tag{A.16}$$

$$A_2 = -\frac{1}{\Gamma_1}\frac{\mathrm{d}\,\ln(p)}{\mathrm{d}\,\ln(r)} = \frac{Gm\rho}{\Gamma_1 p r} \ , \tag{A.17}$$

$$A_3 = \Gamma_1 \ , \tag{A.18}$$

$$A_4 = \frac{1}{\Gamma_1}\frac{\mathrm{d}\,\ln(p)}{\mathrm{d}\,\ln(r)} - \frac{\mathrm{d}\,\ln(\rho)}{\mathrm{d}\,\ln(r)} \ , \tag{A.19}$$

$$A_5 = \frac{4\pi\rho r^3}{m} \ . \tag{A.20}$$

Here Γ_1 is defined as $(\partial \ln(p)/\partial \ln(\rho))_{ad}$.

These equations are solved in the full description in this work to deduce all the possible frequencies present in the stellar model[1]. Appropriate boundary conditions are set up in the center of the star, $r = 0$, and at the stellar surface. The equations are solved in ADIPLS according to a fourth order shooting method, where solutions that satisfy the boundary conditions are independently solved from one another. The eigenvalue of the equations is found by connecting these solutions at an appropriate mesh point x_f.

Once the frequencies and the corresponding eigenvalues are obtained for the stellar oscillations of spherical degree ℓ, additional parameters have to be determined. First, the order of the mode, which is estimated as

$$n = -\sum_{x_{z1}>0} \mathrm{sign}\left(y_2\frac{\mathrm{d}y_1}{\mathrm{d}x}\right) + n_0 \ , \tag{A.21}$$

where the sum is over the zeros $\{x_{z1}\}$ in y_1 and sign is the sign function. $n_0 = 1$ for radial modes and $n_0 = 0$ for non-radial modes when the model includes the center of the star.

[1]It is also possible to solve the equations of stellar oscillations according to the Cowling approximation, where the perturbation to the gravitational potential $\Phi'(r)$ is neglected. This reduces the order of the set of equations from fourth order to second order and is appropriate for the pulsation modes with large l and high radial order $|n|$. Because the focus lays on low degree, high radial order modes during this study, it has been chosen to use the full set of equations.

Second, the normalized mode inertia $\hat{E}$ is calculated, which provides a powerful diagnostic on the behaviour of the oscillation. This is defined as

$$\hat{E} = \frac{\int\limits_{x_1}^{x_s} \left[y_1^2 + y_2^2/\ell(\ell+1)\right] q A_5 \mathrm{d}x/x}{4\pi \left[y_1(x_{\mathrm{phot}})^2 + y_2(x_{\mathrm{phot}})^2/\ell(\ell+1)\right]} , \tag{A.22}$$

where $x_1 = r_1/R$ and $x_s = R_s/R$ is the fractional distance of the mesh point respectively closest to the center and to the radius of the star, while $x_{\mathrm{phot}} = R_{\mathrm{phot}}/R = 1$ is the photospheric radius. For the radial modes, the terms in y_2 are not included.

In the end of the simulation, ADIPLS provides a frequency ν, a spherical degree ℓ, a radial order n and a normalised mode inertia $\hat{E}$ for each pulsation present in the star.

Appendix B

Figures of Background Fitting and ACF

The figures indicating the background model for the PSD of the red giants are presented in this Chapter. The background includes the white noise component, the granulation contributions (except for Ziva) and the Gaussian power excess. The fit is performed by both a LS minimisation and a Bayesian MCMC, as described in Section 3.1.

The figures presenting the determination of $\Delta\nu$, according to the fitting method of the ACF (Section 3.2), are also given. These show the LS minimisation fit to the ACF with the different fitting and search regions indicated.

B.1 Figures of the Background Model

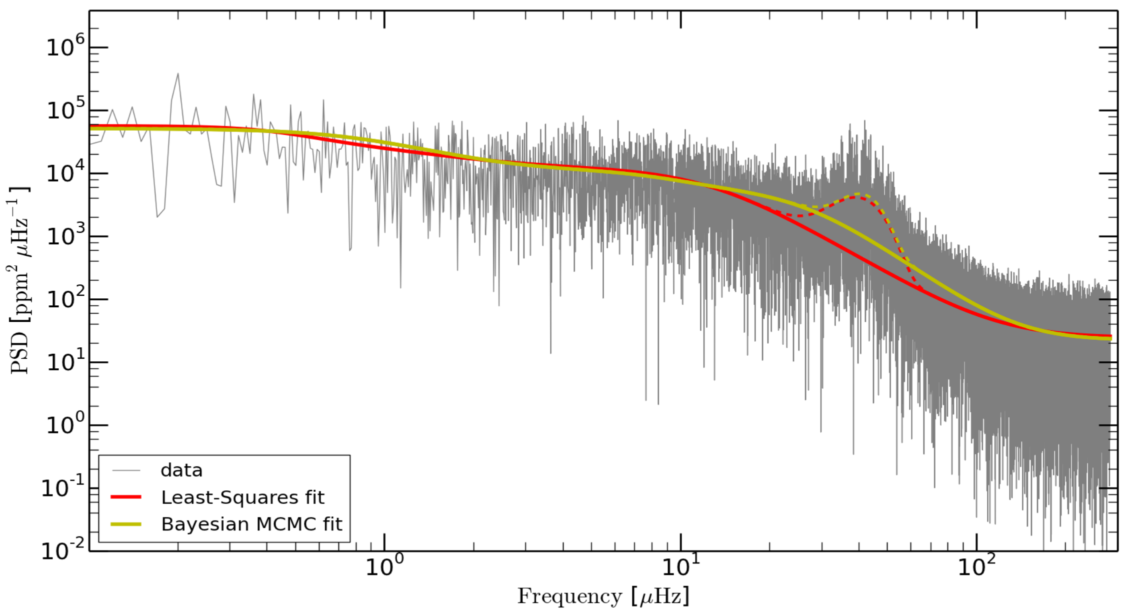

Figure B.1: The resulting background fit using the Bayesian approach (solid yellow line) to the PSD (gray) of KIC 6762022. The initial fit using the LS minimisation is given by the red solid line. The yellow (red) dashed line is when the Gaussian power excess is included.

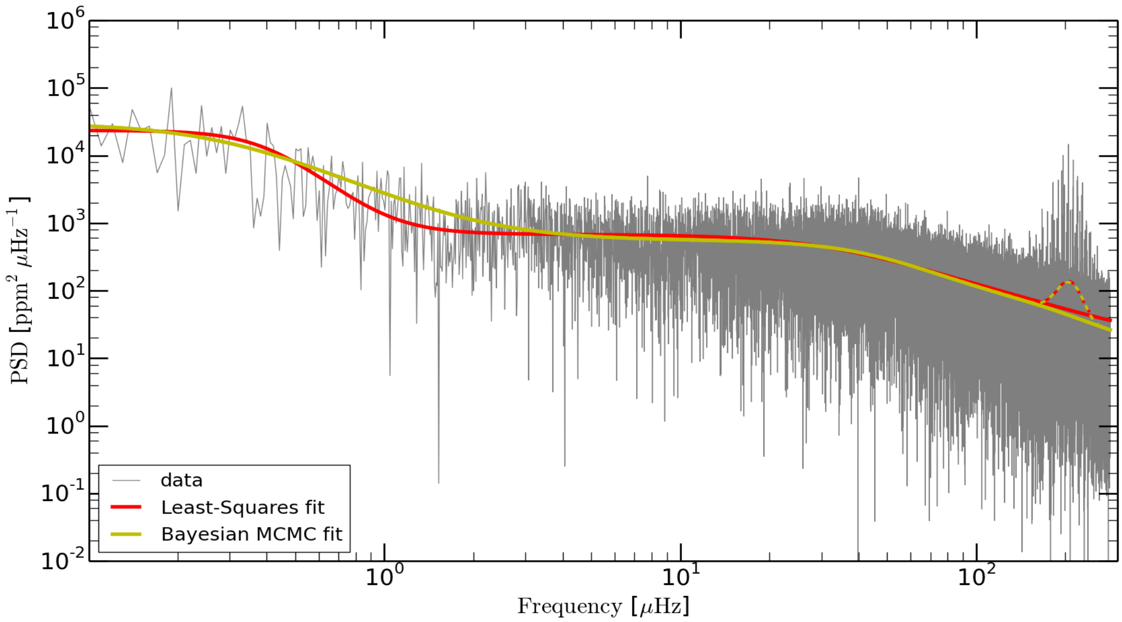

Figure B.2: The resulting background fit using the Bayesian approach (solid yellow line) to the PSD (gray) of KIC 10593078. The same colour coding as Figure B.1 is used to describe both fits.

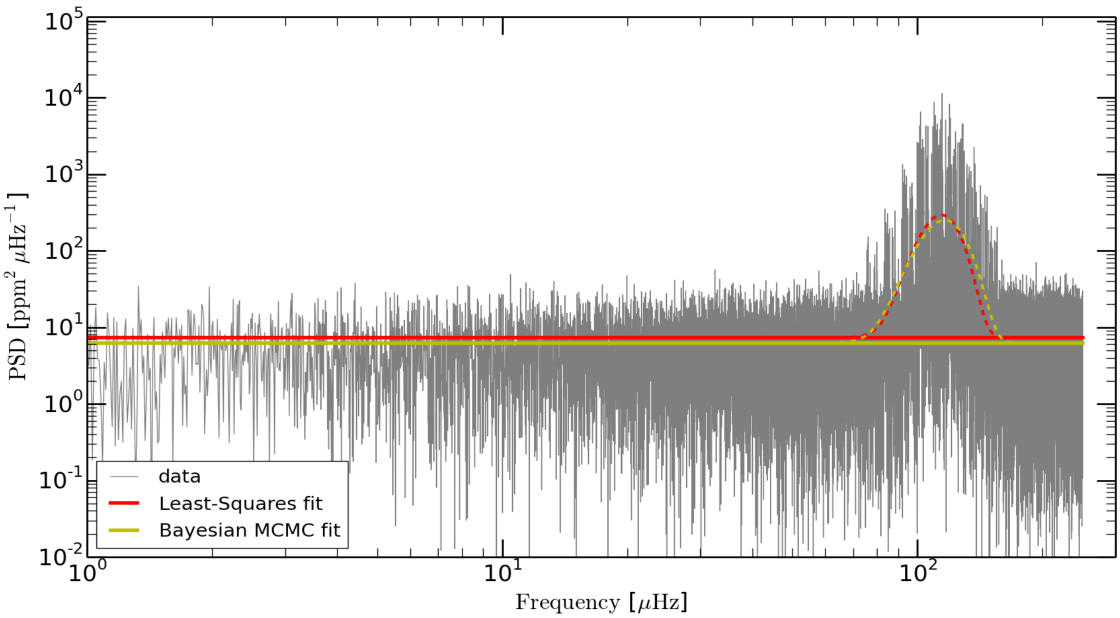

Figure B.3: The resulting background fit using the Bayesian approach (solid yellow line) to the PSD (gray) of Ziva. The same colour coding as Figure B.1 is used to describe both fits. For the artificial PSD no granulation contributions were used in the fit, since these were not present in the provided simulation.

B.2 Determining the Large Frequency Separation $\Delta\nu$

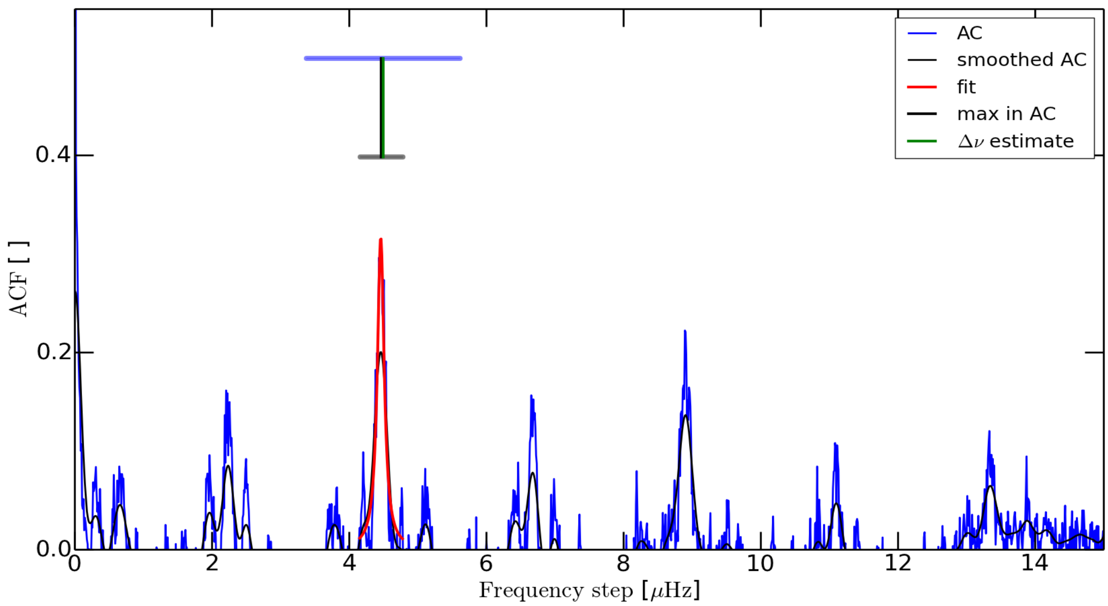

Figure B.4: The determination of $\Delta\nu$ for KIC 6762022, where the ACF is given in blue. The green line represents the estimate for $\Delta\nu$, obtained from Equation 3.5. The maximum in the ACF shaded blue region (i.e. the search interval) is fitted by a Lorentzian profile (red line) to determine $\Delta\nu$. The deduced large frequency separation is given by the black line.

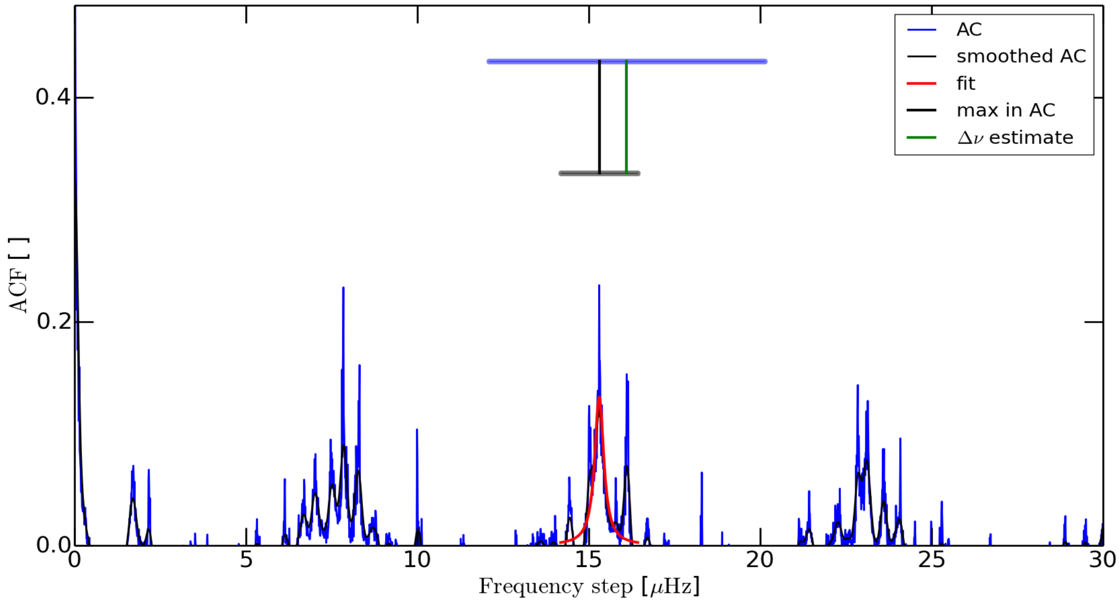

Figure B.5: The determination of $\Delta\nu$ for KIC 10593078, where the ACF is given in blue. The green line represents the estimate for $\Delta\nu$, obtained from Equation 3.5. The maximum in the ACF shaded blue region (i.e. the search interval) is fitted by a Lorentzian profile (red line) to determine $\Delta\nu$. The deduced large frequency separation is given by the black line.

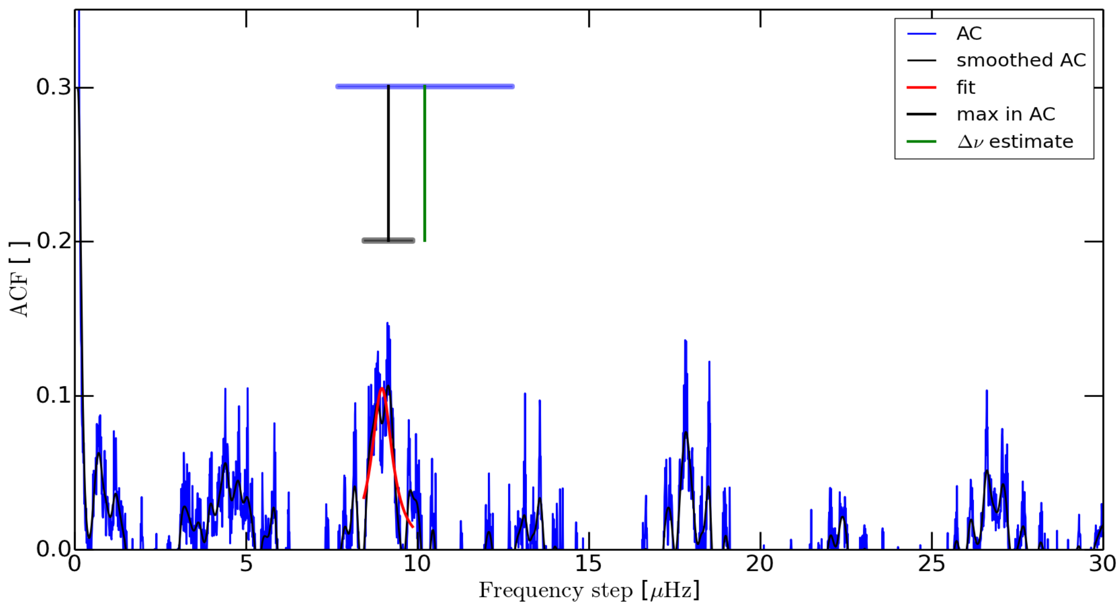

Figure B.6: The determination of $\Delta\nu$ for Ziva, where the ACF is given in blue. The green line represents the estimate for $\Delta\nu$, obtained from Equation 3.5. The maximum in the ACF shaded blue region (i.e. the search interval) is fitted by a Lorentzian profile (red line) to determine $\Delta\nu$. The deduced large frequency separation is given by the black line.

Appendix C

Determining $\Delta\Pi_1$ by Fitting the Period Spacing ΔP

The figures of the fit to the observed period spacing ΔP are given in this Chapter for each star of the sample. From this fit, the true period spacing $\Delta\Pi_1$ is obtained, which is used in the further analysis of the red giants.

Once a suitable pulsation model is retrieved with ASTEC for the RGB stars in the sample, the true period spacing is determined for this model. The method of using the fit to ΔP is also used to determine the true period spacing. The figures of this analysis are also presented in this chapter.

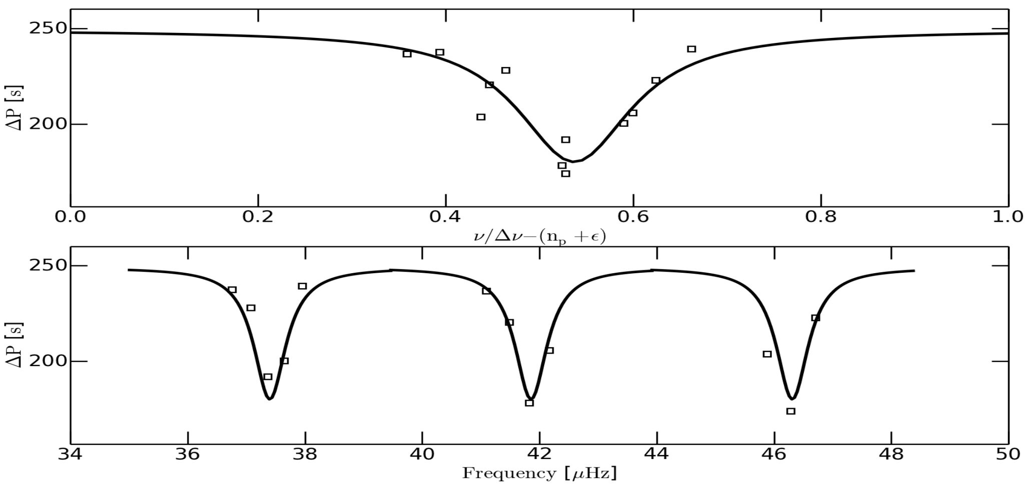

Figure C.1: Deducing $\Delta\Pi_1$ for KIC 6762022 using the empirical approach of fitting ΔP yielded $\Delta\Pi_1 = 249$ s. The fit is done for the phase shift θ (*top*) and subsequently expanded to ν, using the inverse relation of Equation 3.15.

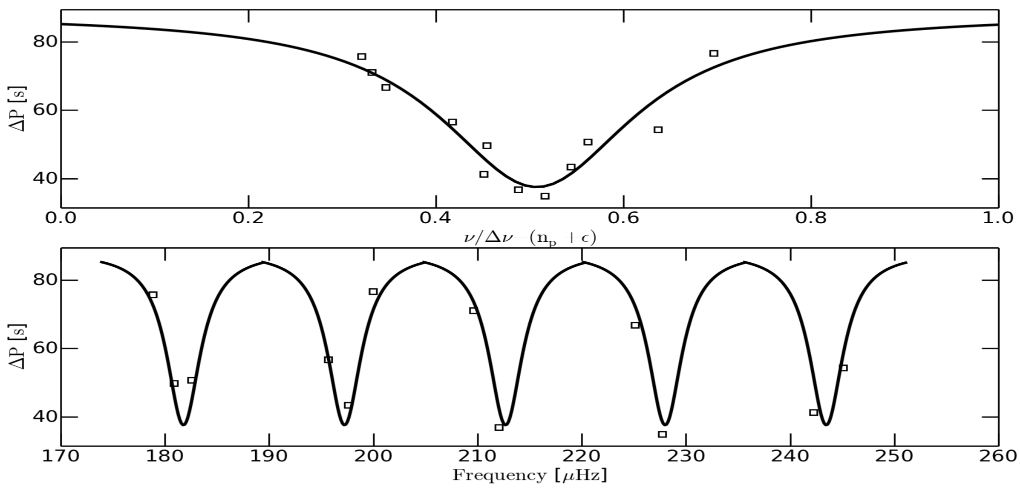

Figure C.2: Deducing $\Delta\Pi_1$ for KIC 10593078 using the empirical approach of fitting ΔP yielded $\Delta\Pi_1 = 88.11$ s.

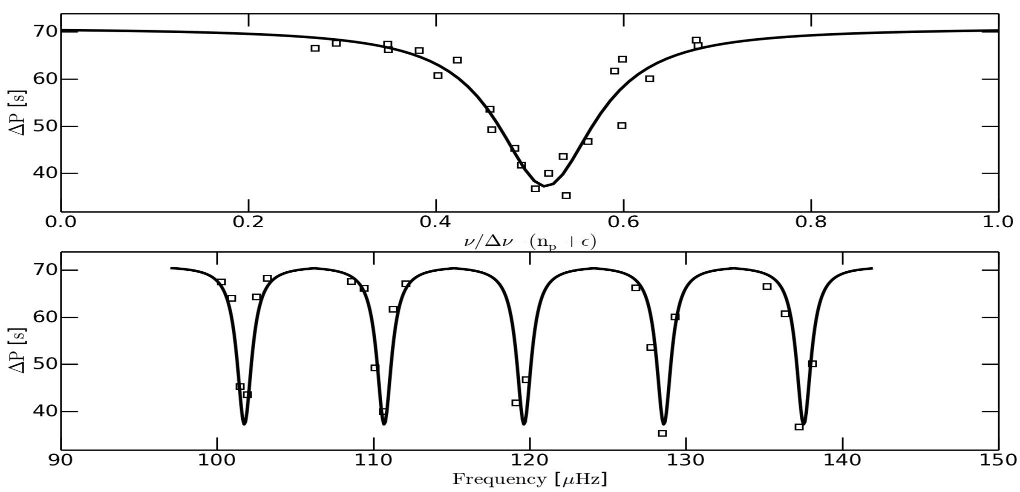

Figure C.3: Deducing $\Delta\Pi_1$ for Ziva using the empirical approach of fitting ΔP yielded $\Delta\Pi_1 = 70.89$ s.

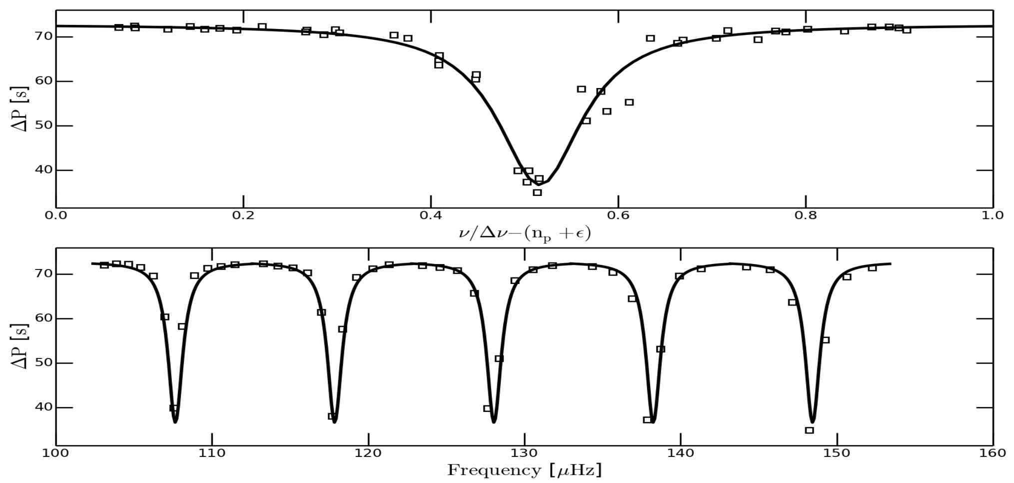

Figure C.4: Deducing $\Delta\Pi_1$ for the best ASTEC model for KIC 6928997. The model has $M = 1.46$ M$_\odot$, $R = 6.31$ R$_\odot$ and $Z = 0.03$. The empirical approach of fitting ΔP yielded $\Delta\Pi_1 = 72.94$ s.

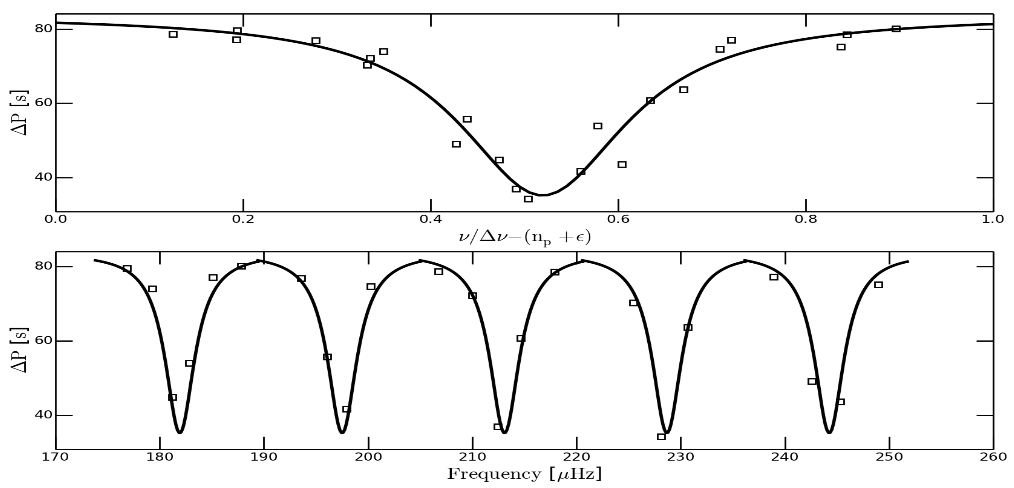

Figure C.5: Deducing $\Delta\Pi_1$ for the best ASTEC model for KIC 10593078. The model has $M = 1.37$ M$_\odot$, $R = 4.66$ R$_\odot$ and $Z = 0.03$. The empirical approach of fitting ΔP yielded $\Delta\Pi_1 = 83.72$ s.

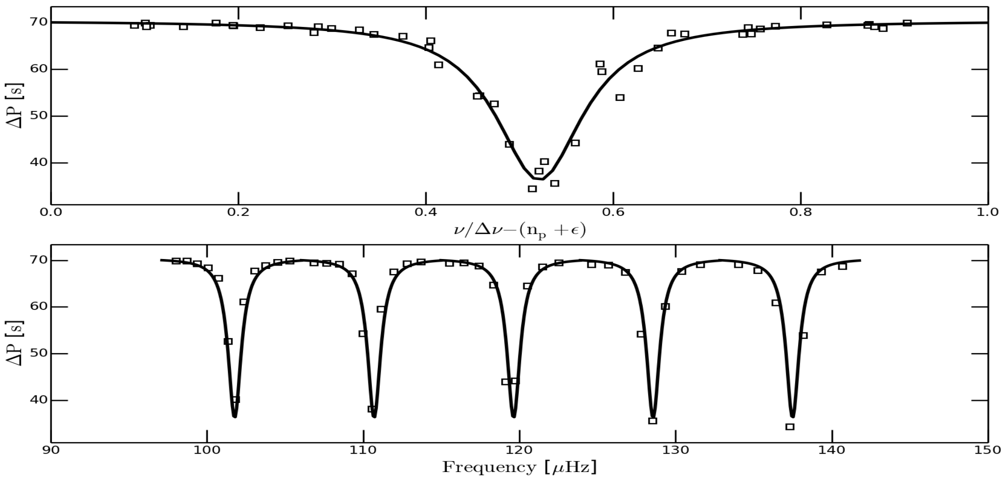

Figure C.6: Deducing $\Delta\Pi_1$ for the best ASTEC model for Ziva. The model has $M = 1.44$ M$_\odot$, $R = 6.90$ R$_\odot$ and $Z = 0.02$. The empirical approach of fitting ΔP yielded $\Delta\Pi_1 = 70.39$ s.

Appendix D

Figures of the Multi-Parameter Fit for $\Delta\Pi_1$

The figures describing the analysis of the asymptotic relation for the dipole mixed modes in the red giants are described in this Chapter. First, the grids are presented, which were used for the analysis of the multi-parameter fit for $\Delta\Pi_1$. Next, the frequency and period échelle diagrams are presented, making the comparison between the extracted modes from the PSD and the optimal description with the asymptotic relation. Finally, the uncertainty on the deduced parameters is calculated. The method is visualised in the figures of the last section.

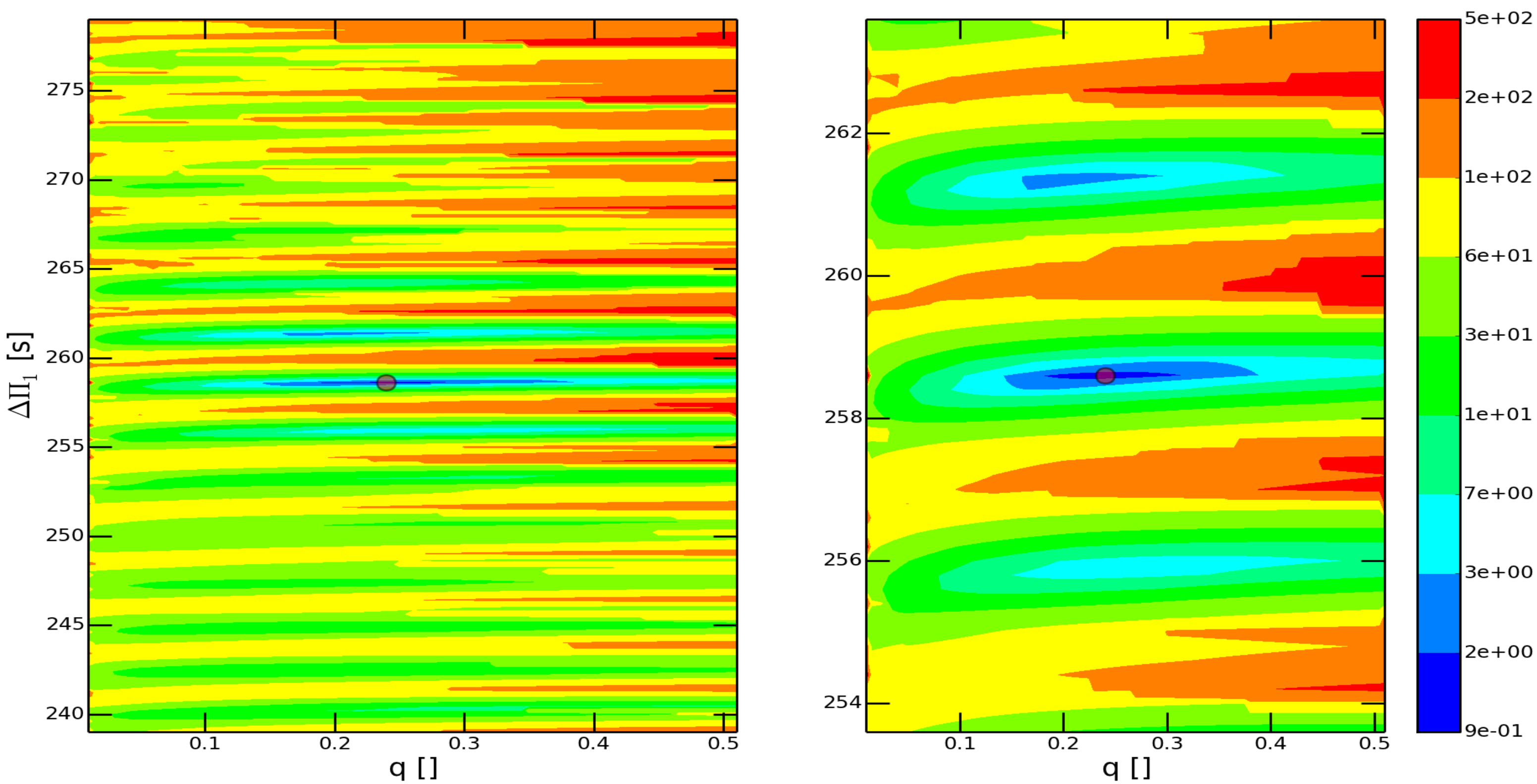

Figure D.1: *Left:* The results from the gridsearch to determine $(\Delta\Pi_1, q)$ using the asymptotic relation for KIC 6762022. The grid is composed of 201 meshpoints along the $\Delta\Pi_1$ axis and 101 along the q axis. The color scale indicates the $\chi^2_{\rm grid}$ derived from the grid search. The best solution for the pair of $(\Delta\Pi_1, q)$ is indicated by a dot. *Right:* A zoom of the region with the optimal solution.

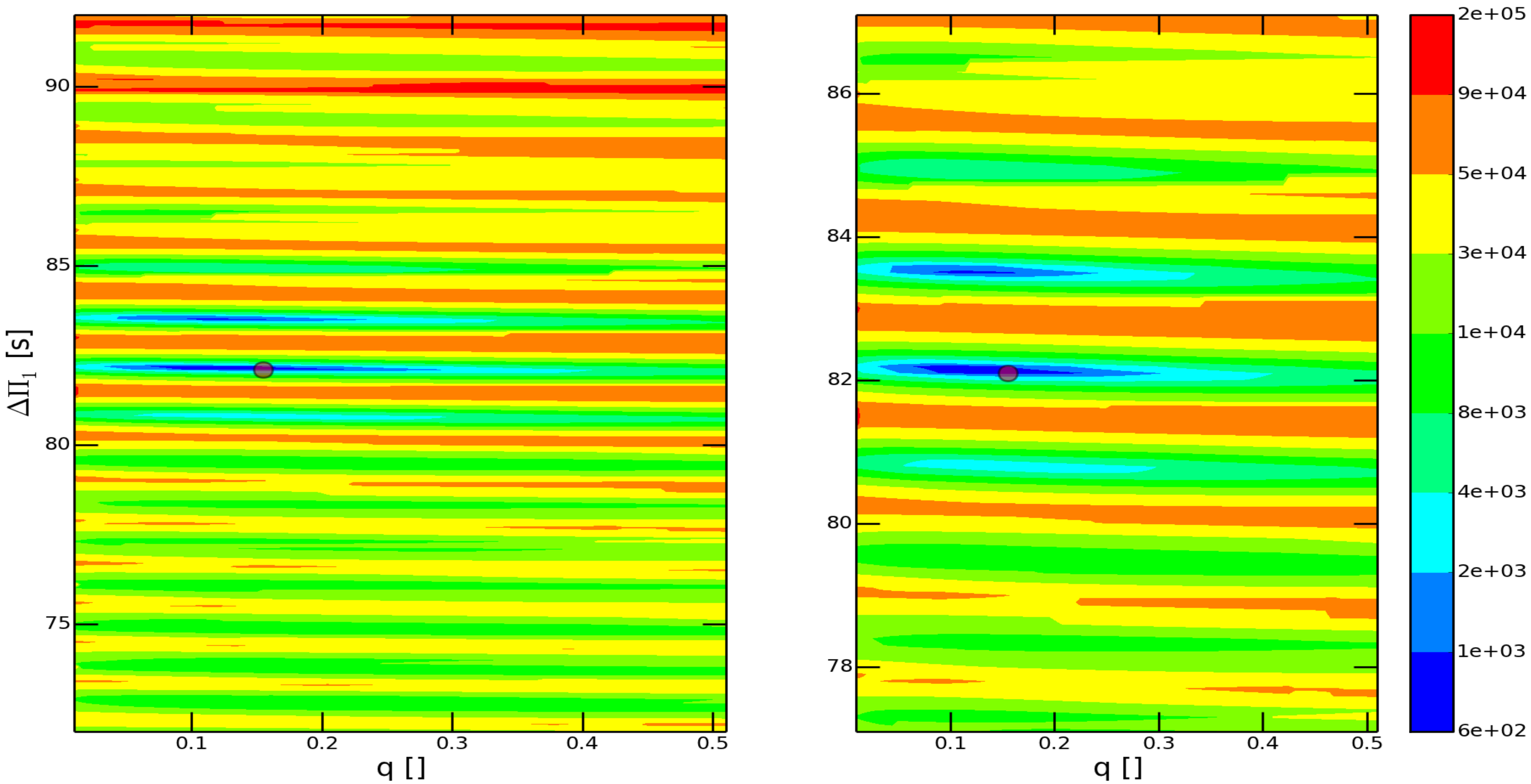

Figure D.2: *Left:* The results from the gridsearch to determine $(\Delta\Pi_1, q)$ using the asymptotic relation for KIC 10593078. The grid is composed of 201 meshpoints along the $\Delta\Pi_1$ axis and 101 along the q axis. The color scale indicates the $\chi^2_{\rm grid}$ derived from the grid search. The best solution for the pair of $(\Delta\Pi_1, q)$ is indicated by a dot. *Right:* A zoom of the region with the optimal solution.

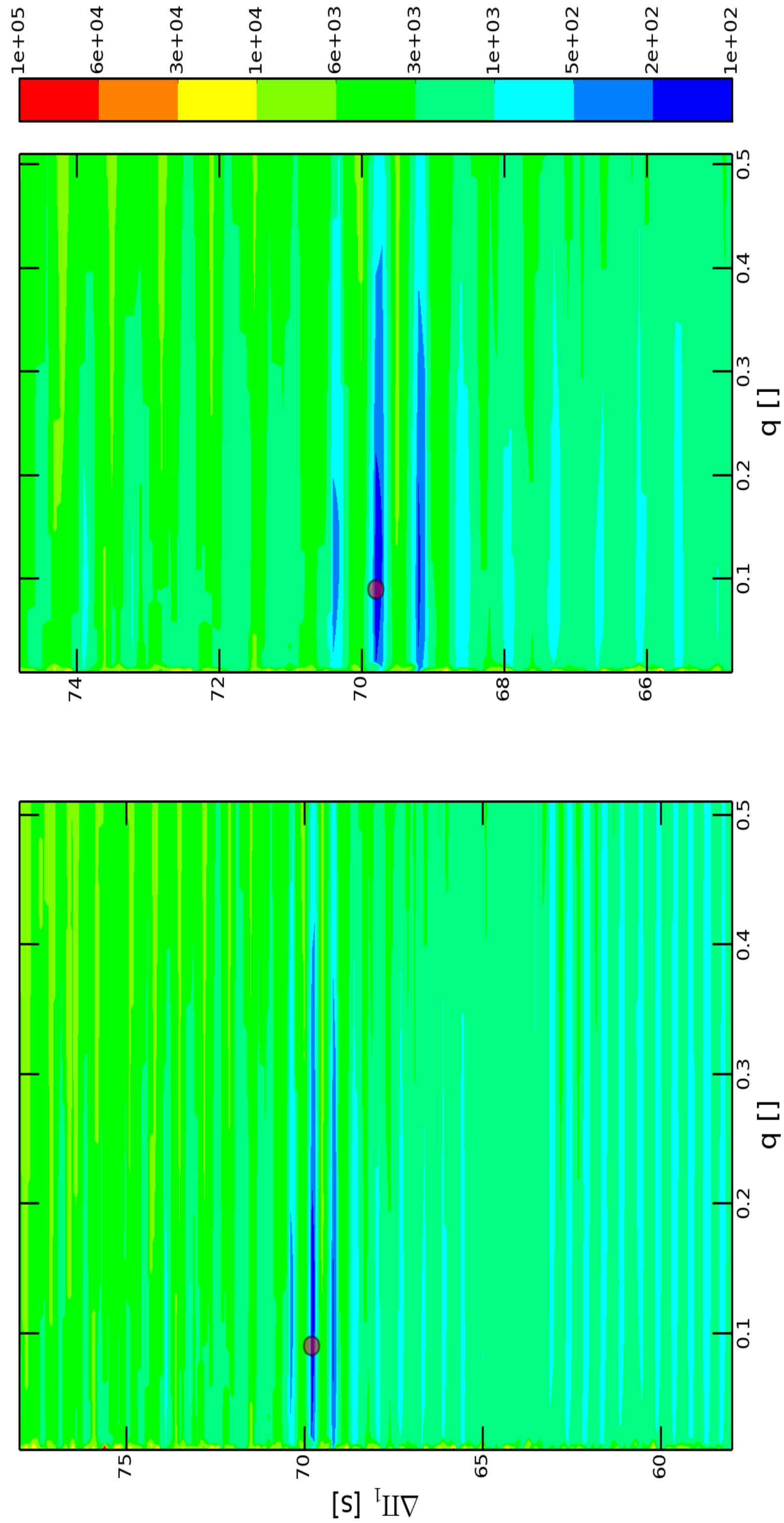

Figure D.3: *Left:* The results from the gridsearch to determine $(\Delta\Pi_1, q)$ using the asymptotic relation for Ziva. The grid is composed of 201 meshpoints along the $\Delta\Pi_1$ axis and 101 along the q axis. The color scale indicates the $\chi^2_{\rm grid}$ derived from the grid search. *Right:* A zoom of the region with the optimal solution. The best solution for the pair of $(\Delta\Pi_1, q)$ is indicated by a dot.

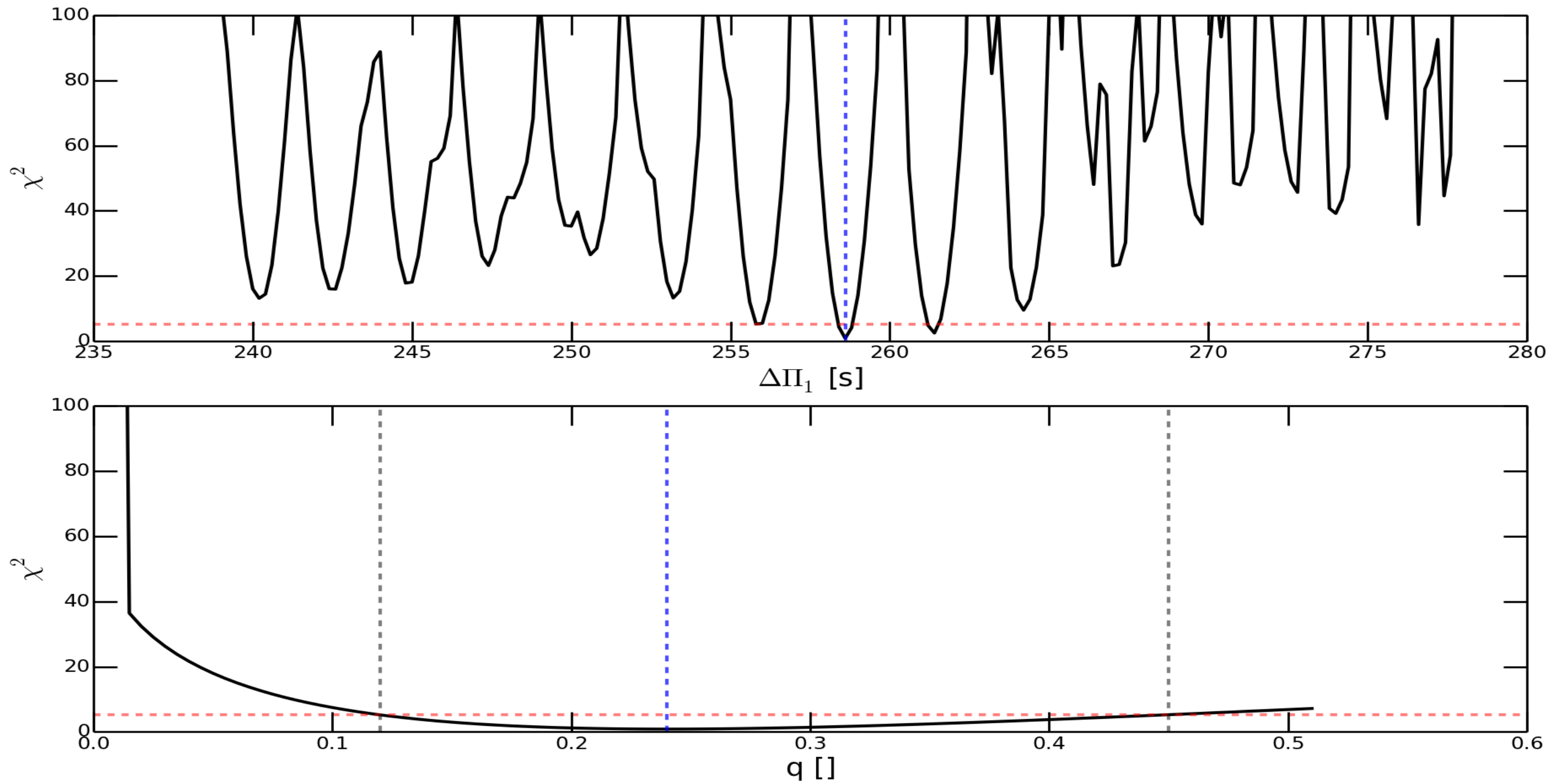

Figure D.4: The cross-cut in the grid along fixed q ($\Delta\Pi_1$) of the optimal solution (blue dashed line) for varying $\Delta\Pi_1$ (q) in the grid is indicated by the black line in the *top* (*bottom*) panel for KIC 6762022. The χ^2 level, corresponding to a 1σ uncertainty is given by the red dashed line. The upper (lower) boundaries for the uncertainty on q are given by the gray dashed lines.

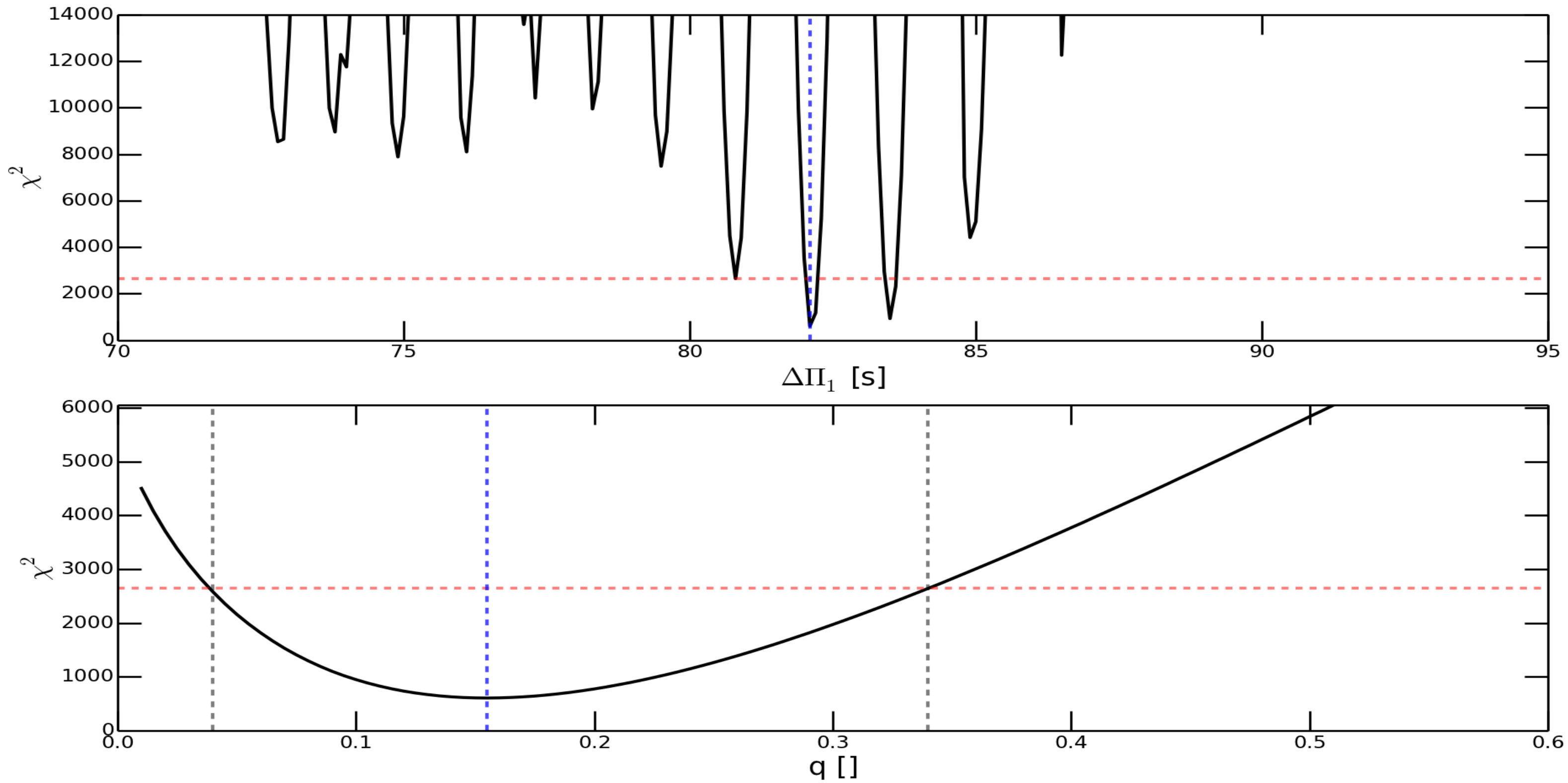

Figure D.5: The cross-cut in the grid along fixed q ($\Delta\Pi_1$) of the optimal solution (blue dashed line) for varying $\Delta\Pi_1$ (q) in the grid is indicated by the black line in the *top* (*bottom*) panel for KIC 10593078. The χ^2 level, corresponding to a 1σ uncertainty is given by the red dashed line. The upper (lower) boundaries for the uncertainty on q are given by the gray dashed lines.

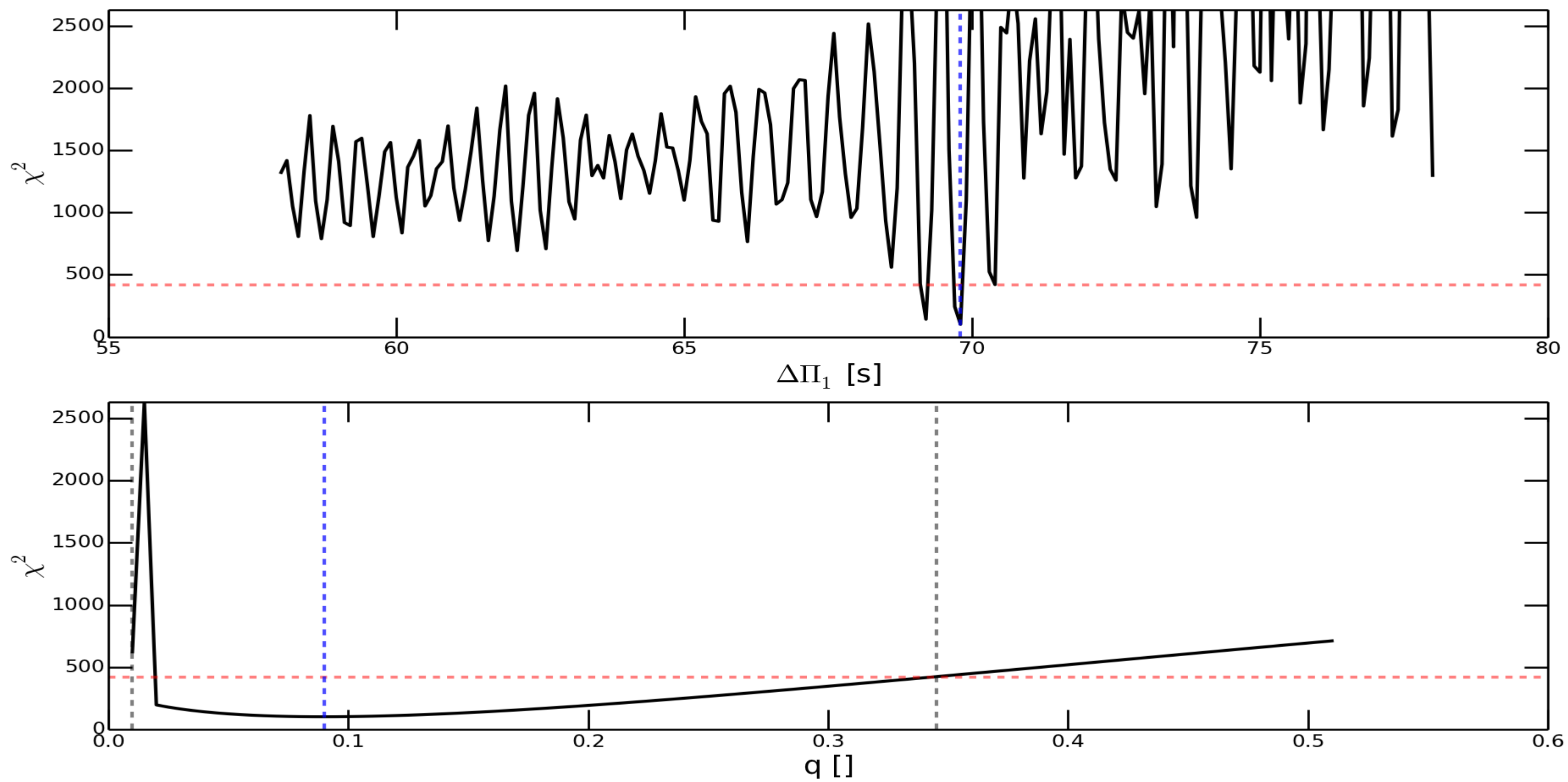

Figure D.6: The cross-cut in the grid along fixed q ($\Delta\Pi_1$) of the optimal solution (blue dashed line) for varying $\Delta\Pi_1$ (q) in the grid is indicated by the black line in the *top* (*bottom*) panel for Ziva. The χ^2 level, corresponding to a 1σ uncertainty is given by the red dashed line. The upper (lower) boundaries for the uncertainty on q are given by the gray dashed lines.

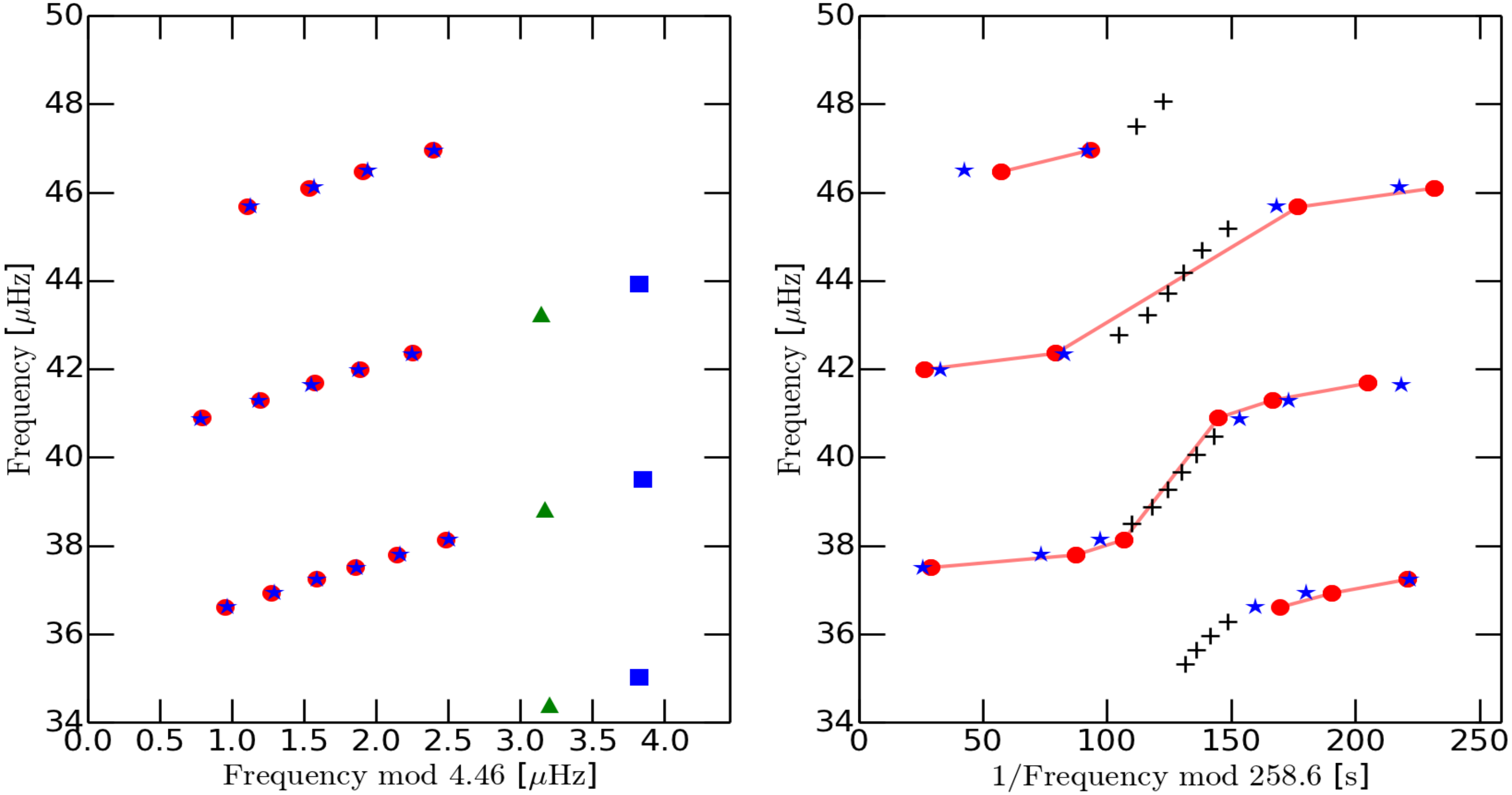

Figure D.7: *Left:* A frequency échelle, comparing the obtained frequencies of the dipole mixed modes for the most likely description using the asymptotic relation with $\Delta\Pi_1 = 258.6$ s and $q = 0.240$ to the extracted modes from the PSD for KIC 6762022. The extracted radial, dipole, quadrupole and octupole modes are indicated by blue squares, red dots, green triangles and yellow diamonds, respectively. The frequencies of the dipole mixed modes, obtained from the asymptotic relation, and which are used in the comparison are indicated by blue stars. *Right:* A period échelle, showing the same comparison as in the left panel with the same colour coding. The black '+' indicate the frequencies for the mixed modes, obtained from the asymptotic relation, which are not used in the comparison.

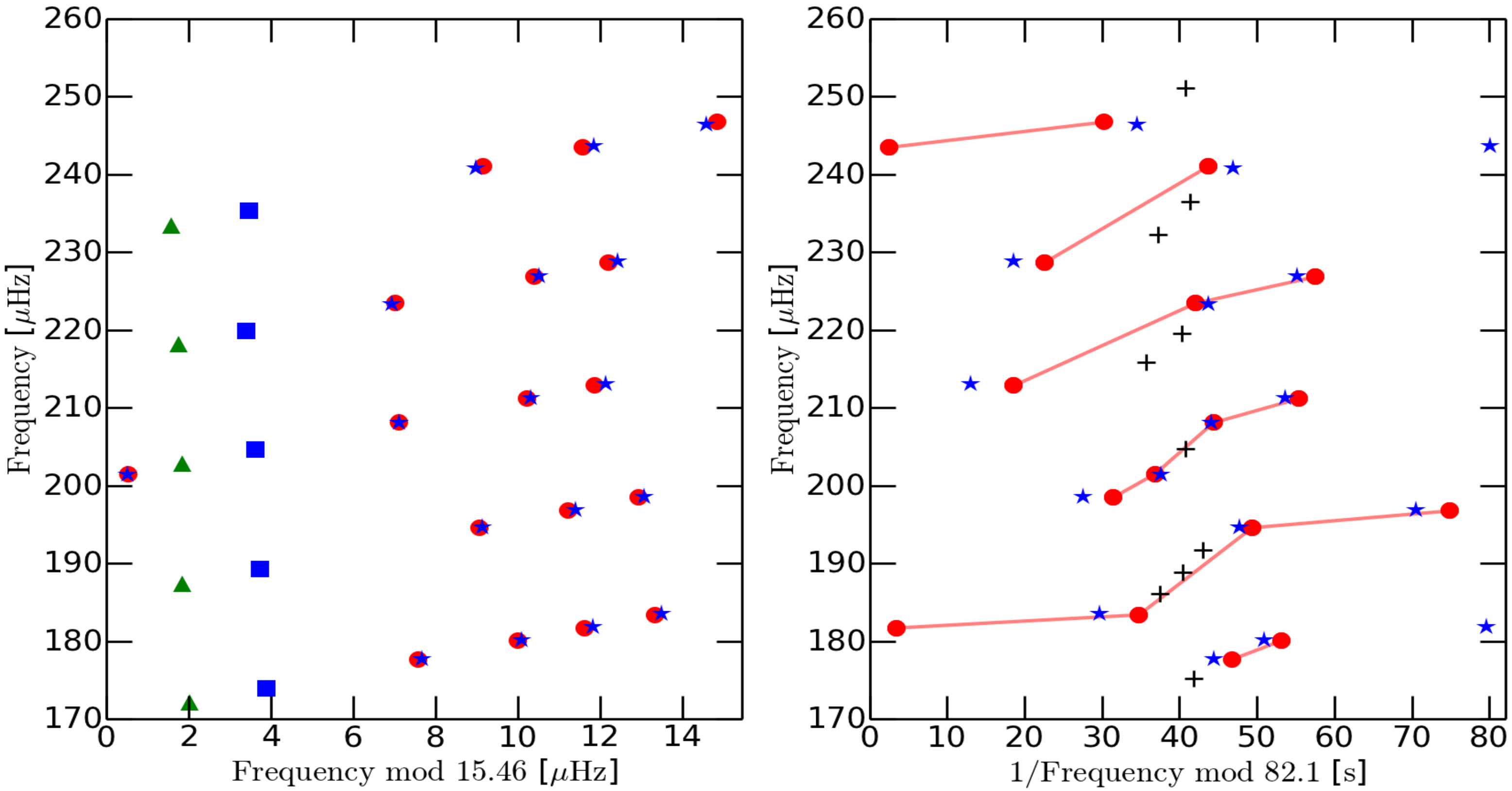

Figure D.8: *Left:* A frequency échelle, comparing the obtained frequencies of the dipole mixed modes for the most likely description using the asymptotic relation with $\Delta\Pi_1 = 82.1$ s and $q = 0.155$ to the extracted modes from the PSD for KIC 10593078. *Right:* A period échelle, showing the same comparison as in the left panel. The same colour coding of Figure D.7 is used.

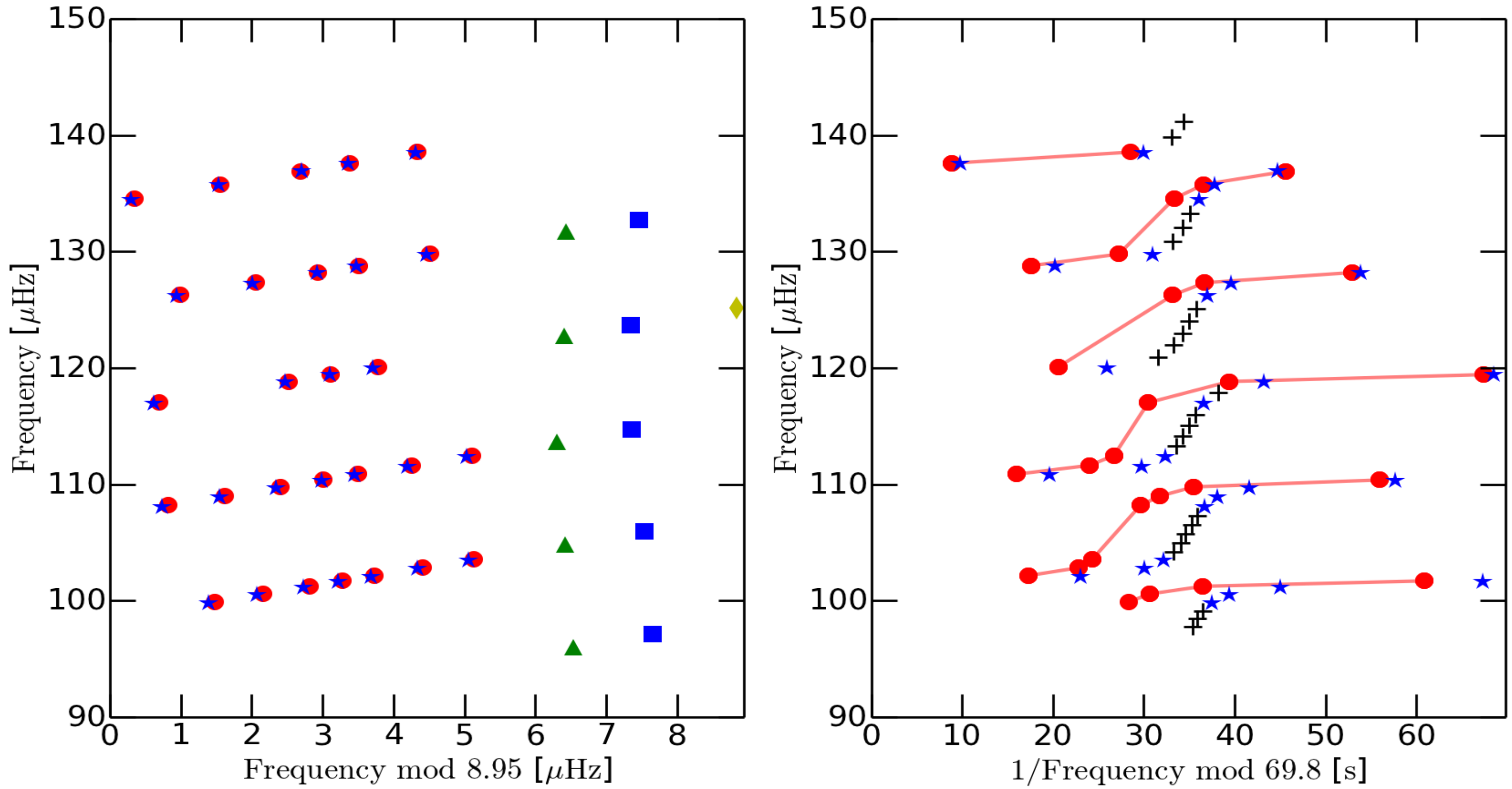

Figure D.9: *Left:* A frequency échelle, comparing the obtained frequencies of the dipole mixed modes for the most likely description using the asymptotic relation with $\Delta\Pi_1 = 69.8$ s and $q = 0.090$ to the extracted modes from the PSD for Ziva. *Right:* A period échelle, showing the same comparison as in the left panel. The same colour coding of Figure D.7 is used.

Appendix E

Comparison between Peak Bagging, Asymptotic Relation and Models

The determined frequencies from the different analyses are presented in a graphical manner in this chapter. The frequencies of the mode extraction, the frequencies of the dipole mixed modes deduced from the asymptotic relation and the frequencies determined from the best stellar model are compared on the same figure for every star in the sample.

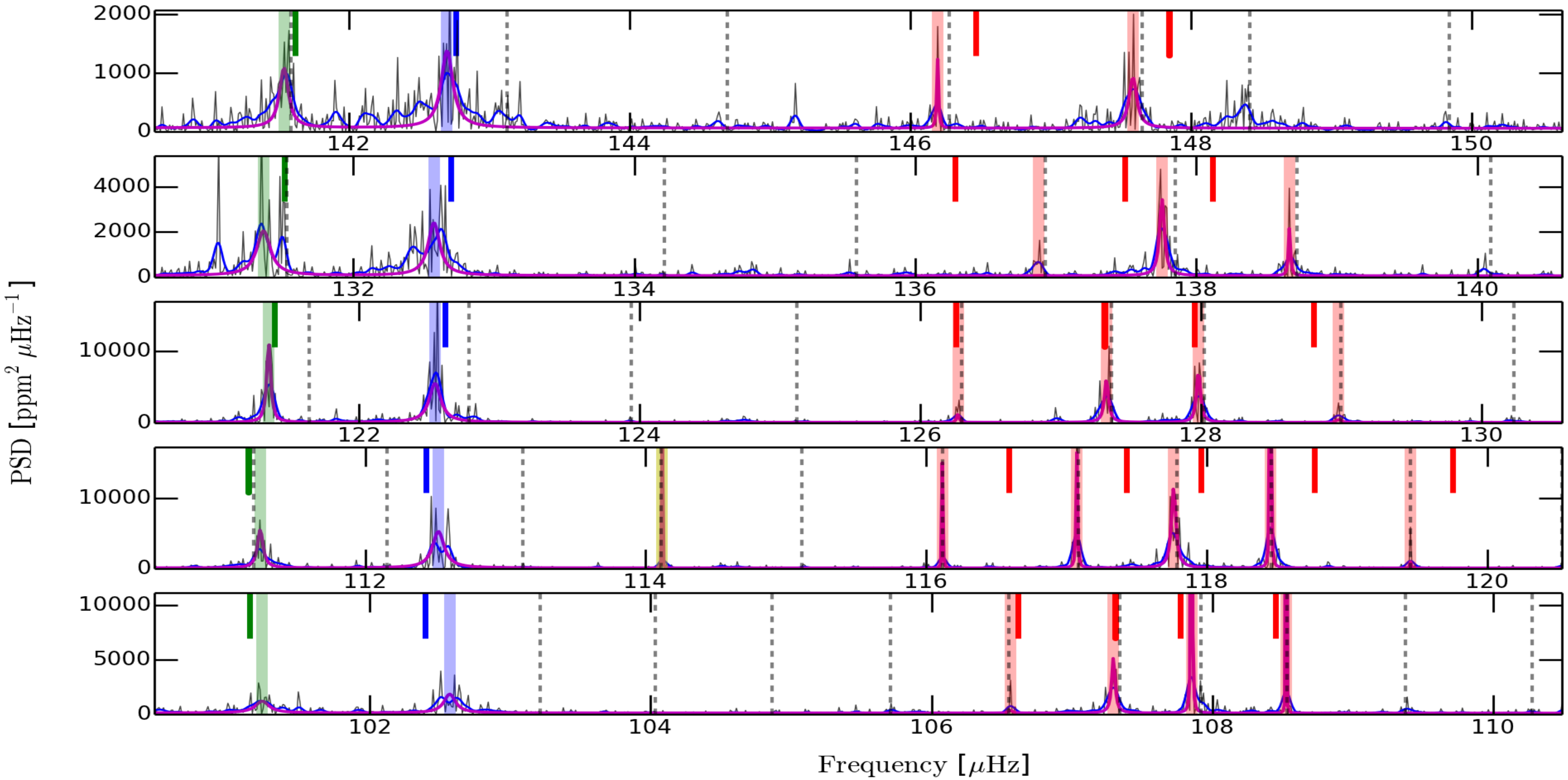

Figure E.1: A comparison between the observed frequencies from the peak bagging, the deduced frequencies for the dipole mixed modes using the asymptotic relation and the frequencies of the best model for KIC 6928997. The radial, dipole, quadrupole and octupole modes retrieved by peak bagging are respectively indicated by the blue, red, green and yellow shaded region in the PSD. The PSD itself is given in black, smoothed with a moving boxcar of 0.1 μHz in blue and the fit in magenta. The best description using the asymptotic relation is found with $\Delta\Pi_1 = 77.2$s and $q = 0.105$ and the deduced frequencies for the dipole mixed modes are given by the black dashed line. The frequencies determined by the best model are given by the arrows, using the same colour coding as the mode extraction. The best model has $M = 1.46\mathrm{M}_\odot$, $R = 6.31\mathrm{R}_\odot$ and $Z = 0.03$.

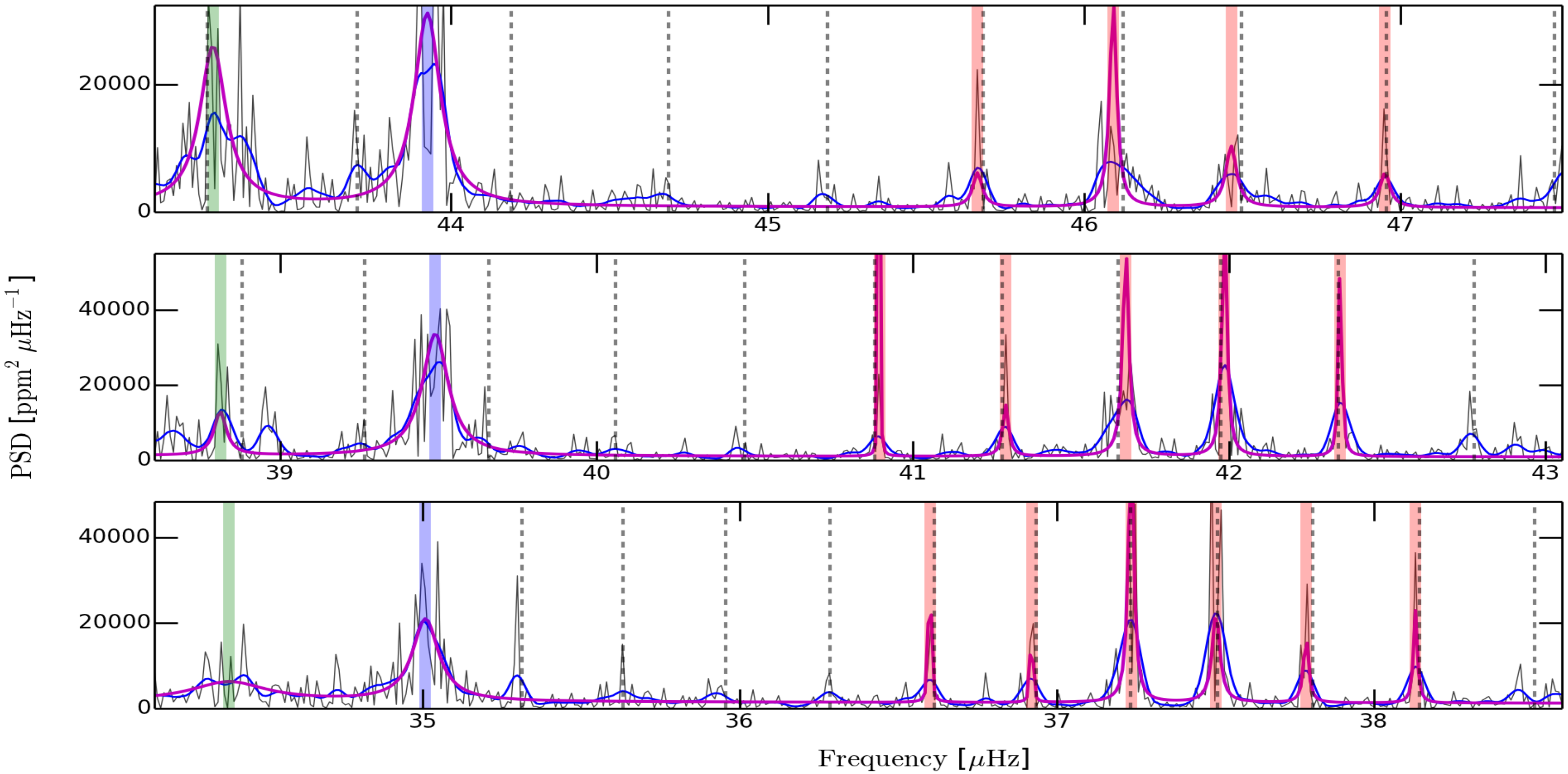

Figure E.2: A comparison between the observed frequencies from the peak bagging, the deduced frequencies for the dipole mixed modes using the asymptotic relation and the frequencies of the best model for KIC 6762022. The same identification and colour coding is uses as Figure E.1. The best description of the asymptotic relation has $\Delta\Pi_1 = 258.6$s and $q = 0.240$ and the best model has $M = 1.47\mathrm{M}_\odot$, $R = 6.90\mathrm{R}_\odot$ and $Z = 0.02$.

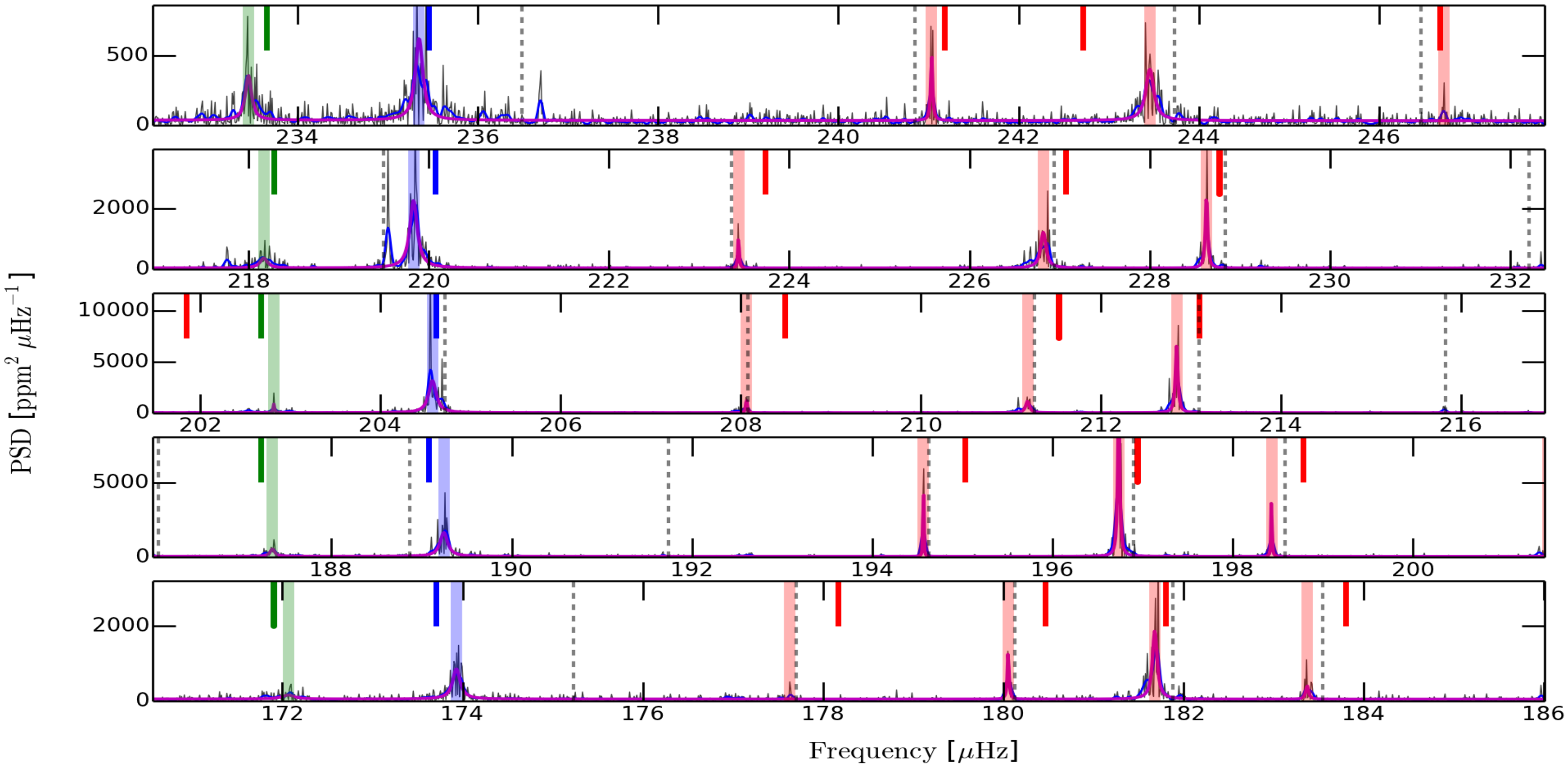

Figure E.3: A comparison between the observed frequencies from the peak bagging, the deduced frequencies for the dipole mixed modes using the asymptotic relation and the frequencies of the best model for KIC 10593078. The same identification and colour coding is uses as Figure E.1. The best description of the asymptotic relation has $\Delta\Pi_1 = 82.1\text{s}$ and $q = 0.155$ and the best model has $M = 1.37\text{M}_\odot$, $R = 4.66\text{R}_\odot$ and $Z = 0.03$.

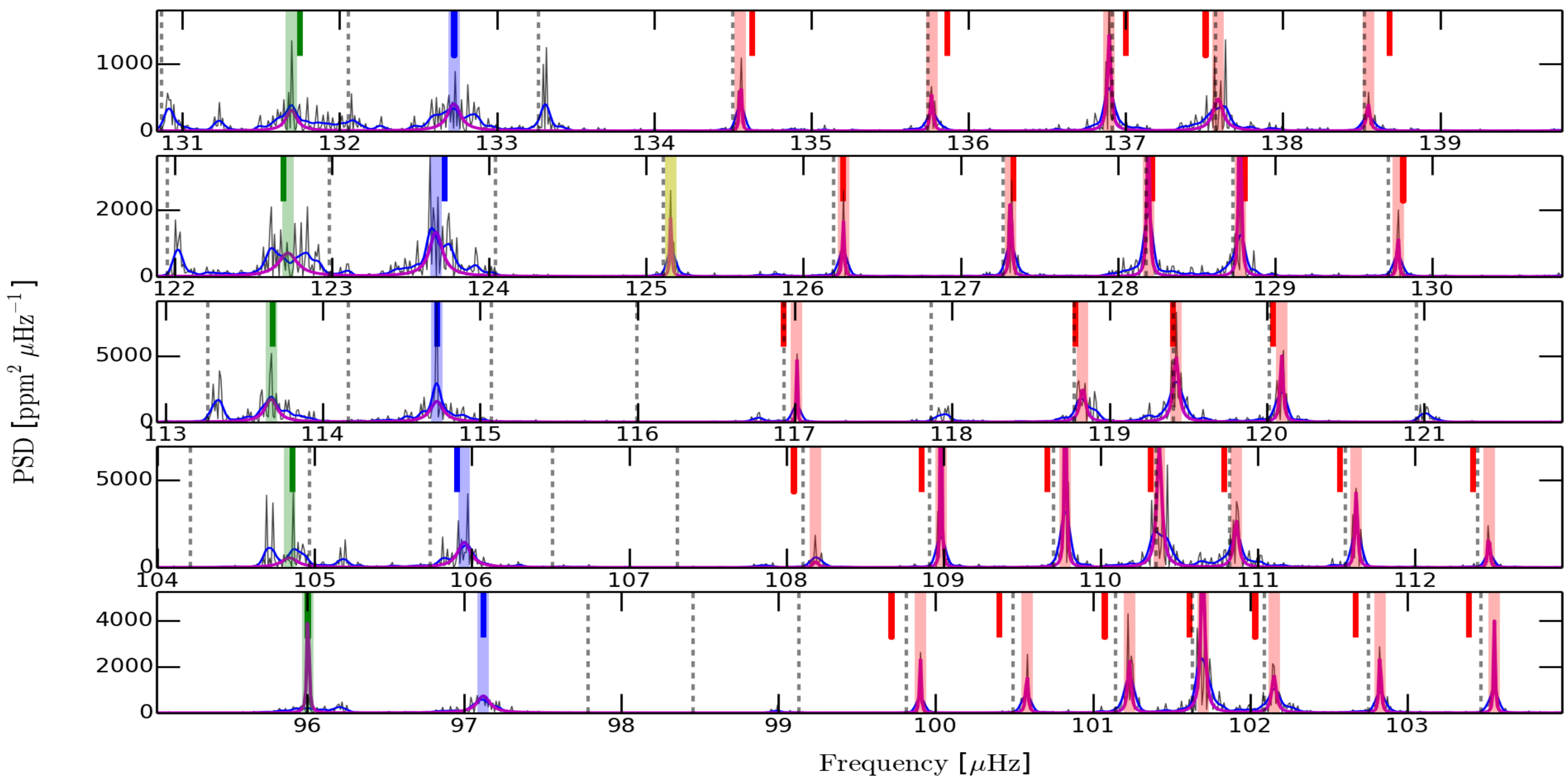

Figure E.4: A comparison between the observed frequencies from the peak bagging, the deduced frequencies for the dipole mixed modes using the asymptotic relation and the frequencies of the best model for Ziva. The same identification and colour coding is uses as Figure E.1. The best description of the asymptotic relation has $\Delta\Pi_1 = 69.2$s and $q = 0.110$ and the best model has $M = 1.44\mathrm{M}_\odot$, $R = 6.90\mathrm{R}_\odot$ and $Z = 0.02$.

Institute of Astronomy
Celestijnenlaan 200D BUS 2401
3001 LEUVEN, BELGIË
tel. + 32 16 32 70 27
fax + 32 16 32 79 99
www.kuleuven.be